University of Strathclyde

Department of Mechanical & Aerospace Engineering

Benchmarking, Development and Applications of an Open Source DSMC Solver

Craig White

A thesis presented in fulfilment of the requirements
for the degree of Doctor of Philosophy

2013

Declaration of author's rights

This thesis is the result of the author's original research. It has been composed by the author and has not been previously submitted for examination which has led to the award of a degree.

Craig White

May 2013

Abstract

Several important engineering gas flow problems fall within the transition Knudsen number regime, e.g. re-entry of spacecraft, or gas flows in micro-scale geometries. The transition regime remains the most difficult to obtain reliable analytical or numerical results for, but the most successful method has been the direct simulation Monte Carlo (DSMC) numerical technique.

Due to the nature of high temperature, hypersonic flows, and equipment limitations at the micro-scale, there is a scarcity of reliable experimental data for transition regime flows; numerical experiments using DSMC are an essential tool for the design of engineering systems that encounter these kinds of flows.

We benchmark a recently developed open-source DSMC solver against existing DSMC solvers, analytical solutions, and experimental data. The solver is then extended to include some important features that enable it to be applied to a larger range of engineering problems. Vibrational energy and the quantum-kinetic chemical reaction model are implemented in our DSMC solver, preparing it for use with hypersonic flow problems with shockwaves and local regions of very high temperature. Low speed fixed pressure boundary conditions are also implemented, for use with simulations of gas flows in micro-channels.

The extended solver is then used to investigate two different engineering problems. Firstly, simulations of gas flows in micro-channels with bends are performed. We find that the inclusion of a sharp ninety degree bend does not lead to significant losses, and can even lead to a small increase in mass flow rate within a limited range of Knudsen number. Adding a second bend is found to increase this mass flow rate enhancement.

Finally, we investigate rarefied gas effects on high area-to-mass ratio spacecraft in low Earth orbit, taking inspiration from the Crookes radiometer. We find that the

non-equilibrium gas effects can be exploited for use as propellant-free inter-spacecraft position control within a swarm, by altering the temperature of one spacecraft relative to another. A small degree of attitude control can be exercised in a similar manner, through non-uniform heating of an individual spacecraft.

Acknowledgements

Firstly I thank my supervisors Dr Tom Scanlon and Prof. Jason Reese for their constant guidance, knowledge, advice, expertise and support that they have provided throughout the past 3 and a half years.

Thank you to the rest of the researchers in the James Weir Fluids Laboratory for many useful and enlightening discussions throughout this process. In particular; Dr Matthew Borg for selflessly providing a lot of his time and expertise in OpenFOAM programming, Dr William Nicholls for putting up with my many queries while I learned OpenFOAM and Linux, and Dr Nishanth Dongari for many hours of discussions on all things rarefied gas.

Thank you also to Dr Camilla Colombo, formerly of the Advanced Space Concepts Laboratory at Strathclyde (now at the University of Southampton), who has been like a third supervisor to me; firstly for bringing me a problem that led to an interesting chapter of this thesis, and for her support in the unfamiliar area of spacecraft and orbital dynamics.

I recognise, and am thankful for, the financial support of the James Weir Foundation in the form of the scholarship that they have provided me with.

Finally, I would like to thank my family, who have supported me unconditionally throughout my whole life and education – none of this would not have been possible without them.

Contents

List of Figures

List of Tables

Nomenclature

A	cross-sectional area
a	speed of sound
B	Earth's local magnetic field
c	molecular speed
$\mathbf{c}$	molecular velocity vector
c_f	skin friction coefficient
c_g	centre of gravity
c_h	heat transfer coefficient
c_p	centre of pressure
c_{pa}	centre of aerodynamic pressure
c_r	relative speed
D	residual magnetic dipole
d	molecular diameter
E_a	activation energy
E_c	collision energy
e	specific energy
$\mathbf{F}$	force vector
F_N	number of real atoms/molecules each DSMC particle represents
f	normalised velocity distribution function
G_{Earth}	gravitational parameter of the Earth
g	applied acceleration
H	altitude

h	height
I	mass moment of inertia
i	vibrational quantum level
J	collision integral
k_B	Boltzmann constant
k_f	forward reaction rate coefficient
k_r	reverse reaction rate coefficient
Kn	Knudsen number
L	length
Ma	Mach number
m	molecular mass
$\dot{m}$	mass flow rate
m_r	reduced mass
N	number of molecules/DSMC particles
$\dot{N}$	number flux
n	number density
P	scalar pressure
Pr	Prandtl number
$\mathbf{p}$	pressure tensor
Q	normalised mass flow rate
$\mathbf{q}$	heat flux vector
R	specific gas constant
$R13$	regularised 13 moment equations
$R26$	regularised 26 moment equations
R_1, R_2	cylinder radii
R_{coll}	collision rate in equilibrium VHS gas
Re	Reynolds number
R_{Earth}	equatorial radius of the Earth
R_f	random fraction
$\mathbf{r}$	molecule position vector
r	molecular radius

r_{orbit}	orbital radius
s	speed ratio
T	temperature
T_a	aerodynamic disturbance torque
T_g	gravity gradient torque
T_m	magnetic disturbance torque
t	time
U	velocity
V	volume
w	width
Z	relaxation number
u, v, w	velocity vector components
x, y, z	spatial Cartesian co-ordinates

Greek

α	angle of attack
γ	ratio of specific heats
δ	mean molecular separation
δ_m	rarefaction parameter
ϵ	mass flow rate enhancement factor
ε	energy
ζ	degrees of freedom
Θ_r	post-surface interaction scattering angle
θ_d	dissociation temperature
θ_v	characteristic vibrational temperature
ϑ, ϕ	post-collision scattering angles
λ	mean free path
μ	viscosity
ξ	collision cross-section
ρ	mass density
ϱ	energy accommodation coefficient

σ	momentum accommodation coefficient
$\boldsymbol{\tau}$	viscous shear stress tensor
τ	wall tangential shear stress
Ω	solid angle
ω	viscosity exponent
ω_1, ω_2	angular velocities

Superscripts

$*$	post-collision/surface interaction properties
$\prime$	thermal velocity

Subscripts

0	stream properties
bend	properties in bent micro-channel
c	cold
cm	centre of mass
coll	collision properties
g	gas properties
h	hot
in	properties at inlet face
inc	incident
j	properties in boundary cell
lin	linear
M	Maxwell's fraction
max	maximum
mc	mean collision
mp	most probable
N-S	Navier-Stokes
n	normal direction
out	properties at outlet an face

proc	processor
ref	reference properties
refl	reflected
rot	rotational
s	surface properties
straight	properties in straight micro-channel
tr	translational
v	vibrational
w	wall properties

Acronyms

CFD	computational fluid dynamics
CLL	Cercignani-Lampis-Lord
DSMC	direct simulation Monte Carlo
GUI	graphical user interface
HMM	Heterogeneous Multiscale Method
HPC	high performance computer
LB	Larsen-Borgnakke
LEO	low Earth orbit
MD	molecular yynamics
MEMS	microelectromechanical systems
NIST	National Institute of Standards and Technology
NSF	Navier-Stokes-Fourier
NTC	no time counter
ODE	ordinary differential equation
OpenFOAM	Open Field Operation And Manipulation
QK	quantum kinetic
SMILE	Statistical Modeling In Low Density Environment
TCE	total collision energy
VHS	variable hard sphere

Chapter 1

Introduction

Somewhere, something incredible is waiting to be known.

- Carl Sagan

1.1 Motivation

In this thesis we investigate computationally the interesting and non-intuitive behaviour of rarefied gas flows. Rarefied gas dynamics is the study of fluid flows at a length scale L comparable to the mean free path λ of the gas molecules (the average distance a gas molecule travels before encountering another gas molecule), and where the gas behaviour cannot be accurately predicted by traditional engineering methods, such as the Navier-Stokes-Fourier (NSF) equations. These rarefied flows can typically be found in low density hypersonic applications, such as re-entry of spacecraft [1]. However, more recently the development of advanced fabrication techniques, which enable the manufacturing of micro- and nano-scale devices, has resulted in rarefied gas flows being found at standard atmospheric pressure and very low Mach number in these devices [2].

Numerical experiments are an essential tool in the study of rarefied gas dynamics because physical experiments are often difficult to perform accurately, and the data that can be obtained is limited. For high temperature hypersonic applications, modern experimental data is scarce due to the high financial costs involved in performing the experiments. For example, much of the experimental data available for dissociation reactions at high temperature are from the 1960s and 1970s, and are subject to signifi-

cant uncertainties [3]. It is important to accurately predict the aero-thermo-mechanical loads on a spacecraft during the re-entry portion of the mission so that the thermal protection systems are designed both safely and efficiently. Since the gas surrounding the spacecraft can be rarefied, we must take care to use numerical methods that can account for rarefaction. Examples of computational rarefied gas dynamics techniques being applied to hypersonic engineering problems include re-entry of the Apollo capsule [4], de-orbiting of the Mir space station [5], and to provide supporting evidence for the failure scenario that resulted in the loss of Space Shuttle *Columbia* in 2003 [6].

At the micro-scale, detailed experimental results are often unavailable due to current technological limitations of measurement equipment. As such, experimental results are often limited to measurements of integral flow parameters such as mass flow rates [7]. In this situation, computer simulation provides an opportunity to supplement any available experimental data in a cost effective manner, and any available experimental data is vital in order to validate and benchmark numerical methods. It is important to accurately predict flow parameters to maximise the performance of these devices; this can most efficiently be done by gaining an understanding of the fundamental behaviour of low speed rarefied gases, which can differ greatly from that of its macro-scale companion. At the micro-scale, rarefied gas dynamics is still used primarily to gain more of a fundamental understanding of the unconventional physics involved in the operation of microelectromechanical systems (MEMS), rather than to engineer systems. However, rarefied gas dynamics has contributed towards the development of many technologies, including micro-fuel cells, micro-pumps, and micro-turbines.

In this thesis, we will only consider dilute gases. So long as the gas molecular diameter d is small compared to the mean molecular separation δ, i.e. $d \ll \delta$, the gas can be considered dilute and the kinetic theory of dilute gases can be applied to describe the state of the gas at any given point. The large molecular separation allows the assumption that inter-molecular potentials can be neglected (and hence Boltzmann's molecular chaos assumption can be applied) and that only binary collisions will occur. It is therefore considered that molecules move in free paths until they encounter another molecule, and then they undergo an elastic collision.

The rest of this chapter provides an outline of this thesis and an introduction to

rarefied gas dynamics.

1.2 Thesis Outline

In Chapter 2 we describe direct simulation Monte Carlo (DSMC), the numerical technique used to perform all of the simulations in this thesis. A history of the method from the first publication in 1963 to modern state-of-the-art is discussed.

In Chapter 3 we perform some benchmark cases with *dsmcFoam*, a new open-source DSMC solver. Our results are compared to analytical solutions, established DSMC codes, and experimental measurements.

The expansion of *dsmcFoam* to include vibrational energy, a state-of-the-art chemical reaction model, a robust macroscopic properties measurement framework, and the Cercignani-Lampis-Lord gas-surface interaction model is described in Chapter 4.

Chapter 5 deals with the implementation of subsonic pressure boundary conditions in *dsmcFoam*, and we then propose an extension to these that accounts for rotational non-equilibrium at the exit of a micro-channel. Micro-channels with sharp ninety-degree bends are studied using DSMC, and, in agreement with previous lattice Boltzmann results, we find that a small mass flow rate enhancement can be achieved by including bends in a micro-channel geometry. Cylindrical Couette flows are also investigated over a wide range of different geometric configurations, rarefaction and surface accommodation.

Taking inspiration from the classical Crookes radiometer, rarefied gas effects on high area-to-mass ratio spacecraft in low Earth orbit are studied in Chapter 6. True radiometric forces are not found to exist due to the near vacuum wake created behind the spacecraft, but it is still possible to take advantage of rarefied gas effects as control techniques without the need for any propellent.

The key findings of this research presented in this thesis and discussion of future work based on it, is covered in Chapter 7.

1.3 Rarefied Gas Dynamics

1.3.1 The Knudsen number

Rarefied gas dynamics is the study of gases in which the molecular mean free path λ is not negligible with respect to the characteristic length scale L of the system under consideration. The degree of rarefaction is defined by the Knudsen number

$$Kn = \frac{\lambda}{L}. \tag{1.1}$$

In the limit of zero Knudsen number, inter-molecular collisions dominate and the gas is in perfect thermodynamic equilibrium. As the Knudsen number increases, molecular collisions become less likely to occur until the free-molecular limit is reached, when inter-molecular collisions are very unlikely. Since it is inter-molecular collisions and gas-surface interactions that drive a system towards thermodynamic equilibrium, it is clear that non-equilibrium effects become dominant with increasing Knudsen number. The different Knudsen number regimes are illustrated in Figure 1.1.

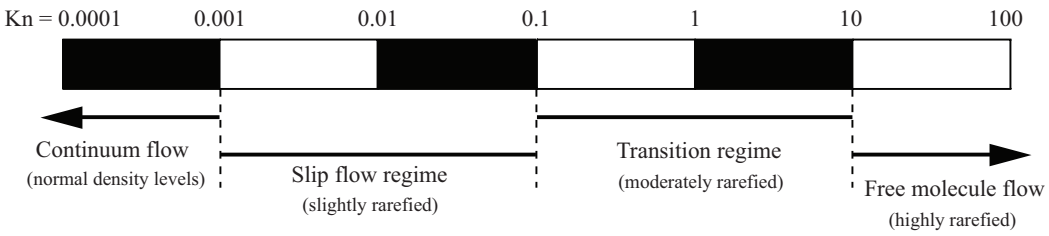

Figure 1.1: Knudsen number regimes, adapted from Reference [2].

A description of each regime and the appropriate numerical approach for each one can be summarised as [2]:

- $Kn \to 0$: inviscid flow (Euler equations);
- $Kn \leq 0.001$: continuum regime (Navier-Stokes-Fourier equations);
- $0.001 \leq Kn \leq 0.1$: slip regime (Navier-Stokes-Fourier equations with velocity slip and temperature jump boundary conditions);
- $0.1 \leq Kn \leq 10$: transition regime (Boltzmann equation or particle methods);

- $Kn \geq 10$: free-molecular regime (collisionless Boltzmann equation or particle methods).

Continuum Regime

In continuum flow regime, the familiar Navier-Stokes-Fourier (NSF) equations provide an excellent approximation for gas flows that are very close to equilibrium. At this low Knudsen number it is assumed that local macro-properties can be described as averages over elements large compared to the microscopic structure of the fluid, but small enough with respect to the macroscopic phenomena to permit the use of differential calculus to describe them. Inter-molecular collisions are dominant at low Knudsen number, i.e. there are enough molecular collisions occurring for thermodynamic equilibrium to be reached in a very short time compared to the macroscopic time scale. In the limit of zero Knudsen number, the NSF equations can be reduced to the inviscid Euler equations because molecular diffusion can be ignored, and so the transport terms in the continuum momentum and energy equations are negligible [2].

Slip Regime

As the Knudsen number becomes significant, molecule-surface interactions become less frequent and regions of non-equilibrium start to appear near surfaces. This non-equilibrium can be observed from a macroscopic point of view as the gas velocity and temperature (U_g and T_g) at a surface not obtaining the same values as the surface (U_s and T_s). These phenomena are known as velocity slip and temperature jump. Despite this form of non-equilibrium becoming important, the range of validity of the NSF equations can be extended to the slip regime by applying Maxwell's velocity slip [8] and Von Smoluchowski's temperature jump [9] boundary conditions, which for planar surfaces have the form

$$U_g - U_s = \frac{2-\sigma}{\sigma}\lambda\left(\frac{\partial u}{\partial y}\right)_s + \frac{3}{4}\frac{\mu}{\rho T_g}\left(\frac{\partial T}{\partial x}\right)_s, \tag{1.2}$$

and

$$T_g - T_s = \frac{2-\varrho_T}{\varrho_T}\left[\frac{2\gamma}{(\gamma+1)}\right]\frac{\lambda}{Pr}\left(\frac{\partial T}{\partial y}\right)_s, \tag{1.3}$$

respectively, where σ and ϱ_T are the tangential momentum accommodation coefficient (TMAC) and the thermal-accommodation coefficient respectively, ρ, μ, Pr and λ are the fluid density, viscosity, Prandtl number, and mean free path at the surface, respectively, and γ is the specific heat ratio.

Transition and Free-Molecular Regimes

In the transition and free-molecular regimes non-equilibrium effects dominate and a solution to the Boltzmann equation must be sought, as the assumption of linear constitutive relations in the NSF equations is no longer valid. For a single species, monatomic gas, the Boltzmann equation has the form

$$\frac{\partial (nf)}{\partial t} + \mathbf{c}\frac{\partial (nf)}{\partial \mathbf{r}} + \mathbf{F}\frac{\partial (nf)}{\partial \mathbf{c}} = J(f, f^*), \tag{1.4}$$

where nf is the product of the number density and the normalised velocity distribution function, $\mathbf{r}$ and $\mathbf{c}$ are the position and velocity vectors of a molecule, respectively, $\mathbf{F}$ is an external force, $J(f, f^*)$ is a non-linear integral that describes the binary collisions, and the superscript $*$ represent post-collision properties. The collision integral takes the form:

$$J(f, f^*) = \int_{-\infty}^{\infty}\int_{0}^{4\pi} n^2 \left(f^* f_1^* - f f_1\right) c_r \xi d\Omega d\mathbf{c}_1, \tag{1.5}$$

where f and f_1 are the velocity distribution function at $\mathbf{c}$ and $\mathbf{c}_1$ respectively, c_r is the relative speed of two colliding molecules, ξ is the molecular cross-section, and Ω is the solid angle.

So long as the assumptions of molecular chaos and binary collisions are met, the Boltzmann equation is valid for all ranges of Knudsen number. It is, however, difficult to obtain exact analytical solutions to the Boltzmann equation due to the non-linear nature of the collision integral. In the free-molecular regime, the collision integral can be ignored and the Boltzmann equation can then be solved with relative ease. It is the transition regime that presents most difficulty in finding a solution; the Knudsen number is significant, but inter-molecular collisions are still important. Several analytical methods for solving the Boltzmann equation in the transition regime have been proposed; however, these solutions depend either on arbitrary assumptions being made

about the form of the velocity distribution function (Moment methods) [10–12], or on a simplification of the collision term on the right hand side of the Boltzmann equation (model equations), e.g. the Bhatnagar-Gross-Krook (BGK) method [13].

The Moment methods have seen significant progress in recent years, with the introduction of the regularised 13 moment (R13) [14] and regularised 26 moment (R26) [15] equations, along with wall boundary conditions [16] making it possible to solve 2D Couette and Poiseuille flow problems [17–19]. The R13 equations are valid until around Knudsen number 0.5 [20], and the R26 equations extend the Moment methods further [19]. The moment methods are not yet suitable for 3D problems and are not currently capable of solving problems with complex arbitrary geometries. The BGK method is only valid for small departures from equilibrium, but this does allow the BGK equation to be linearised and solved relatively easily [21] and it is useful for solving problems involving small perturbations, e.g. gas flows in MEMS [22].

Attention has therefore turned to numerical methods to find solutions to the Boltzmann equation. Direct simulation methods enable the difficulties associated with the particulate nature of the gas (the collision integral of the Boltzmann equation) in analytical solutions to be used as an advantage. Simulation particles represent real molecules, and their positions, velocities and energies are stored and updated with time as the simulation proceeds. By far, the most successful numerical method for solving rarefied gas flows in the transition regime has been the direct simulation Monte Carlo method (DSMC) [21]. DSMC is a stochastic particle-based method based on the kinetic theory of dilute gases. It is the technique that we apply throughout this thesis to perform numerical experiments in a wide variety of different situations, showing the strength of this numerical method. We give a comprehensive history of the method in the following chapter, along with a detailed description of the DSMC algorithm and sub-routines, before describing the state-of-the-art in DSMC and the different DSMC codes available.

1.3.2 Kinetic Theory

Kinetic theory is a statistical theory of the dynamics of systems formed from a great number of individual molecules. It describes the macroscopic behaviour of a system in terms of the microscopic molecule movements and interactions, utilising probability

theory. These molecule interactions are always considered as binary collisions in kinetic theory; since the gas is dilute it is very unlikely that three or more molecules will be involved in a single collision event [23].

Molecular interactions can be described using classical Newtonian mechanics and assuming the molecules interact with a force relative to their separation distance, $\mathbf{F}_{ij}$ — the force imparted on molecule i by molecule j — the equations of motion for all molecules in the system can be written as a set of coupled ordinary differential equations (ODEs) of the form

$$\frac{d^2}{dt^2}\mathbf{r}_i = \frac{1}{m}\sum_{\substack{j=1 \\ j\neq i}}^{N} \mathbf{F}_{ij}, \tag{1.6}$$

where m is the mass of one molecule and $\mathbf{r}_i$ is its position. Molecular dynamics [24] (MD) is a numerical technique that solves these coupled ODEs deterministically. It is a very computationally demanding technique; a cubic centimetre of dilute gas at standard temperature and pressure contains 2.687×10^{19} molecules. Even on modern high performance computers using parallel processing techniques, MD is restricted to very small volumes and timescales [25].

Statistical mechanics is used in order to treat these large numbers as an advantage, rather than a hindrance. No attempt is made to calculate the exact state of each individual molecule; probability theory is employed along with averaging techniques, making the large numbers an advantage as even in a small system there will be a large statistical sample. In a dilute gas, it is assumed that all of a molecule's energy is kinetic energy. This is a fair assumption because of the relatively large distances between molecules for the most part, so short-range inter-molecular forces can be ignored.

The Maxwell-Boltzmann distribution

The probability P that a molecule's thermal speed is between c' and $c' + dc'$ is given by the probability distribution;

$$P_{c'}\left(c'\right)dc' = 4\pi\left(\frac{m}{2\pi k_B T}\right)^{3/2}\left(c'\right)^2 e^{-\frac{1}{2}mc'^2/k_B T}dc'. \tag{1.7}$$

This is the well known equilibrium Maxwell-Boltzmann molecular speed distribution function, where k_B is Boltzmann's constant, T is the local macroscopic translational temperature of the gas and m is the molecular mass. Various average properties of an equilibrium gas be calculated easily from this distribution function. For example, the average molecular speed is

$$\overline{c'} = \int_0^\infty c' P_{c'} dc' = \sqrt{\frac{8k_B T}{\pi m}}. \tag{1.8}$$

The most probable thermal velocity c'_{mp} is the point where the Maxwell-Boltzmann distribution has a maximum; i.e.

$$\frac{d}{dc'} P_{c'} \left(c'\right) \Big|_{c'=c'_{mp}} = 0, \tag{1.9}$$

which gives

$$c'_{mp} = \sqrt{\frac{2k_B T}{m}}. \tag{1.10}$$

Figure 1.2 shows equilibrium Maxwell-Boltzmann speed distributions at temperatures of 173 K and 293 K. The most probable thermal speed at 293 K is also plotted.

Macroscopic Properties

In engineering applications, it is important to be able to define macroscopic properties such as temperature and density, rather than consider only molecular properties. Here we describe how to recover a variety of macroscopic flow properties from the individual molecular properties. For the sake of succinctness, we restrict our analysis here to a single species gas with rotational energy, but no vibrational energy. All definitions are valid for equilibrium and non-equilibrium gases. The simplest property is the number density n, which is defined as the number of molecules N in the volume of interest V;

$$n = \frac{N}{V}, \tag{1.11}$$

and the mass density ρ is simply the product of the molecular mass m and the number density;

$$\rho = nm. \tag{1.12}$$

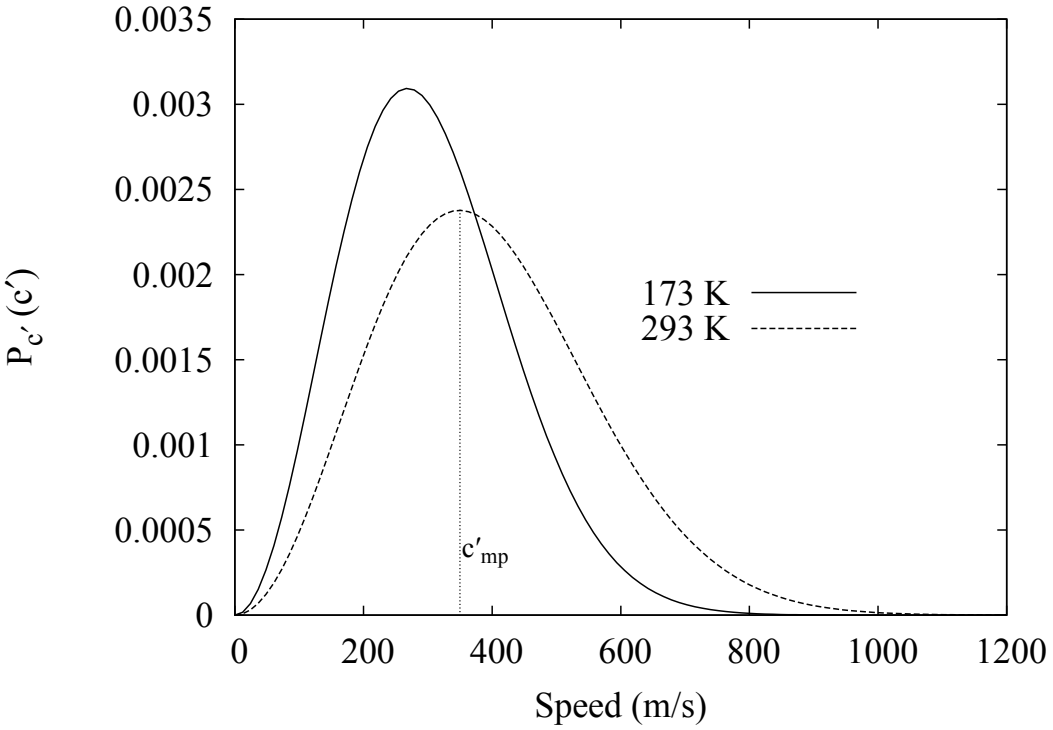

Figure 1.2: Maxwell-Boltzmann molecular speed distribution for argon gas at two different temperatures.

Other macroscopic properties are related to the transport of mass, momentum, and energy via molecular motion in a system. The macroscopic, or stream, velocity $\mathbf{c}_0$ is the mean of the instantaneous molecular velocities $\mathbf{c}$

$$\mathbf{c}_0 = \frac{\sum_{i=1}^{N} \mathbf{c}}{N}. \tag{1.13}$$

The instantaneous velocity of a molecule relative to the stream velocity is called the peculiar, or thermal, velocity $\mathbf{c}'$;

$$\mathbf{c}' = \mathbf{c} - \mathbf{c}_0. \tag{1.14}$$

We now consider the gas from a reference frame moving with the stream velocity, such that properties can be defined as averages of the thermal velocities.

The pressure tensor $\mathbf{p}$ is a tensor with nine components and can be written in shorthand as:

$$\mathbf{p}_{ij} = \rho\overline{c'_i c'_j}, \tag{1.15}$$

with the subscripts i and j having three values each, representing a single component of the velocity vector each, i.e.

$$c'_1 = u', \quad c'_2 = v', \quad c'_3 = w', \tag{1.16}$$

where u, v and w are the velocity components in the x, y and z directions, respectively. The scalar pressure P is the average of the three normal components of the pressure tensor ($\mathbf{p}_{xx}$, $\mathbf{p}_{yy}$ and $\mathbf{p}_{zz}$):

$$P = \frac{1}{3}\rho\left(\overline{u'^2} + \overline{v'^2} + \overline{w'^2}\right). \tag{1.17}$$

In an equilibrium gas all three normal components of the pressure tensor are equal; in regions of non-equilibrium they will differ from one another.

The viscous stress tensor $\boldsymbol{\tau}$ is the negative of the pressure tensor with the scalar pressure subtracted from the normal components, i.e.

$$\boldsymbol{\tau} \equiv \tau_{ij} = -\left(\rho\overline{c'_i c'_j} - \delta_{ij}p\right), \tag{1.18}$$

where δ_{ij} is the Kronecker delta such that $\delta_{ij} = 1$ if $i = j$, or $\delta_{ij} = 0$ if $i \neq j$.

The average specific kinetic energy associated with the thermal velocity of a molecule can be given as

$$e_{tr} = \frac{1}{2}\left(\overline{u'^2} + \overline{v'^2} + \overline{w'^2}\right), \tag{1.19}$$

which can be combined with Equation (1.17) to give

$$P = \frac{2}{3}\rho e_{tr}. \tag{1.20}$$

This can finally be compared to the equation of state for an ideal gas to allow for the definition of a translational temperature T_{tr}:

$$T_{tr} = \frac{1}{3k_B}m\left(\overline{u'^2} + \overline{v'^2} + \overline{w'^2}\right). \tag{1.21}$$

This shows that the equation of state is valid for a dilute gas, even in a state of non-equilibrium, as long as the pressure is based only on the translational temperature. It

is also possible to define a translational temperature for each component, e.g.

$$T_{tr_x} = \frac{m}{k_B}\overline{u'^2}, \tag{1.22}$$

and the departure of each component from T_{tr} can then be used as a measure of the translational non-equilibrium.

In a dilute monatomic gas, molecules are considered to have translational temperature only, so T_{tr} is the actual temperature. However, a diatomic or polyatomic molecule will also have rotational energy (vibrational energy is ignored for now). The rotational temperature T_{rot} is defined in a manner consistent with Equation (1.21) to give

$$T_{rot} = \frac{2me_{rot}}{k_B\zeta_{rot}}, \tag{1.23}$$

where e_{rot} is the specific rotational energy and ζ_{rot} is the number of rotational degrees of freedom. In equilibrium, T_{tr} will be equal to T_{rot}. An overall temperature T_{ov} can be defined for a non-equilibrium gas as the weighted average of the translational and rotational modes;

$$T_{ov} = \frac{3T_{tr} + \overline{\zeta}_{rot}T_{rot}}{3 + \overline{\zeta}_{rot}}, \tag{1.24}$$

where $\overline{\zeta}_{rot}$ is the average number of rotational degrees of freedom. It is important to note that this overall temperature does not apply to the equation of state if the gas is in a state of non-equilibrium.

Finally, the heat flux vector $\mathbf{q}$ is defined as

$$\mathbf{q} \equiv q_i = \frac{1}{2}\rho\overline{c'^2c'_i} + n\overline{\varepsilon_{rot}c'_i}, \tag{1.25}$$

where ε_{rot} is the rotational energy of a single molecule.

1.4 Project Objectives

In this thesis, we aim to benchmark a recently developed free and open source DSMC code against existing experimental data, analytical solutions, and results from more established DSMC codes. We use the free and open source parallelised DSMC solver

dsmcFoam, that is part of the Open Field Operation and Manipulation (OpenFOAM) C++ fluid dynamics toolbox [26]. We have extended the code to include: vibrational energy, a modern approach to simulating chemical reactions, various boundary conditions and surface-molecule interaction models, and macroscopic property measurements. Finally, the code is applied to various engineering problems including micro-channels with bends, and high area-to-mass ratio spacecraft in low Earth orbit.

1.5 Key Developments

Recently, an open source DSMC code in OpenFOAM was created as a collaboration between OpenCFD Ltd and the University of Strathclyde, as a natural extension to the MD code developed by Macpherson [27]. This thesis benchmarks this new DSMC solver, named *dsmcFoam*, and provides additional functionality to greatly improve the range of applicability of this new DSMC code. These new developments enable *dsmcFoam* to take chemical reactions into account for hypersonic applications, and to be applied to low speed micro-channel simulations. In addition, some of the new measurement and control features have direct application to hybrid continuum-particle solvers. The main contributions of this work are outlined below:

- Benchmarking of the open source *dsmcFoam* solver against experimental results, independent simulation data, and hydrodynamic and kinetic theory based analytical solutions.
- Vibrational energy has been implemented within the *dsmcFoam* framework and validated accordingly, enabling the code to be used for high temperature applications where the vibrational mode is active and plays an important role in the flow characteristics.
- The modern quantum-kinetic (QK) chemical reaction model has been implemented, and the simulated chemical reaction rates for dissociation and exchange reactions are compared with theoretical predictions, other chemical reaction models, and accepted rates from the literature.
- *dsmcFoam* has been extended to include more boundary conditions, such as the

Cercignani-Lampis-Lord (CLL) surface interaction model and implicit, prescribed pressure inlets and outlets for low speed flows. The low speed pressure outlets were then extended to take rotational non-equilibrium into account.

- A robust measurement framework, based on that of the open source MD solver *mdFoam*, by Borg [28], has been implemented and various tools to measure macroscopic properties such as vibrational temperature, heat flux vector and mass flux have been implemented and validated against existing numerical results in the literature. This will be important for a Heterogeneous Multiscale Method solver that is being implemented in OpenFOAM [29].

- Detailed DSMC studies of argon gas in micro-channels with bends have been reported for the first time. The pressure and Mach number profiles are presented and compared with those of an equivalent straight micro-channel. It is found that in a small range of Knudsen number, the addition of a bend in a micro-channel system increases the amount of mass that can be carried, and that adding a second bend continues the trend. This could allow for increases in the efficiency of MEMS devices that rely on gases being delivered through micro-channels.

- Rarefied gas effects on small spacecraft characterised by a high area-to-mass ratio in low Earth orbit are considered, with the aim of taking advantage of them for position and attitude control within a swarm. DSMC simulations and analytical solutions for the drag coefficient are in excellent agreement with one another and both indicate that it is possible to change the drag coefficient by controlling the temperature of the spacecraft.

1.6 Published papers

The work from this thesis has contributed to the following peer reviewed research papers:

1. Craig White, Matthew K. Borg, Thomas J. Scanlon and Jason M. Reese. An investigation of micro-channel gas flows with bends using DSMC, *Computers & Fluids*, 71:261–271 2013.

2. Craig White, Camilla Colombo, Thomas J. Scanlon, Colin R. McInnes and Jason M. Reese. Rarefied gas effects on the aerodynamics of high area-to-mass ratio spacecraft in orbit, *Advances in Space Research*, 51(11):2112–2124, 2013.

3. Nishanth Dongari, Craig White, Thomas J. Scanlon, Yonghao Zhang and Jason M. Reese. Effects of curvature on rarefied gas flows between rotating concentric cylinders, *Physics of Fluids*, in press, 2013.

4. Craig White, Matthew K. Borg, Thomas J. Scanlon and Jason M. Reese. Accounting for rotational non-equilibrium effects in subsonic DSMC boundary conditions, *Journal of Physics: Conference Series*, 362:012016, 2012.

5. Thomas J. Scanlon, Ehsan Roohi, Craig White, Masoud Darbandi and Jason M. Reese. An open source, parallel DSMC code for rarefied gas flows in arbitrary geometries, *Computers & Fluids*, 39(10):2078-2089, 2010.

6. Thomas J. Scanlon, Craig White, Matthias Schuebler, Richard E. Brown and Jason M. Reese. Thermochemistry modelling in an open source DSMC code, *Proceedings of the 28th International Symposium on Shock Waves*, Part III, 145–151, 2011.

7. Nam T. P. Le, Craig White, Jason M. Reese and Rho S. Myong. Langmuir-Maxwell and Langmuir-Smoluchowski boundary conditions for thermal gas flow simulations in hypersonic aerodynamics, *International Journal of Heat and Mass Transfer*, 55(19–20):5032–5043, 2012.

8. Nishanth Dongari, Craig White, Thomas J. Scanlon, Yonghao Zhang and Jason M. Reese. Rarefaction effects in gas flows over curved surfaces, *Proceedings of the 28th International Symposium on Rarefied Gas Dynamics: AIP Conference Proceedings*, 1501:778–785, 2012.

9. Lei Wu, Craig White, Thomas J. Scanlon, Jason M. Reese and Yonghao Zhang. Deterministic numerical solutions of the space-inhomogeneous Boltzmann equation using the fast spectral method, *Journal of Computational Physics*, under review, 2013.

Chapter 2

Direct Simulation Monte Carlo

DSMC is computationally intensive but ...
the difficulties are habitually overstated.
- Graeme A. Bird [30]

The direct simulation Monte Carlo method, pioneered by Bird, has emerged over the past 50 years as the dominant numerical technique for simulating rarefied gas flows in the transition regime. It is a stochastic particle-based technique, and the fundamental idea is to track a number of statistically representative particles in time and space, while modifying their velocities and positions in a manner that provides a statistical representation of a real gas. A single DSMC simulator particle can represent any number of real gas molecules, which can be used to reduce the computational expense of all but the most intensive simulations to a level manageable for most modern computers.

The method is based on the decoupling of the particle movements and collisions over small time intervals. Movements are handled in a deterministic manner according to their individual velocity vectors and the time step. Collisions are then dealt with in a stochastic manner after all particle positions have been updated. Since the method is based on kinetic theory, it has the same limitations, i.e. the gas must be dilute and Boltzmann's molecular chaos assumption must hold. Although the method attempts to emulate the physics of a real gas rather than provide an analytical solution to the Boltzmann equation, it is now widely accepted that DSMC is the most reliable method for solving transition regime problems and any newly-proposed methods are frequently

benchmarked against DSMC data.

A computational mesh is required for the DSMC method to recover macroscopic properties, but it also used to perform near-neighbour collisions. In order to ensure collisions are as realistic as possible, the usual recommendation is that the cell size is one third of the local mean free path. For the assumption of uncoupled particle collisions and movements to be valid, it important to ensure that the time step is significantly smaller than the mean collision time t_{mc}.

DSMC is reasonably computationally expensive due to the need to track a large number of particles, compute a potentially large number of collisions, and perform a large number of time steps in order to reduce the statistical scatter to an acceptable level. However, with modern computational advances and the advent of parallel processing and high performance computers, the method is now reasonably accessible to most users.

The first DSMC paper was published by Bird in 1963 [31] and deals with the relaxation of hard sphere particles to a Maxwellian speed distribution from an initial state of every particle having an equal velocity. This paper repeats the deterministic molecular dynamics simulations of Alder & Wainwright [32] using a stochastic method that allowed for a five fold increase in the size of the system. In this early work, only the particle velocities were stored and the collision probability for a randomly selected pair of particles was calculated based on the relative velocity of the pair. This procedure for deciding on what particles to collide endures to the present day. Bird quotes the Silliac computer at the University of Sydney performing a total of 30,000 collisions per compute hour for a system with 500 DSMC simulator particles in 1963.

The first non-trivial application of the DSMC method was in the study of shockwave structures of both single species [33, 34] and gas mixtures [35]. By this time, the idea of a single DSMC particle representing a large number of real molecules had been introduced. Soon after, the first studies involving diatomic molecules were performed by Bird [36], studying the breakdown of both translational and rotational equilibrium in gaseous expansion. By 1970, Bird was quoting run times of 40 seconds to perform 12,000 collisions in a system with 1,600 DSMC particles on an IBM 360-75. All of this work was restricted to hard sphere and Maxwell molecules. In the case of diatomic

molecules, the unrealistic rough sphere molecular model was used. The main challenge facing the DSMC method at this time was showing how it was related to the Boltzmann equation and that results from DSMC could be considered a solution to the Boltzmann equation [37].

Despite scepticism about the relationship to the Boltzmann equation [38, 39], the DSMC method grew in popularity during the 1970s, driven by the aerospace sector. The increase in the number of users led to several notable improvements being made in the following decades. A phenomenological model for the redistribution of energy between translational and rotational modes was introduced in 1975 by Borgnakke & Larsen [40]. Phenomenological models use the simplest possible mathematical model of a process at the molecular level to reproduce important gas effects, and they have become important and popular in DSMC since the introduction of the Larsen-Borgnakke model [38]. The variable cross-section hard sphere (VHS) model introduced by Bird [41] relates the collision cross-section of a colliding particle pair to their relative velocity and has been shown to produce values of mean free path and viscosity that are in agreement with experimental results.

Two final important additions to the DSMC method was Bird's 'no-time-counter' (NTC) method [42] for returning the correct collision rates with minimal computational effort, and the sub-cell technique [21]. In the sub-cell technique each computational cell is split into multiple sub-cells when selecting collision partners and only particles within the same virtual sub-cell are allowed to collide with one another. This increases the physical realism of the simulation further by promoting nearest neighbour collisions.

In 1992, a mathematical proof that the DSMC method provides a solution to the Boltzmann equation for a monatomic gas in the limiting case of an infinite number of particles [39] was published, finally removing the ambiguity over how DSMC related to the Boltzmann equation. The DSMC method has been comprehensively described in Bird's 1994 monograph [21].

2.1 The DSMC Algorithm

Figure 2.1 is a flowchart of the basic algorithm followed by all DSMC solvers. After defining the gas species properties, boundary conditions and the number of real

molecules each DSMC particle represents F_N, the first step is to populate the computational mesh with DSMC particles. User-defined values of macroscopic density, temperatures and velocity can be used to calculate the number of DSMC particles to insert in each cell, and the thermal velocities are selected from the equilibrium Maxwell-Boltzmann distribution at the prescribed translational temperature. If rotational and vibrational energy are required, they are selected using the prescribed rotational and vibrational temperatures. For details of sampling from the relevant distribution functions see Appendix C of Ref. [21].

2.1.1 Particle Movement

Next, the main loop of the DSMC algorithm begins. Particles are first inserted at inlet boundaries based on the equilibrium Maxwellian number flux across a boundary $\dot{N}_{in}$:

$$\dot{N}_{in} = \frac{n_{in}}{\beta\left(2\pi^{1/2}\right)}\left[\exp\left(-s^2\cos^2\theta\right) + \pi^{1/2} s\cos\theta\left\{1+\operatorname{erf}\left(s\cos\theta\right)\right\}\right], \tag{2.1}$$

with

$$\beta = \left\{m/\left(2k_B T_{in}\right)\right\}^{1/2}, \tag{2.2}$$

and

$$s = c_{0_{in}}\beta, \tag{2.3}$$

where the subscript in denotes properties at an inlet face and θ is the angle between the velocity vector $\mathbf{c}_{0_{in}}$ and the inlet face.

All particles are moved according to their velocity vector and the time step. During this stage, any interactions with boundaries are also handled, e.g. moving from one processor to another, reflecting from a surface according to molecule-surface interaction (e.g. Maxwellian diffuse or specular reflection), or leaving the system at a deletion boundary. Macroscopic properties at solid boundaries are calculated during this step, generally as a function of the difference in the pre- and post-interaction properties (momentum and/or energy) of particles that are incident at the boundary.

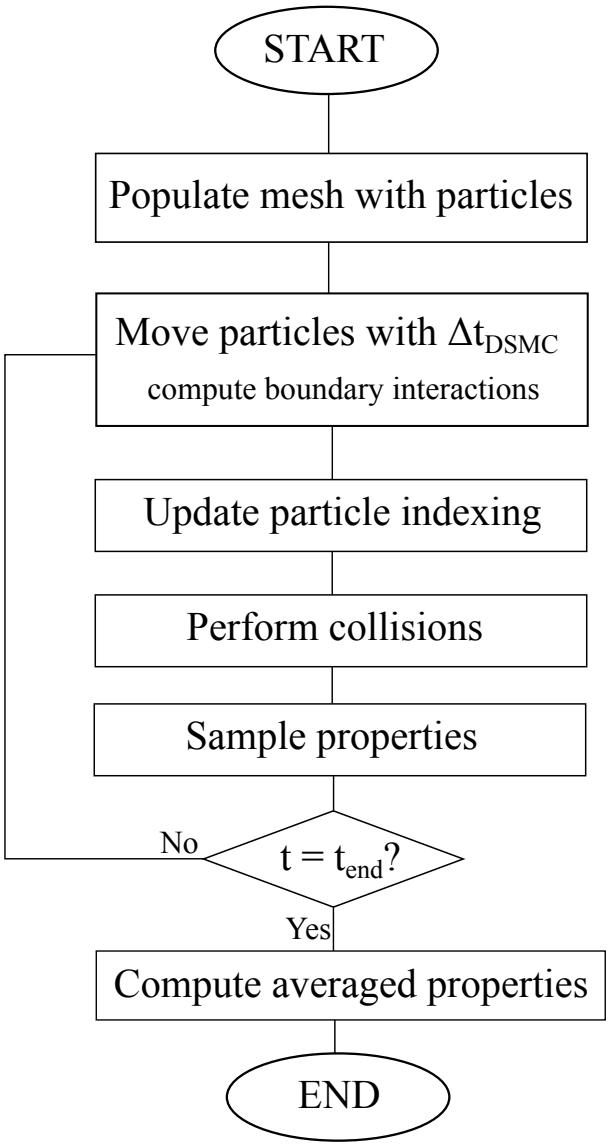

Figure 2.1: Flowchart of the standard DSMC algorithm.

2.1.2 Collision Procedure

Once all of the particles have been moved, it is necessary to re-index them before beginning the collision routine, as the collision and sampling routines depend on information about each cell's current occupancy. Performing the collisions comes next. This is done in a probabilistic manner, setting DSMC apart from deterministic techniques like MD. There are various methods for ensuring the correct number of collisions are performed to remain consistent with theory [43, 44], but the current standard is Bird's NTC scheme [21, 42]. The sub-cell technique [21], or more modern transient-adaptive sub-

cell techniques [45], are used to promote nearest neighbour collisions. The probability P_{coll} of particle i colliding with particle j within a cell is

$$P_{coll}\left[i,j\right] = \frac{\left|\mathbf{c}_i - \mathbf{c}_j\right|}{\sum_{m=1}^{N}\sum_{n=1}^{m-1}\left|\mathbf{c}_m - \mathbf{c}_n\right|}, \tag{2.4}$$

where N is the instantaneous number of DSMC particles in the cell. This would be computationally expensive to calculate for each pair and so an acceptance-rejection scheme is used to choose which pairs collide. The NTC method is that

$$\frac{1}{2V_C} F_N N\left(N-1\right)\left(\xi_T c_r\right)_{max} \Delta t_{DSMC} \tag{2.5}$$

pairs are selected from a cell at a given time step, where V_C is the cell volume, $\left(\xi_T c_r\right)_{max}$ is the maximum product of collision cross-section and relative speed of all possible particle pairs in the cell and Δt_{DSMC} is the time step size. Particle i is chosen at random from all particles in the cell and j is chosen from the same sub-cell to ensure near neighbour collisions. Each collision pair is then tested using the acceptance-rejection method [21, 25], i.e. the collision is accepted if

$$\frac{\left(\xi_T c_r\right)_{ij}}{\left(\xi_T c_r\right)_{max}} > R_f, \tag{2.6}$$

where R_f is a random fraction uniformly chosen in $[0, 1)$.

Once a particle pair have been selected for collision, they must be 'collided'. In DSMC, collisions are simulated simply by resetting the velocities of both partners in the collision pair; their positions are not altered. We will firstly consider elastic collisions, which occur between particles that are not exchanging rotational or vibrational energy. In order to conserve momentum and energy, we therefore know that

$$\mathbf{c}_{cm} = \frac{m_i\mathbf{c}_i + m_j\mathbf{c}_j}{m_i + m_j} = \frac{m_i\mathbf{c}_i^* + m_j\mathbf{c}_j^*}{m_i + m_j} = \mathbf{c}_{cm}^*, \tag{2.7}$$

and

$$c_r = \left|\mathbf{c}_i - \mathbf{c}_j\right| = \left|\mathbf{c}_i^* - \mathbf{c}_j^*\right| = c_r^*, \tag{2.8}$$

where $\mathbf{c}_{cm}$ is the centre of mass velocity and the superscript $*$ denotes post-collision properties. Using Equations (2.7) and (2.8), along with an equation for the scattering angles, it is possible to solve for $\mathbf{c}_r^*$. The scattering angles, ϑ and ϕ, are uniformly distributed over a unit sphere, between 0 and 2π radians. The asimuthal angle, ϕ is simply given as

$$\phi = 2\pi R_f. \tag{2.9}$$

The elevation angle, ϑ, is distributed with a probability $P(\vartheta)\, d\vartheta = \frac{1}{2}\sin\theta d\theta$. Using the change of variable $q = \sin\vartheta$, we have $P(q)\, dq = \frac{1}{2} q dq$, and q is uniformly distributed in the interval [-1,1) [25]. Then q can be found as

$$q = 2R_f - 1 \quad \text{and} \quad \vartheta = \cos^{-1} q. \tag{2.10}$$

The three components of the post-collision relative velocity are defined as

$$\mathbf{c}_r^* = c_r^* \left[(\sin\vartheta\cos\phi)\,\hat{\mathbf{x}} + (\sin\vartheta\sin\phi)\,\hat{\mathbf{y}} + \cos\vartheta\hat{\mathbf{z}} \right], \tag{2.11}$$

and the post-collision velocities become

$$\begin{aligned} \mathbf{c}_i^* &= \mathbf{c}_{cm}^* + \left(\frac{m_j}{m_i + m_j}\right)\mathbf{c}_r^*, \\ \mathbf{c}_j^* &= \mathbf{c}_{cm}^* - \left(\frac{m_i}{m_i + m_j}\right)\mathbf{c}_r^*. \end{aligned} \tag{2.12}$$

In the case of diatomic molecules with rotational energy, inelastic collisions must take place in order to exchange energy between the translational and rotational modes. In DSMC, the most common method of exchanging rotational energy is the phenomenological Larsen-Borgnakke model [40]. To capture a realistic rate of rotational relaxation, the Larsen-Borgnakke model only treats a certain fraction of collisions as inelastic. For nitrogen gas at around 273 K, it has been found that a rotational relaxation number Z_{rot} of 5 returns relaxation rates in good agreement with experimental data. When a collision is accepted, it is first checked for rotational relaxation and is accepted if

$$\frac{1}{Z_{rot}} > R_f, \tag{2.13}$$

and the particle is assigned a new rotational energy. In order to conserve energy, the total translational energy available to the particle pair is decreased accordingly and a new post-collision relative speed c_r^* is calculated as

$$c_r^* = \sqrt{\frac{2\varepsilon_{tr}}{m_r}}, \tag{2.14}$$

where ε_{tr} is the total translational energy available to the collision pair after the adjustment for rotational relaxation has taken place, and m_r is the reduced mass of the collision pair. The remainder of the collision process proceeds as from Equation (2.9) above.

2.1.3 Sampling and Averaging

The aim of any engineering-based DSMC simulation is to recover macroscopic flow properties. In order to do so, it is necessary to sample the particle properties after all of the collisions have been processed. The sampling procedure is largely the same as described in §1.3.2, but care has to be taken to account for the fact that a single DSMC particle can represent any number of real molecules. For example, number density is sampled as

$$n = \frac{F_N \overline{N}}{V_C}, \tag{2.15}$$

where F_N is the number of real molecules that a DSMC particle represents, $\overline{N}$ is the average number of DSMC particles in the cell during the measurement interval, and V_C is the cell volume.

A steady state problem is allowed to reach its steady state, then properties are measured over a large enough sample size to reduce the statistical error to an acceptable level, which can be estimated using equations in Reference [46]. For a transient problem, the simulation must be repeated enough times to provide a large enough sample and the results can then be presented as an ensemble average.

2.2 DSMC Codes

Here, we give a brief overview of some of the available DSMC codes and their capabilities, followed by a more detailed description of the software used in this thesis. The list of available DSMC codes here is by no means exhaustive.

2.2.1 DS1V, DS2V and DS3V

These are Bird's DSMC codes and are available to download from his website [47]. DS1V is the one-dimensional version of the code and includes support for both steady and unsteady planar, spherical, or cylindrical flows. It is mainly used to test new DSMC procedures. All of the Fortran source code is freely available for this version of Bird's code.

DS2V is the two-dimensional version and is the most advanced of Bird's codes, being described as a "well established commercial quality" code [47]. It includes a graphical user interface (GUI) and supports plane or axially symmetric problems. Unlike DS1V, this is not a 64-bit program and so is subject to some problems with round-off errors. The code includes all of the latest "sophisticated DSMC" procedures described in Reference [30], such as automatically adjusting the cell size as a function of local mean free path during the simulation. The code reports to the user on the quality of the simulation based on various parameters, e.g. cell size and collision quality.

DS3V is a three-dimensional version of the solver and is very similar in capability to DS2V, but it does not have such an advanced GUI. Both DS2V and DS3V are free to download and use, but the source code for them is not currently available.

2.2.2 MONACO

The MONACO code has been developed by Iain D. Boyd at the University of Michigan [48, 49] since 1996 and is now a mature, parallelised DSMC code. Key features include:

- arbitrary 2D/3D geometry capability,
- structured/unstructured meshes,
- multi-species capability,

- Total Collision Energy (TCE) chemical reaction model [50].

The MONACO code is restricted to use within the United States and is therefore not available to us at the University of Strathclyde.

2.2.3 SMILE

Statistical Modeling in Low-Density Environment (SMILE) [51] is a parallel DSMC code developed at the Laboratory of Computational Aerodynamics from the Khristianovich Institute of Theoretical and Applied Mechanics of the Siberian Branch of the Russian Academy of Sciences. Key features of SMILE include:

- arbitrary 2D/3D/axi-symmetric geometry capability,
- multi-species capability,
- TCE chemical reactions [50] with extendible chemical species database,
- majorant frequency scheme collision partner selection routine [43].

The SMILE code does not appear to be readily distributed.

2.2.4 *dsmcFoam*

The DSMC solver that we use throughout this thesis is *dsmcFoam*. The code has been developed within the framework of the open source CFD toolbox OpenFOAM [26]. The code was written, with collaboration from researchers at the University of Strathclyde, by OpenCFD Ltd. OpenFOAM is a flexible set of efficient, object-oriented C++ modules for solving complex fluid flows, and is primarily a Compuational Fluid Dynamics (CFD) package, but it does include both MD and DSMC solvers. It is freely available and open source under the GNU general public licence. A MD code contained within OpenFOAM [27, 28] was modified to generate the DSMC capability. Fundamental features of the existing MD code, including particle initialisation in arbitrary geometries and particle tracking in unstructured, arbitrary, polyhedral meshes, are among the core elements of the *dsmcFoam* code.

All of the OpenFOAM modules are fully parallelised and the free and open source philosophy of the software eliminates the need for expensive licence fees. Therefore,

the only constraint on how many cores can be used in a parallel *dsmcFoam* simulation is the number of cores available to the user, and the scaling performance of the solver and the current problem. Powerful meshing tools are also provided with OpenFOAM, allowing for the building of structured and unstructured meshes for use with DSMC simulations. Results can be post-processed using the Paraview software provided with OpenFOAM, or with a variety of other post-processing software, such as Tecplot. Key features of the *dsmcFoam* solver as included with OpenFOAM are:

- steady state or transient simulations,
- unlimited parallel processing capability,
- arbitrary 2D/3D geometries,
- structured/unstructured meshes,
- automatic 8 sub-cell generation to promote nearest neighbour collisions,
- arbitrary number of gas species,
- free-stream flow boundaries,
- Maxwellian diffuse or specular surface interactions,
- no-time-counter collision partner selection,
- rotational energy mode,
- Larsen-Borgnakke rotational energy redistribution,
- variable hard sphere collision model,
- cyclic (periodic) boundaries.

These are all essential features of any modern DSMC code, but the standard *dsmcFoam* code is lacking in some features to make it of use for solving certain practical engineering problems, such as a vibrational mode and chemical reactions. However, the open source philosophy employed by OpenFOAM means it is possible for users to extend the code themselves to add any desired functionality. The work described in this thesis will attempt to deal with these weaknesses in the *dsmcFoam* solver.

In addition to the core *dsmcFoam* solver, there are two other important supporting executables included in OpenFOAM. The first is *dsmcInitialise*, which is an application used to populate the mesh with DSMC simulator particles. After the simulation is complete, the *dsmcFieldsCalc* utility can be called to calculate intensive fields such as temperature and pressure. These intensive fields do not need to be sampled while the simulation is running, as they can easily be recovered from time/ensemble averaged extensive fields such as mass, momentum and energy once the simulation is complete. This allows for a small reduction in the computational expense of sampling macroscopic properties. Running a steady state DSMC simulation with *dsmcFoam* therefore consists of the following steps:

1. Build computational mesh.
2. Set up species properties, boundary conditions and time step size.
3. Populate mesh with DSMC particles using *dsmcInitialise*.
4. Begin the simulation with *dsmcFoam*.
5. Start time averaging once a steady state solution has been reached.
6. Perform post-processing with *dsmcFieldsCalc*.

Since *dsmcFoam* is a new DSMC solver, it is important to determine the accuracy of the code before extending it. In the following chapter we benchmark *dsmcFoam* against analytical solutions, experimental results and existing results from established DSMC solvers.

Chapter 3

Benchmarking *dsmcFoam*

Testing, we will never do enough of it.

- Greg LeMond

Since *dsmcFoam* is a new DSMC code, it is important that we rigorously test the code, and compare results from it against experimental data, analytical solutions, and numerical results from other DSMC solvers. In this chapter, we perform a variety of benchmark cases in order to make these comparisons.

3.1 Collision Rates

It is of fundamental importance to verify that the no-time-counter implementation within *dsmcFoam* returns collision rates that are in agreement with analytical solutions. Here, we test three cases in order to validate that *dsmcFoam* calculates correct collision rates. We use a slightly modified version of the *dsmcFoam* solver for these cases. The particles do not move in this version of the code and they do not collide; however, the probability of them colliding is still calculated and if the collision is 'accepted' the counter is updated, allowing for collision rates to be measured for an equilibrium system with no gradients.

All of the cases are simple adiabatic box single cell simulations. The cell is cubic with a volume of 1.97×10^{-5} m^3, the time step employed for all cases is 1×10^{-7} s and each DSMC simulator particle represents 2×10^8 real particles. The number densities and gas species for each case are outlined in Table 3.1. Cases I and II contain around

1 million DSMC particles and Case III has around 2 million. The number of collisions is counted for a total of 1000 time steps for all cases.

Case	n_{O_2} (m^{-3})	n_{N_2} (m^{-3})
I	1×10^{19}	0
II	0	1×10^{19}
III	1×10^{19}	1×10^{19}

Table 3.1: Number densities for the collision rate test simulations.

	O_2	N_2
T_{ref} (K)	273	273
d_{ref} (m)	4.07×10^{-10}	4.17×10^{-10}
m (kg)	53.12×10^{-27}	46.5×10^{-27}
ω	0.77	0.74

Table 3.2: Molecular properties for the collision rate test simulations.

We compare the equilibrium collision rates $(N_{pq})_0$ reported by *dsmcFoam* to the exact analytical expression as given in Equation 4.78 of Bird [21]:

$$(N_{pq})_0 = 2\pi^{\frac{1}{2}} (d_{ref})_{pq}^2 n_p n_q \{T/(T_{ref})_{pq}\}^{1-\omega_{pq}} \{2k_B (T_{ref})_{pq}/m_r\}^{\frac{1}{2}}, \tag{3.1}$$

where p and q represent different species and the subscript 0 denotes equilibrium quantities, d_{ref}, T_{ref} and ω are the VHS parameters for reference diameter, reference temperature and viscosity exponent, respectively, n is number density, k_B is the Boltzmann constant, T is temperature, and m_r is reduced mass. Equation (3.1) returns the number of collisions per unit volume per second, although it double counts because it calculates collisions between pq and qp; therefore, if a same species collision calculation is being performed it is necessary to include a factor of a half in order to achieve the correct rate.

Figure 3.1 shows the analytical rate for Case I, pure oxygen, compared with the results from the *dsmcFoam* simulation. Since only single species collisions are involved, the analytical rate is multiplied by the necessary symmetry factor of a half, i.e.:

$$(N_{O_2})_0 = \pi^{\frac{1}{2}} (d_{ref})_{O_2}^2 n_{O_2} n_{O_2} \{T/(T_{ref})_{O_2}\}^{1-\omega_{O_2}} \{2k_B (T_{ref})_{O_2}/m_{r_{O_2}}\}^{\frac{1}{2}}. \tag{3.2}$$

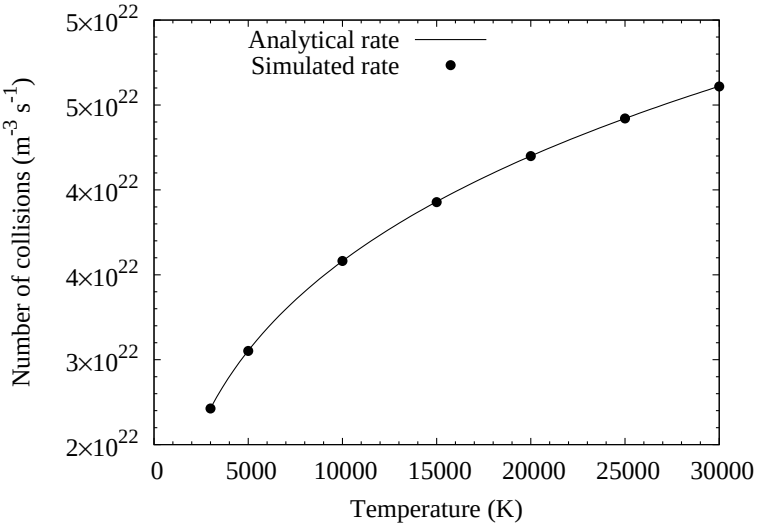

Figure 3.1: Collision rate variation with temperature for Case I, pure oxygen. *dsmcFoam* results are compared to the analytical solution of Equation (3.1).

Temperature (K)	Simulated/Analytical Rate	% Error
3000	0.9992	0.0767
5000	0.9995	0.0487
10000	1.0002	-0.0227
15000	0.9993	0.0653
20000	0.9999	0.0104
25000	0.9999	0.0085
30000	0.9997	0.0263

Table 3.3: Simulated rates compared with analytical values for oxygen.

Excellent agreement is found between the simulated and analytical rates. Table 3.3 shows the relative errors in the values of the simulated rates compared to the analytical solution. All of the errors are smaller than 0.1%, indicating that the collision rates obtained from *dsmcFoam* are in excellent quantitative agreement with the analytical rates.

Figure 3.2 shows the simulated *dsmcFoam* results compared to the analytical solution for Case II, pure nitrogen, and Table 3.4 shows the errors. Very similar to the case with oxygen, excellent agreement is found.

Figure 3.3 shows the simulated *dsmcFoam* results compared to the analytical solution for the gas mixture, Case III. The analytical solution takes into account that there are three possible types of collisions in this gas mixture of nitrogen and oxygen, and is

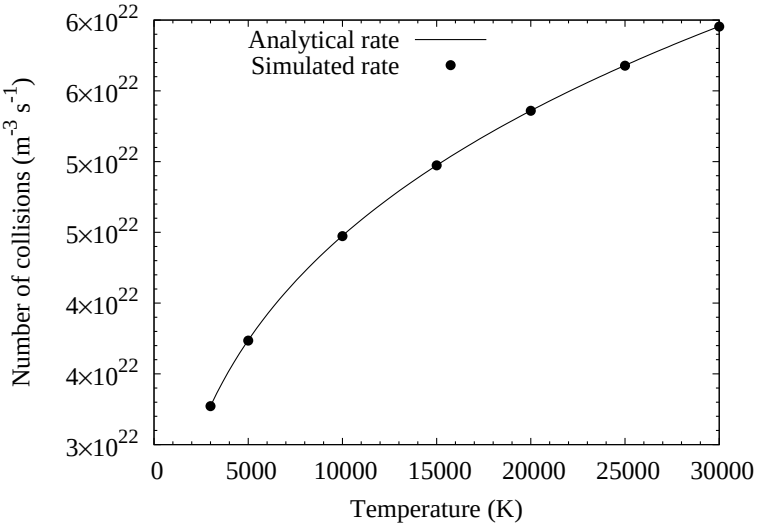

Figure 3.2: Collision rate variation with temperature for Case II, pure nitrogen. *dsmcFoam* results are compared to the analytical solution of Equation (3.1).

Temperature (K)	Simulated/Analytical Rate	% Error
3000	0.9998	0.0224
5000	0.9992	0.0773
10000	0.9994	0.0639
15000	1.0000	0.0048
20000	0.9998	0.0163
25000	0.9997	0.0348
30000	0.9998	0.0234

Table 3.4: Simulated rates compared with analytical values for oxygen.

Temperature (K)	Simulated/Analytical Rate	% Error
3000	1.0000	0.0035
5000	0.9998	0.0225
10000	0.9995	0.0462
15000	0.9994	0.0610
20000	0.9993	0.0693
25000	0.9995	0.0467
30000	0.9995	0.0522

Table 3.5: Simulated rates compared with analytical values for oxygen-nitrogen mixture.

calculated as:

$$
\begin{aligned}
(N_{N_2O_2})_0 &= \pi^{\frac{1}{2}} (d_{ref})^2_{O_2} n_{O_2} n_{O_2} \{T/(T_{ref})_{O_2}\}^{1-\omega_{O_2}} \{2k_B (T_{ref})_{O_2} / m_{r_{O_2}}\}^{\frac{1}{2}} \\
&+ \pi^{\frac{1}{2}} (d_{ref})^2_{N_2} n_{N_2} n_{N_2} \{T/(T_{ref})_{N_2}\}^{1-\omega_{N_2}} \{2k_B (T_{ref})_{N_2} / m_{r_{N_2}}\}^{\frac{1}{2}} \\
&+ \left[2\pi^{\frac{1}{2}} (d_{ref})^2_{N_2O_2} n_{N_2} n_{O_2} \{T/(T_{ref})_{N_2O_2}\}^{1-\omega_{N_2O_2}} \right. \\
&\quad \left. \{2k_B (T_{ref})_{N_2O_2} / m_{r_{N_2O_2}}\}^{\frac{1}{2}}\right]. \qquad (3.3)
\end{aligned}
$$

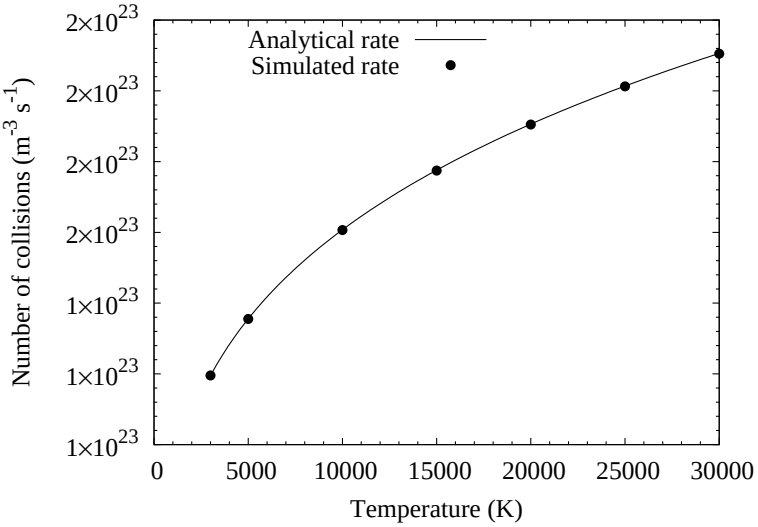

Figure 3.3: Collision rate variation with temperature for Case III, 50% nitrogen, 50% oxygen. *dsmcFoam* results are compared to the analytical solution of Equation (3.1).

3.1.1 Conclusions

Excellent agreement between the analytical solution for the collision rate in an equilibrium gas and the collision rates from *dsmcFoam* for both single species and a gas mixture is found. This demonstrates that the no-time-counter method is implemented correctly in *dsmcFoam* and that the code can be used with confidence that it is returning physically realistic collision rates.

3.2 Maxwell Gas-Surface Interactions

Gas-surface interactions provide boundary conditions in DSMC simulations. The most commonly used interaction model is a mixture of Maxwell's diffuse and specular reflections [8], where a specular reflection involves the normal component of the particle velocity being inverted while the energy and tangential velocity components are unaltered; this represents a perfectly smooth surface. A diffuse reflection represents a microscopically rough surface, and a particle's post-interaction velocity is not related to its pre-interaction velocity. The post-interaction speed is chosen according to the surface temperature, and the direction of the velocity vector is chosen with equal probability in all directions. Figure 3.4 shows a sketch of both types of surface interaction.

An accommodation coefficient σ_M, also known as Maxwell's fraction, is introduced

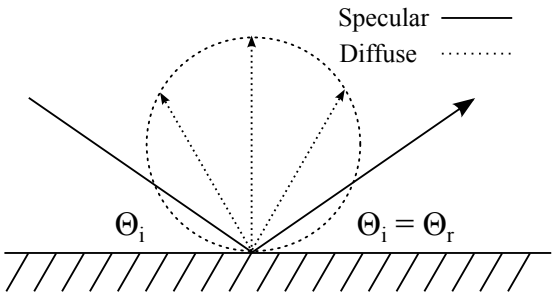

Figure 3.4: Sketch of Maxwell's diffuse and specular type gas-surface interactions.

to model real surfaces. The value of σ_M defines the fraction of molecules that interact with the surface in a diffuse manner; the remaining molecules undergo specular interactions. *dsmcFoam* has a `mixedDiffuseSpecular` type surface boundary condition, and we benchmark this here against an analytical solution for the post-collision scattering angles of a fully diffuse surface, along with numerical solutions for various values of σ_M.

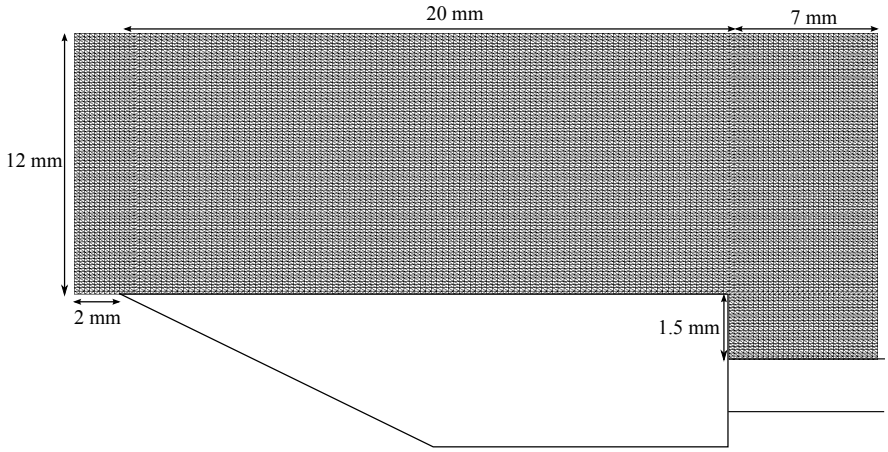

Figure 3.5: Schematic of the simulated flat plate geometry with our 2D DSMC mesh.

Our results for the scattering angle of DSMC particles incident at two positions on a flat plate in a rarefied hypersonic flow are compared to those from MONACO [52, 53]. A 2-dimensional flat plate geometry is simulated; the plate is 20 mm in length, with a 2 mm freestream region upstream of the plate and a 7 mm expansion region behind the plate. A schematic of the simulated flat plate with our mesh overlain is shown in Figure 3.5.

The working gas is nitrogen, although the vibrational mode is not considered in this work. The VHS collision model is used in our *dsmcFoam* simulations, with $\omega = 0.7$ and

$d_{ref} = 4.11 \times 10^{-10}$ m. Energy is exchanged between the rotational and translational modes using the Larsen-Borgnakke model, with a constant relaxation number Z_{rot} of 5. The flat plate has constant surface temperature of 300 K and the freestream gas temperature is 9 K. The freestream velocity component perpendicular to the flat plate varies from 20 m/s at the same height as the flat plate, to 160 m/s at the furthest point from the plate. The component of the freestream velocity parallel to the plate is constant at 725 m/s, giving a freestream Mach number of around 12. The freestream number density is 7.1×10^{21} m^{-3}, giving a Knudsen number of 0.0048 based on the VHS mean free path and the plate length. We use a cell size about the size of the freestream mean free path and 8 sub-cells per computational cell ensure the collisions are performed adequately; a similar cell size was used by Padilla & Boyd [53], and their sensitivity study found that this cell size is adequate. Our time step was 5×10^{-8} s, which is much smaller than the mean collision time of 1.3×10^{-6} s.

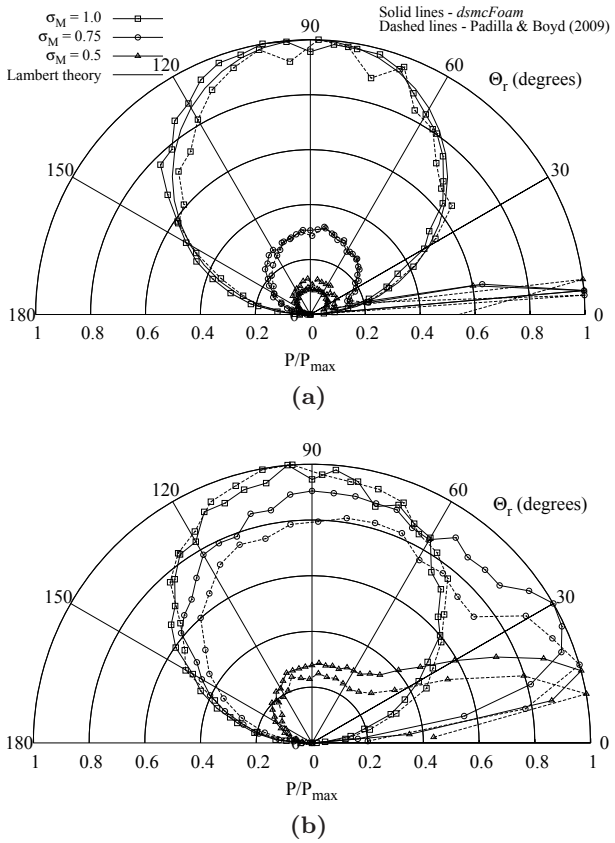

Figure 3.6: Maxwellian scattering angles Θ_r for different values of Maxwell's fraction at (a) 0 mm, and (b) 5 mm positions on the flat plate surface.

We model the plate's surface as a Maxwellian wall, for several different values of σ_M. For each case, the scattering angles of each particle are recorded at two stations on the flat plate surface: at the leading edge of the plate (0 mm), and at a position 5 mm from the leading edge. Our *dsmcFoam* results are compared to those from MONACO. Also included is an analytical solution for the scattering angle probability for a fully diffuse surface. This is from Lambert's cosine distribution of optics theory for light reflecting from a fully diffuse surface, but it also applies to the scattering angle probability distribution of a fully diffuse gas-surface interaction.

The scattering angle probability plots are shown in Figure 3.6. The cosine law solution is also plotted in Figure 3.6(a) and is in excellent agreement with both the MONACO and *dsmcFoam* results for $\sigma_M = 1$. The MONACO and *dsmcFoam* results are in reasonable agreement for the lower accommodation coefficients.

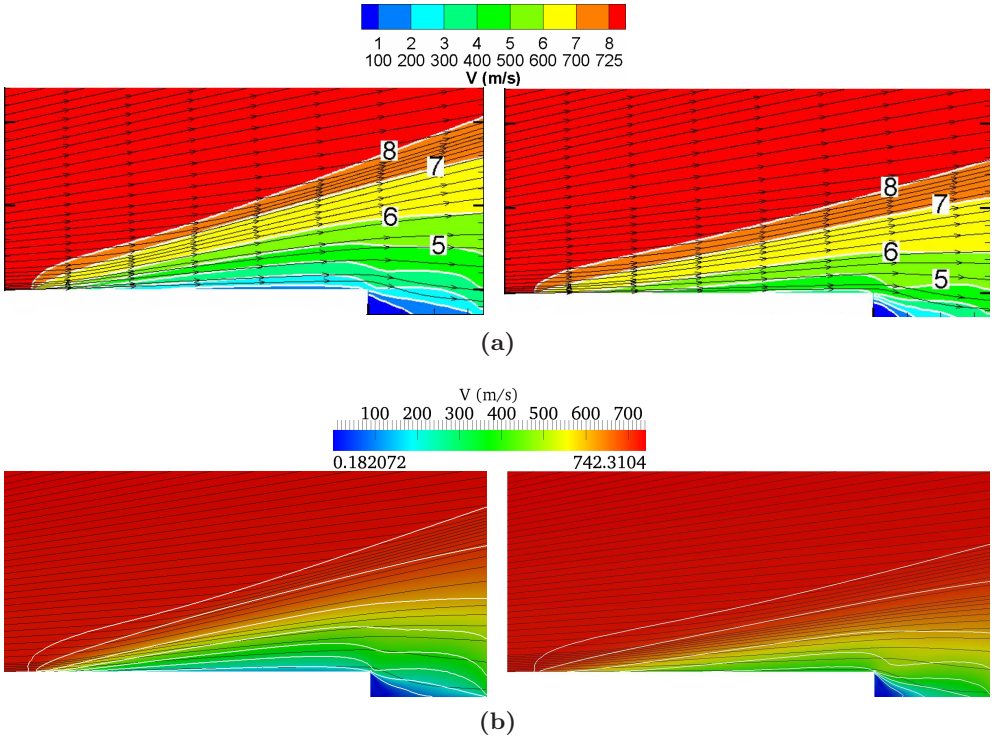

Figure 3.7: Contours of velocity with velocity streamlines from (a) MONACO [52], and (b) *dsmcFoam* for two different values of Maxwell's fraction. Left: $\sigma_M = 1$. Right: $\sigma_M = 0.5$

Contours of velocity with velocity streamlines from *dsmcFoam* are compared with results from MONACO [52] in Figure 3.7. Good qualitative agreement is found for both values of σ_M considered. The cases were solved in parallel on 4 cores of a desktop

PC with an Intel i7 processor. At steady state there were around 1.2 million DSMC particles in the $\sigma_M = 1$ case and a run time of 10 hours produced a sample size of 50,000.

3.3 Supersonic Corner Flow

This benchmark case considers supersonic flow of argon gas in the 'corner' between two flat plates that are perpendicular to one another, and parallel to the incoming stream flow. This is one of Bird's three-dimensional flow example cases and can be found on page 394 of Reference [21]. Both plates are 0.25 m in length and 0.18 m wide. There is a 0.05 m upstream region before the plates. The stream is argon gas with temperature T_∞ of 300 K, number density n_∞ of 1×10^{20} m^{-3}, and Mach 6. The plate temperature is 1000 K and all gas-surface interactions are considered to be fully diffuse. The variable hard sphere mean free path λ_{VHS} [41],

$$\lambda_{VHS} = \frac{\frac{2\mu}{15}(7-2\omega)(5-2\omega)}{\rho\sqrt{2\pi RT}}, \tag{3.4}$$

is 1.33×10^{-2} m, giving a Knudsen number of 0.053 based on the plate length of 0.25 m, where R is the specific gas constant. A mesh with $60 \times 36 \times 36$ computational cells was used, giving a mesh size that is 0.38 times the mean free path, meeting good DSMC practice. The VHS parameters used for argon are: reference temperature T_{ref} = 273 K, reference diameter $d_{ref} = 4.17 \times 10^{-10}$ m and viscosity exponent $\omega = 0.81$. Figure 3.8 shows the mesh generated in OpenFOAM. The surface of the plates are shown in solid grey, and the mesh itself is shown as a wireframe.

We initialise the system uniformly with around 21 DSMC particles per cell at the freestream properties, giving a total of 1.62 million particles in the system initially. The time step chosen for our simulation is 5×10^{-7} s; this is considerably smaller than the mean collision time t_{mc} of 3.77×10^{-5} s and is also small enough to ensure that particles are likely to remain within a single computational cell for multiple time steps. The VHS collision model is used and each cell is split into eight virtual sub-cells (two in each direction) during the collision routine.

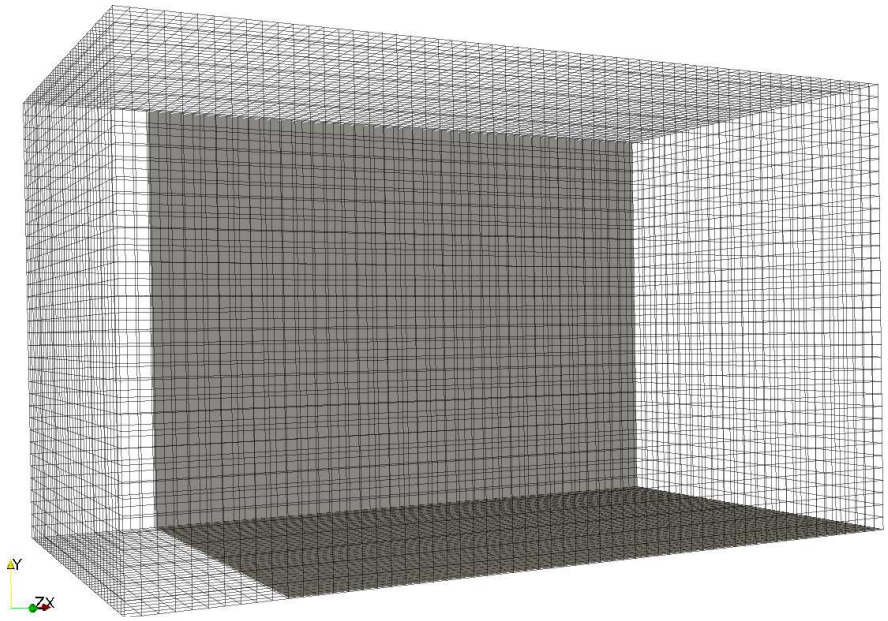

Figure 3.8: Image of the mesh created in OpenFOAM for the supersonic corner flow benchmark simulation.

3.3.1 Approach to Steady State

As the system is initialised with uniform velocity, temperature and density throughout the domain, it is necessary to allow a transient period until the steady state solution is obtained. In order to decide when a simulation has reached steady state, we monitor the number of particles in the system, along with the energy. Figure 3.9 shows the number of particles and average energy in the system changing as the simulation proceeds through a transient period before reaching its steady state, as indicated on Figure 3.9(a). Sampling to recover macroscopic properties is not employed during the transient period; it is only activated once the system has reached steady state.

3.3.2 Results and Conclusions

Once the system reaches steady state, the time averaging is turned on and a total of 100,000 sampling time steps are performed. The simulation was run in parallel on 4 cores of a desktop PC equipped with an Intel i7 processor and the total run time was 30.7 hours.

Figure 3.10 shows various properties measured at the plate surfaces, and the agreement with Birds's DSMC3 code result is excellent. Figures 3.11 and 3.12 show contours

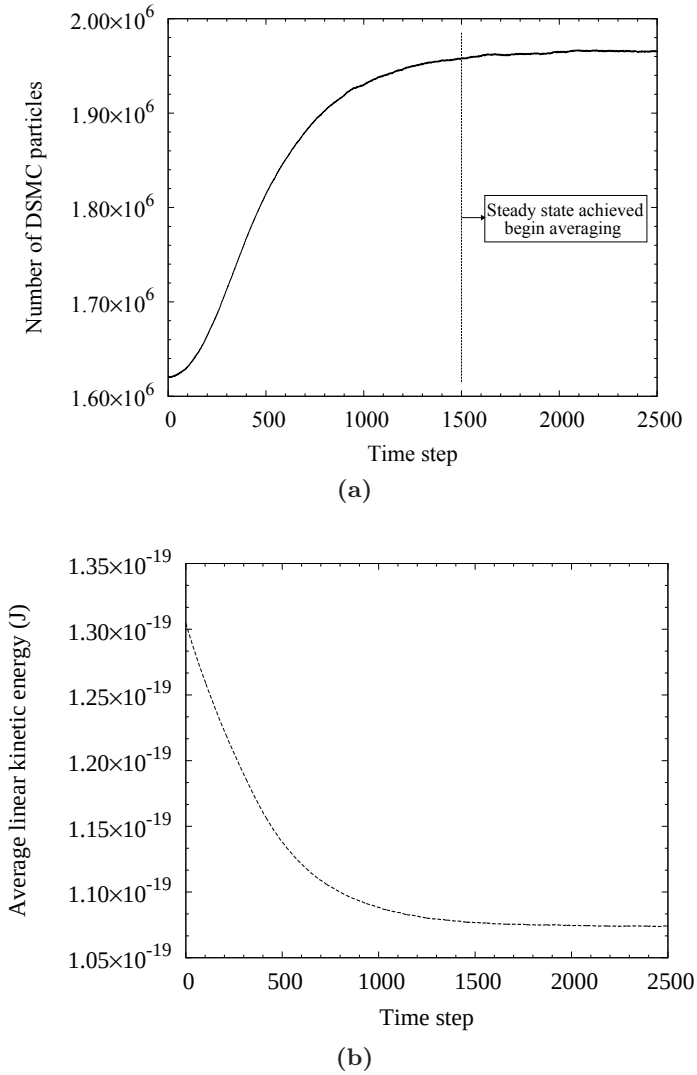

Figure 3.9: Evolution of (a) number of DSMC particles, and (b) average linear kinetic energy in the supersonic corner flow case.

of Mach number and normalised density at four different cross-sections along the domain in the streamwise direction. The results from *dsmcFoam* are compared with those from Bird's DSMC3 code and good qualitative agreement can be seen.

3.4 Flat-Nosed Cylinder

The third benchmark case involves supersonic flow incident on the flat face of a cylinder. This case is presented as an example of axi-symmetric flows on page 374 of Bird's book [21]. *dsmcFoam* does not have axi-symmetric capability, so we perform this

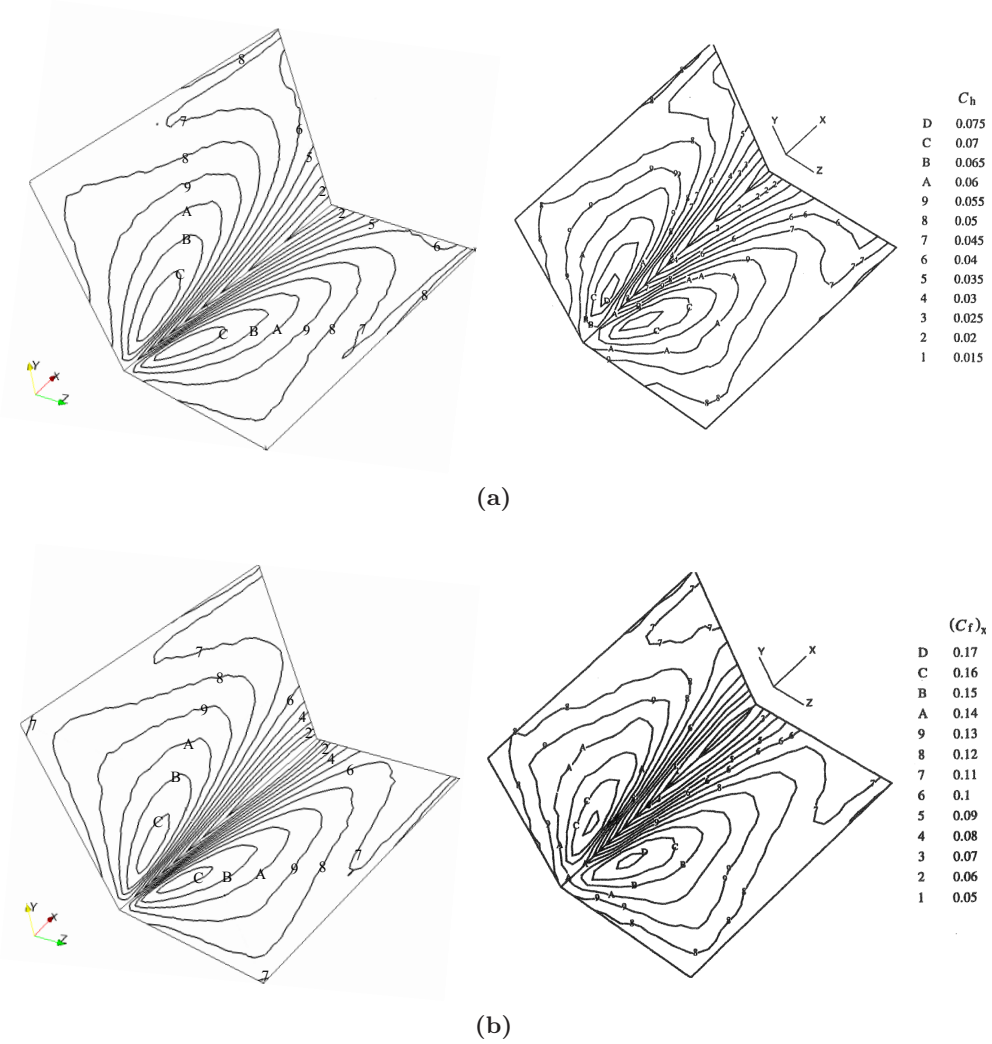

Figure 3.10: Comparison of contours of (a) constant heat transfer coefficient C_h, and (b) constant streamwise skin friction coefficient $(C_f)_x$ at the plate surfaces from *dsmcFoam* (left) and Bird [21] (right).

simulation in three-dimensions, while taking advantage of quarter symmetry.

The radius of the cylinder is 0.01 m and the length simulated is 0.02 m. The working gas is argon with a freestream temperature T_∞, number density n_∞, and Mach number of 100 K, 1×10^{21} m^{-3}, and 5.37, respectively. The VHS mean free path based on the freestream conditions is 9.48×10^{-4} m, giving a Knudsen number of 0.0474 based on the cylinder's diameter. A reference temperature of 273 K is used and the VHS properties for argon outlined in §3.3 are used.

The cylinder is modelled as a fully diffuse surface at a constant temperature of 300 K. 80 × 60 × 60 cells are used to mesh a domain of 0.04 m × 0.03 m × 0.03 m to

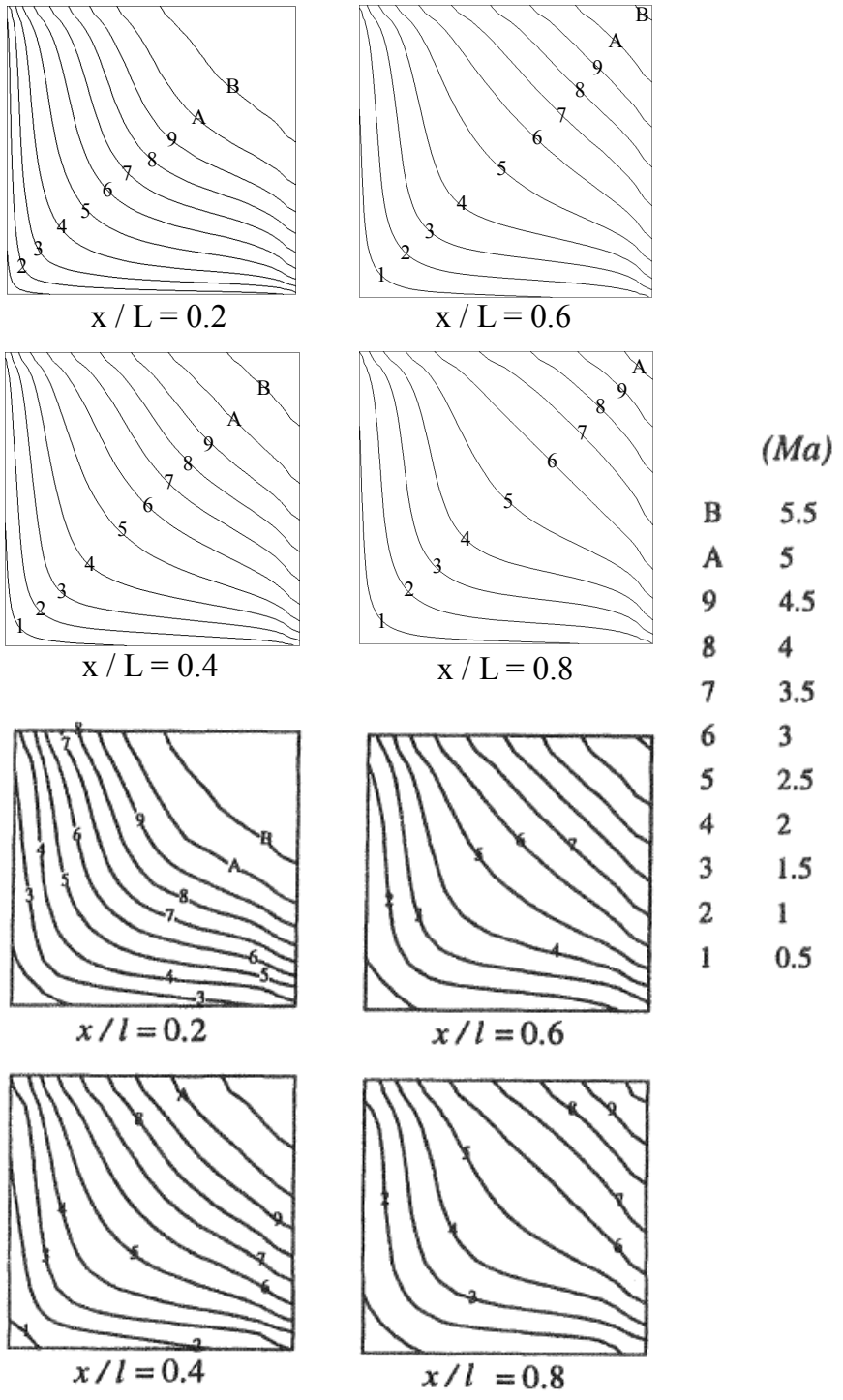

Figure 3.11: Comparison of contours of constant Mach number *Ma* at cross-sections normal to the plates from *dsmcFoam* (top) and Bird [21] (bottom).

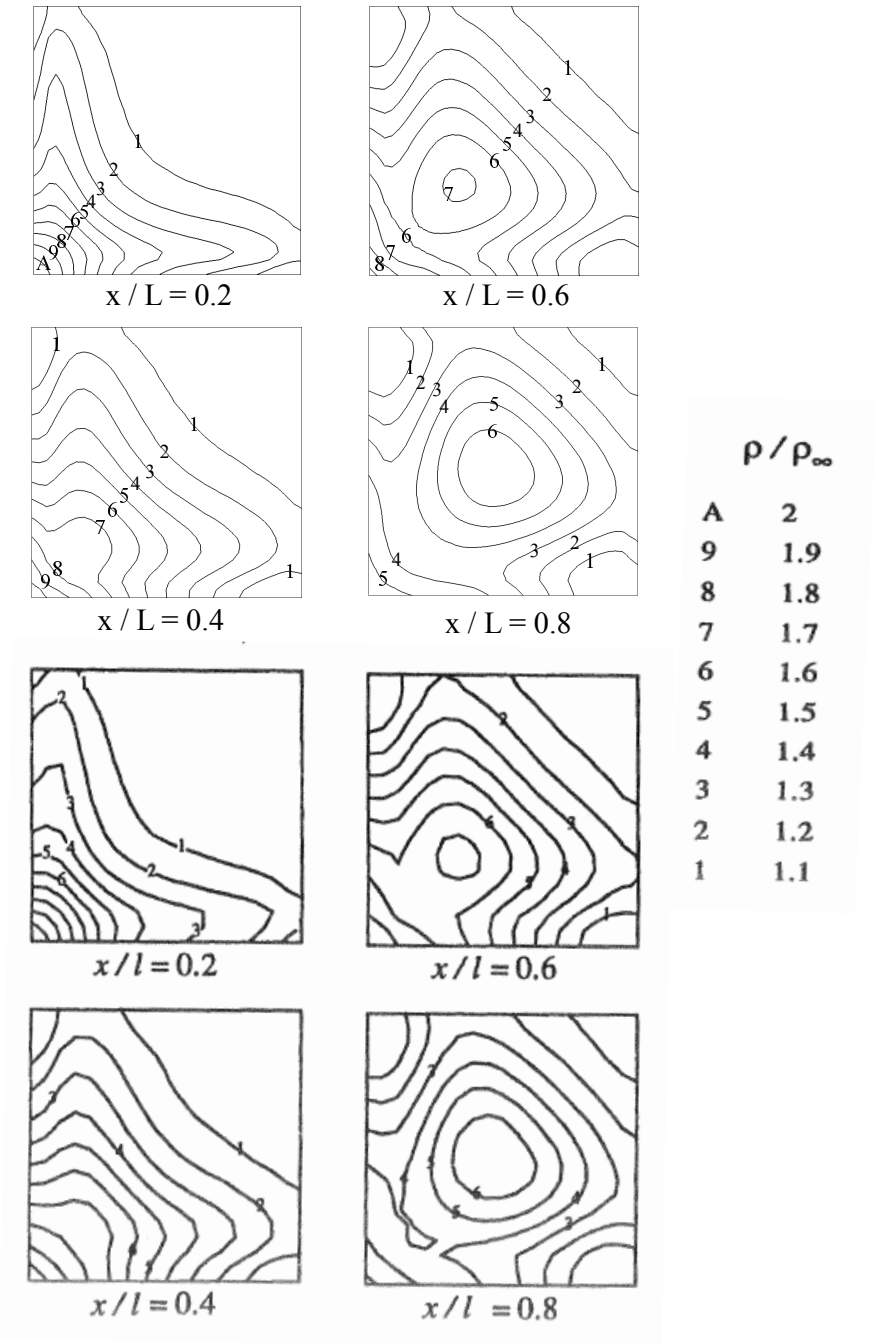

Figure 3.12: Comparison of contours of constant density at cross-sections normal to the plates from *dsmcFoam* (top) and Bird [21] (bottom).

remain consistent with the mesh used by Bird. The cell size is therefore around one half of the mean free path and we use eight sub-cells when performing collisions. A time step of 8×10^{-8} s is chosen; this is significantly smaller than the freestream mean collision time of 4.65×10^{-6} s and small enough to ensure particles will spend multiple time steps in a single cell.

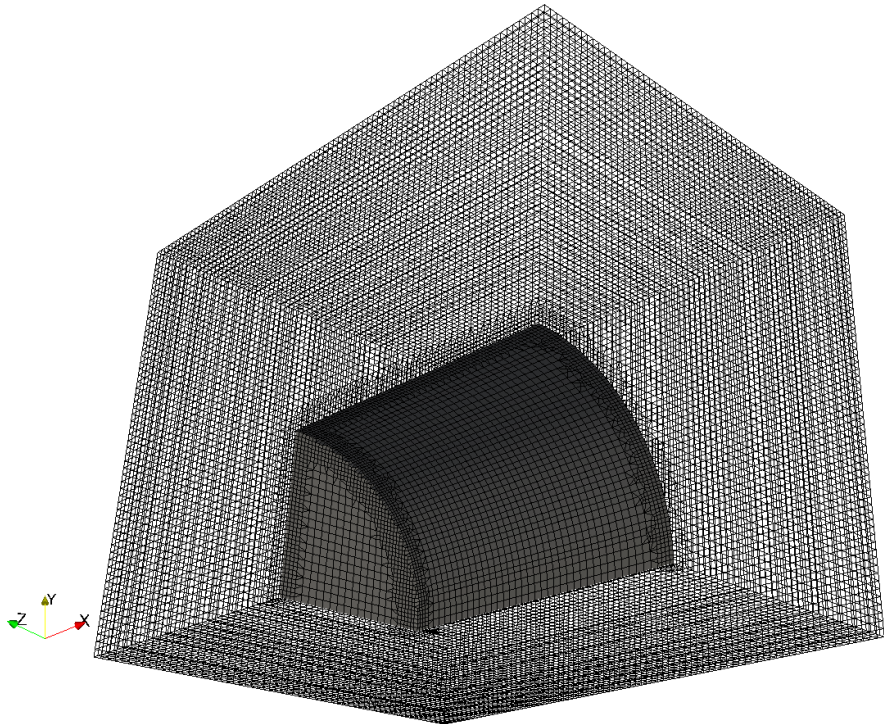

Figure 3.13: Image of the mesh created in OpenFOAM for the quarter-symmetry flat-nosed cylinder flow benchmark simulation.

3.4.1 Creating the Mesh

OpenFOAM's *snappyHexMesh* utility is used to help create the mesh for this benchmark case. A simple cuboid mesh with $80 \times 60 \times 60$ cells is first created with the *blockMesh* utility and then a computer aided design (CAD) geometry of a quarter cylinder is created. *snappyHexMesh* modifies a simple structured mesh and 'snaps' it to take on the shape of any CAD geometry the user desires, resulting in an unstructured mesh. The final mesh used in this case is shown in Figure 3.13, where the solid grey surfaces are the walls of the cylinder.

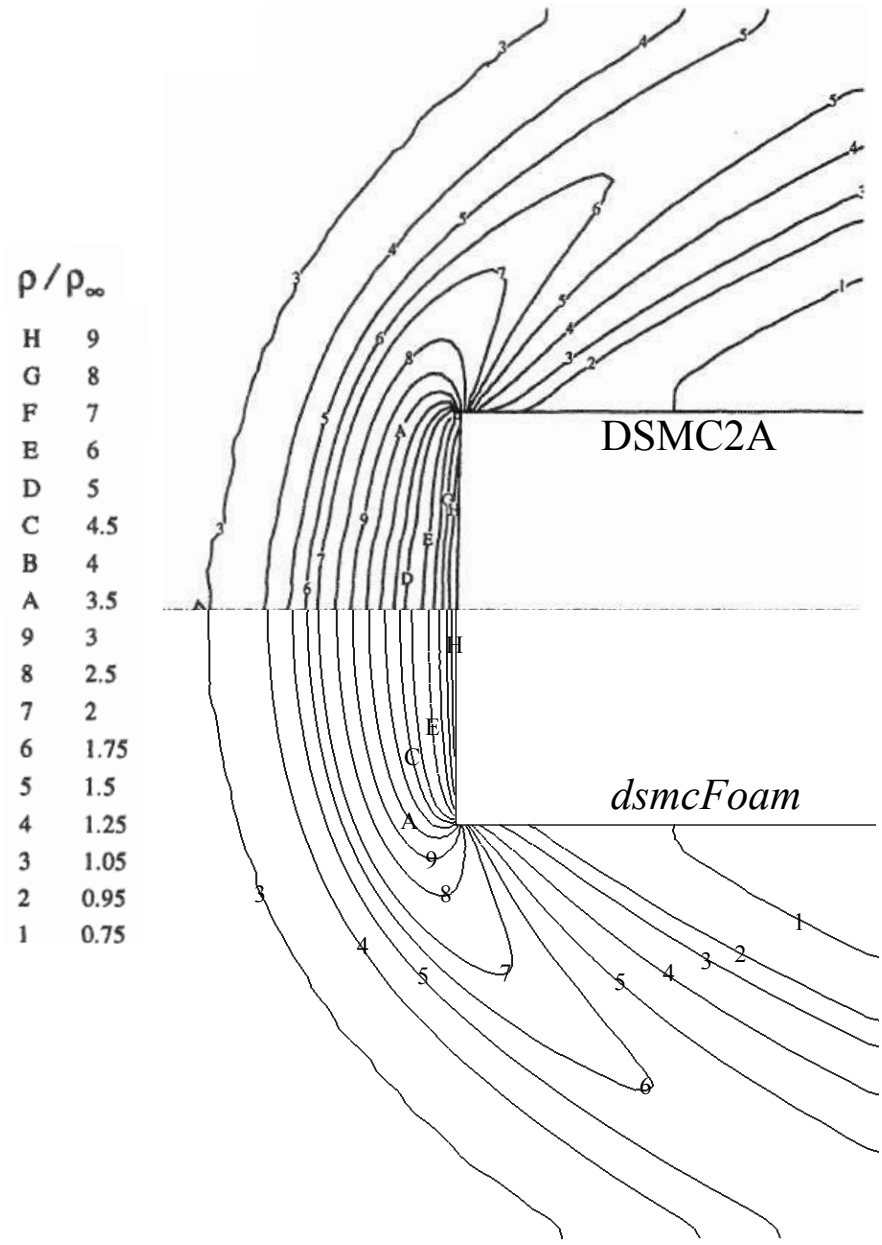

Figure 3.14: Comparison of contours of constant normalised density calculated by DSMC2A (top) and *dsmcFoam* (bottom).

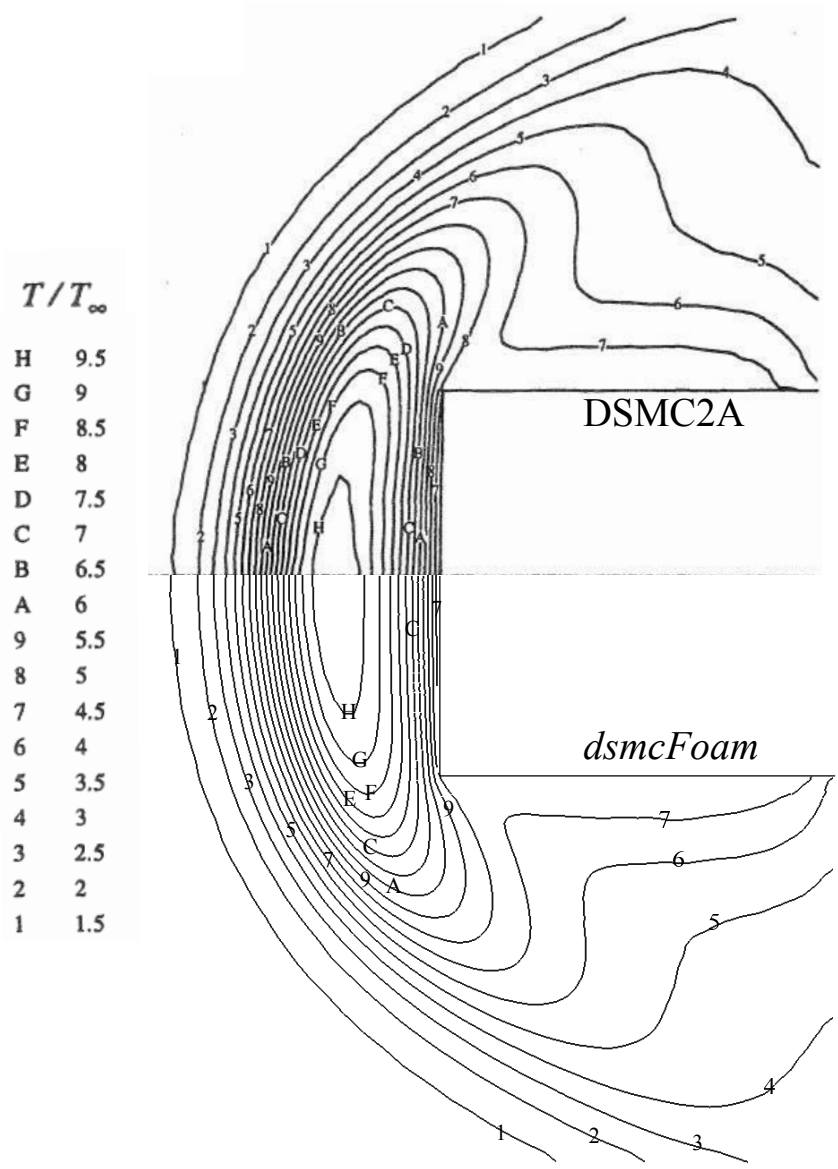

Figure 3.15: Comparison of contours of constant normalised temperature calculated by DSMC2A (top) and *dsmcFoam* (bottom).

3.4.2 Results

The simulation is initialised uniformly with around 25 DSMC particles per cell at the freestream macroscopic conditions. The case was solved in parallel on 8 cores of a desktop PC with an i7 processor. After a transient period of 5000 time steps, there were around 7 million DSMC particles in the system. Time averaging was turned on and a total of 50,000 samples were collected. The total runtime was roughly 52 hours. No attempt to maximise the efficiency of the parallel simulation has been made here, and a greater speed up could likely be achieved by careful consideration of load balancing and mesh decomposition.

Figure 3.14 compares contours of constant density at the symmetry plane from *dsmcFoam* with the axi-symmetric result of Bird, obtained using the DSMC2A code. Figure 3.15 is a comparison of the contours of normalised density. Excellent agreement is observed for both properties, further validating the *dsmcFoam* code.

3.5 Hypersonic Cylinder Flow

The cylinder in hypersonic cross-flow is a test case from Lofthouse's PhD thesis [54] that was used to benchmark several DSMC codes at the DSMC'07 workshop [30]. The case considers Mach 10 flow of argon gas over a cylinder. As discussed in §1.3.1, in rarefied regimes the gas may not be in equilibrium at a surface, and velocity slip and temperature jump may be observed. We use this case to benchmark the velocity slip and temperature measurements from *dsmcFoam* against MONACO [49]. Slip U_{slip} and jump T_{jump} are measured at a surface according to the relations given by Lofthouse [54]:

$$U_{slip} = \frac{\sum \left[\left(m/|c_n| \right) c_t \right]}{\sum \left(m/|c_n| \right)} - U_s, \tag{3.5}$$

$$T_{jump} = \frac{1}{3R} \frac{\sum \left[\left(m/|c_n| \right) \left(\|\mathbf{c}\| \right) \right] - \sum \left(m/|c_n| \right) U_{slip}^2}{\sum \left(1/|c_n| \right)} - T_s, \tag{3.6}$$

where U_s and T_s are the surface velocity and temperature, c_n and c_t are the velocity components of the DSMC particles normal and tangential to the surface, respectively, and R is the specific gas constant. Particle properties must be measured before and after they interact with the surface.

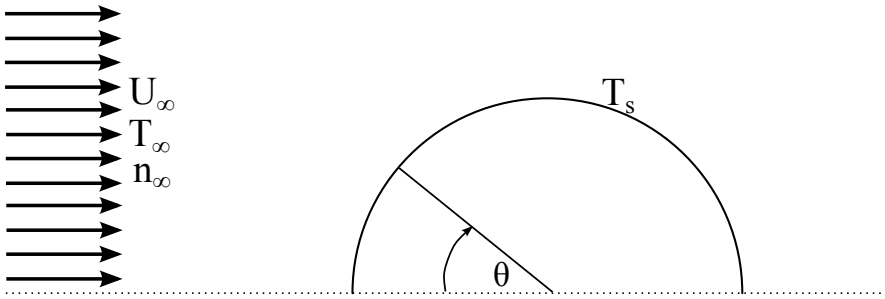

Figure 3.16: Schematic of the hypersonic cross-flow over a cylinder case. The case is symmetrical around the cylinder centre-line.

The cylinder under consideration here has a diameter of 0.3048 m, the freestream number density n_∞ is 1.699 $\times$ 10^{19} m^{-3} and the freestream temperature T_∞ is 200 K, as illustrated in Figure 3.16. The freestream Mach number is 10 and the cylinder surface temperature T_s is constant at 500 K. The VHS collision model is used, and to remain consistent with the work in Reference [54] a reference temperature of 1000 K is used, with the reference diameter d_{ref} being 3.959 $\times$ 10^{-10} m, and a viscosity exponent ω of 0.734. All gas-surface interactions are considered to be fully diffuse. The Knudsen number based on the hard sphere mean free path and the cylinder diameter is 0.25.

3.5.1 Results and Conclusions

A structured mesh with 22,000 cells was used to run the *dsmcFoam* simulation, with each cell significantly smaller than the mean free path. Smaller cells are used near the cylinder surface where the local mean free path will be higher due to the presence of the shockwave. A time step of 6 $\times$ 10^{-7} s was chosen, which is small enough to ensure particles spend multiple time steps in a single cell, and is also much smaller than the freestream mean collision time of 2.64 $\times$ 10^{-4} s. Steady state is reached after 10,000 time steps, with 5.6 million DSMC particles in the system, and 100,000 samples are taken to produce the results. The simulation was performed in parallel on 16 cores of the high performance computer (HPC) in the Faculty of Engineering at the University of Strathclyde and a total run time of 112 hours was needed to perform the 110,000 time steps.

Figure 3.17 shows contours of constant temperature from *dsmcFoam* and compares these with the results of Lofthouse [54, 55] produced using MONACO, and excellent

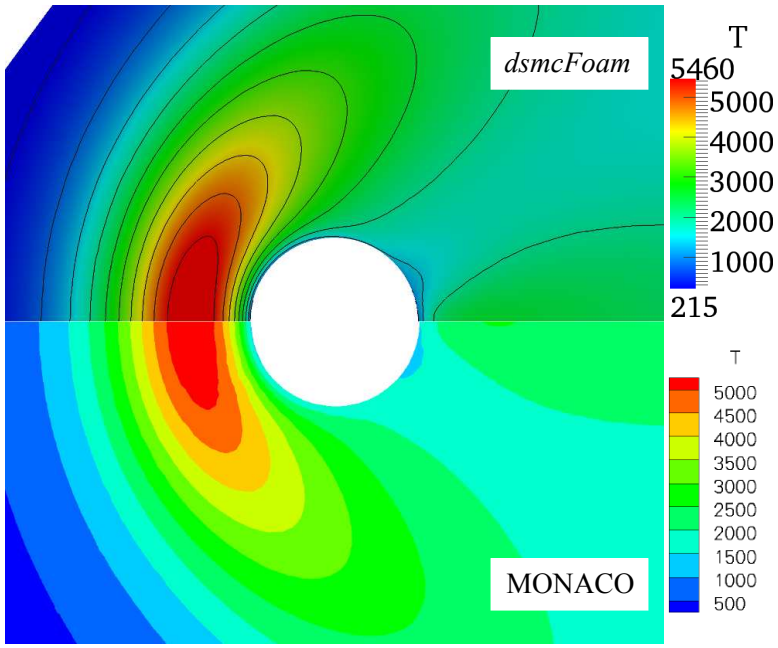

Figure 3.17: Contours of constant temperature. Comparison of results from *dsmcFoam* (top) and MONACO (bottom).

agreement is found.

Figures 3.18(a) and 3.18(b) show the measured slip velocity and temperature jump, respectively, at the cylinder surface calculated by *dsmcFoam* and compared to the same measurements made using MONACO [54]. Reasonable agreement is found for both of these properties, partially validating the implementation of slip and jump measurements. However, *dsmcFoam* does underpredict the temperature jump on the first half of the cylinder surface compared to the more mature MONACO code. This indicates that a future detailed study of the measurement of slip and jump in *dsmcFoam* would be a worthwhile exercise to undertake. There is a near vacuum area in the wake of the cylinder and so it is difficult to reduce the statistical scatter in the wake region of these plots because very few particles interact with the surface. Figure 3.18(c) shows the pressure coefficient c_P at the cylinder surface from MONACO and *dsmcFoam* and excellent agreement is again obtained. The pressure coefficient was calculated as:

$$c_P = \frac{P - P_\infty}{0.5\rho_\infty U_\infty^2}. \tag{3.7}$$

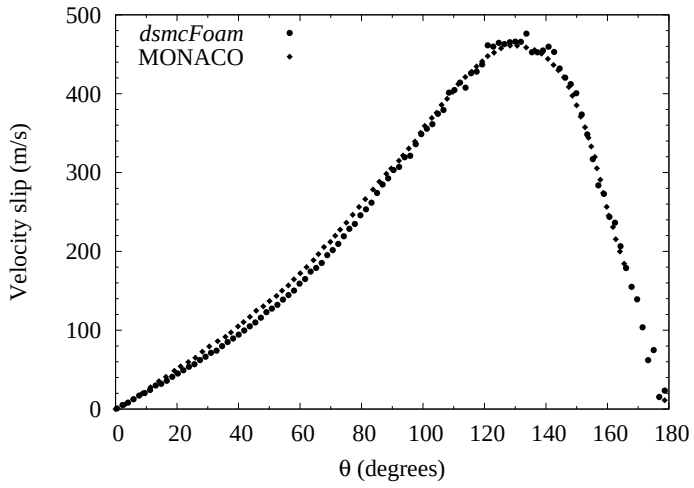

(a)

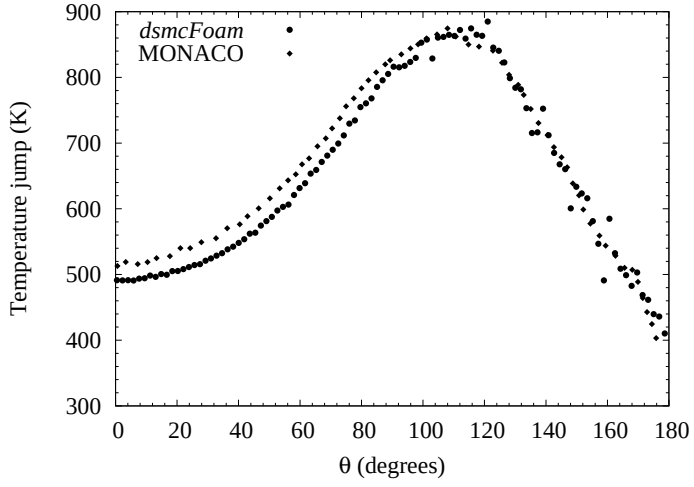

(b)

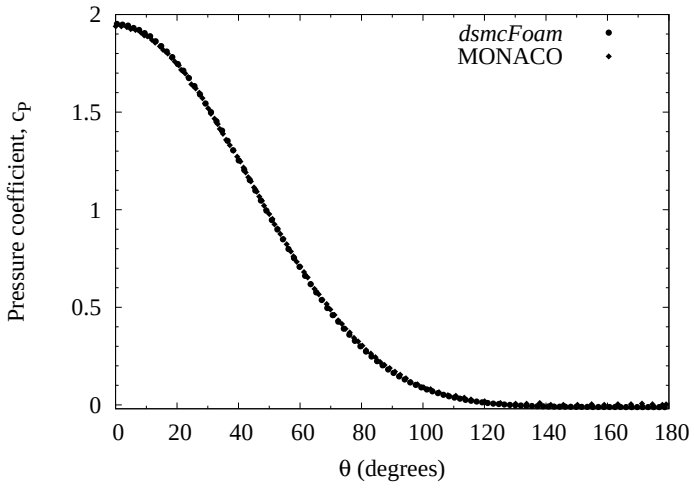

(c)

Figure 3.18: Comparison of measured surface properties around the cylinder from MONACO [52] and *dsmcFoam*: (a) slip velocity, (b) temperature jump, and (c) pressure coefficient.

3.6 Radiometric Forces

So far, we have only benchmarked *dsmcFoam* for supersonic and hypersonic cases. Low speed flows present a different set of problems for the DSMC method, in particular, the low signal-to-noise ratio makes it more difficult to recover macroscopic properties such as temperature and velocity. A significantly larger sample must be used in order to reduce the statistical error to an acceptable level. The benchmark case we chose for these kinds of flows is a non-isothermal vane in a vacuum chamber, as considered by Gimelshein *et al.* [56]. This problem has the advantage of having both experimental results and DSMC results from the SMILE code to compare our *dsmcFoam* results with.

This benchmark case is essentially the classical Crookes radiometer [57]. This is a well known rarefied gas dynamics example and is detailed in this thesis in a later chapter. The main concept of the problem is that a non-isothermally heated vane in a rarefied gas environment has an unbalanced force acting upon it. This phenomenon was first discovered by William Crookes with his radiometer invention, and therefore these kinds of forces are known as radiometric. The experimental results in Reference [56] measure this force over a range of rarefaction and different gas species, and compare to results from the SMILE DSMC code.

The vacuum test chamber dimensions are $0.4 \times 0.4 \times 0.4$ m and the cross-sectional area of the vane is 3.81 cm $\times$ 0.95 cm. Figure 3.19 is a diagram of the vacuum chamber with vane apparatus considered for this benchmark case. The diagram is symmetric around the dashed line at the bottom, h is 3.81 cm, w is 0.95 cm, T_w, T_h and T_c are 300 K, 450 K and 410 K, respectively. The Knudsen number for these cases is based on the variable hard sphere mean free path and the vane height h.

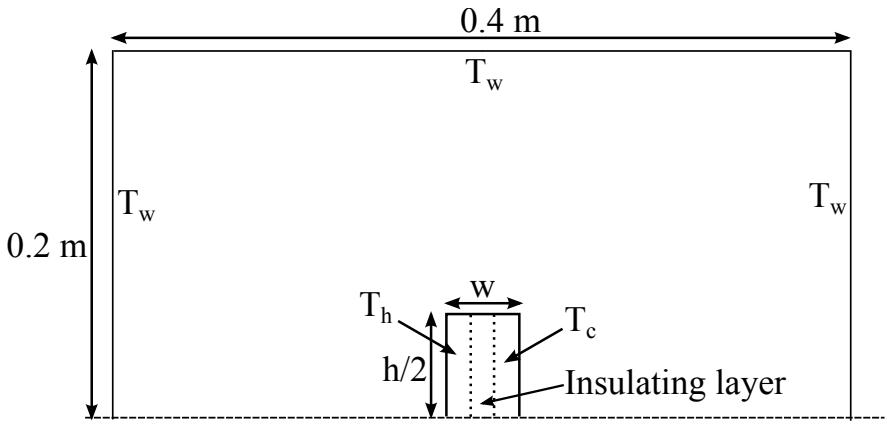

Figure 3.19: Diagram of the vacuum chamber apparatus for radiometric investigations.

3.6.1 Results using Argon gas

The chamber wall temperature T_w is maintained constant at 300 K throughout all of the simulations. Firstly, we consider the vacuum chamber to be filled with argon gas at an initial uniform temperature of 300 K and pressure of 1.2 Pa. The mean free path is 4.6×10^{-3} m and the Knudsen number is 0.12. The numerical cell size is roughly 1.5×10^{-3} m and the time step is 1.5×10^{-6} s, about 10 times smaller than the mean collision time of 1.3×10^{-5} s. The system is initialised with around 40 DSMC simulator particles per cell, giving 6.2 million particles. One half of the vane is maintained constant at 450 K and the other side at 410 K, with an insulating layer simulated between the surfaces at a temperature of 430 K. All gas-surface interactions are considered to be fully diffuse. A reference temperature of 273 K is used, and the VHS parameters for argon are outlined in §3.3.

The system relaxes towards a steady state as the particles interact with the heated vane surfaces and one another. Once the average linear kinetic energy in the system attained a constant value (after 9,000 time steps), averaging was started for a total of 500,000 time steps. The case was run in parallel on 16 cores on the HPC in the Engineering Faculty at the University of Strathclyde and the total run time was 7 days.

Figure 3.20 shows velocity streamlines with contours of constant temperature obtained from *dsmcFoam*, and compares these with results from the SMILE code for the same case [56]. Good qualitative agreement is found: the temperature contours are

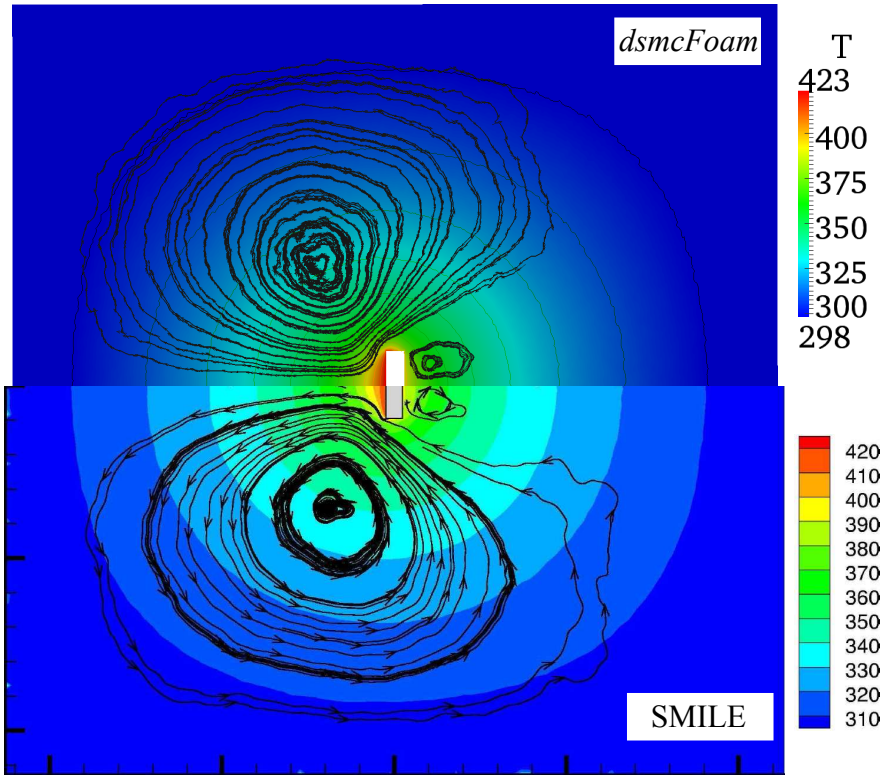

Figure 3.20: Contours of temperature with velocity streamlines for argon gas at $Kn = 0.12$. Comparison of results from SMILE (bottom) and *dsmcFoam* (top).

very similar, and both codes predict a large recirculation region on the hot side of the vane, with a smaller recirculation zone immediately behind the cold side. The level of scatter appears similar in both results, but small differences could be because of the different meshes used, the different post-processing tools, or even because SMILE uses the majorant frequency collision partner selection scheme [43], while *dsmcFoam* uses the no time counter method.

3.6.2 Results using Helium gas

In addition to their DSMC simulations, Gimelshein *et al.* [56] performed experimental measurements of the force induced on the radiometer vane. While showing that *dsmcFoam* is consistent with other DSMC codes is a useful exercise, it is also important to benchmark against experimental results, and we use these force measurements here for that purpose. Gimelshein *et al.* performed their numerical and experimental work for several gas species and found that lighter gases produce larger forces acting on the

radiometer vane. We have therefore chosen to validate *dsmcFoam* against the experimental and numerical results for radiometric forces acting on a heated vane surrounded by helium gas.

The VHS and gas species parameters for helium at a reference temperature of 273 K were used in the *dsmcFoam* simulations. These are: molecular mass $m = 6.65 \times 10^{-27}$ kg, reference diameter $d_{ref} = 2.33 \times 10^{-10}$ m, and viscosity coefficient $\omega = 0.66$. The vacuum chamber and vane dimensions are the same as for the argon case above, and the temperatures of the vane also remain the same. We simulate the system at initial pressures of 6, 3, 2, 1 and 0.4 Pa. The corresponding Knudsen numbers based on the VHS mean free path and vane height range from 0.024 to 0.36.

A mesh of 221,000 cells was used for the 3 Pa and lower pressure cases, with a total of 2.2 million DSMC particles in the systems. Over 1 million samples were taken and the total run time was 183 hours in the 3 Pa case. Run times were slightly shorter in the less dense cases as fewer inter-particle collisions had to be processed. The simulations were run in parallel on 8 cores on the HPC in the Faculty of Engineering at the University of Strathclyde.

This cell size was too large for the 6 Pa case and so a finer mesh was used at this pressure: 22 million DSMC particles were used with a mesh of around 2 million cells, and the case was solved in parallel on 64 cores on the HPC.

Figure 3.21 shows the forces acting on the non-isothermal vane surrounded by helium gas. Good agreement is found with the numerical results from SMILE, with small differences possibly due to the different meshes, potentially different time steps, and the different collision partner selection schemes. The initial increase in the magnitude of the force as the gas becomes more rarefied, and then decrease as the degree of rarefaction is increased further is characteristic of the radiometric force. Experimental data is only available for the lowest pressures; both SMILE and *dsmcFoam* are in excellent agreement with these force measurements.

3.7 Summary

In this chapter we have undertaken some benchmarking of *dscmFoam*, a new open-source direct simulation Monte Carlo code. Results from *dsmcFoam* have been com-

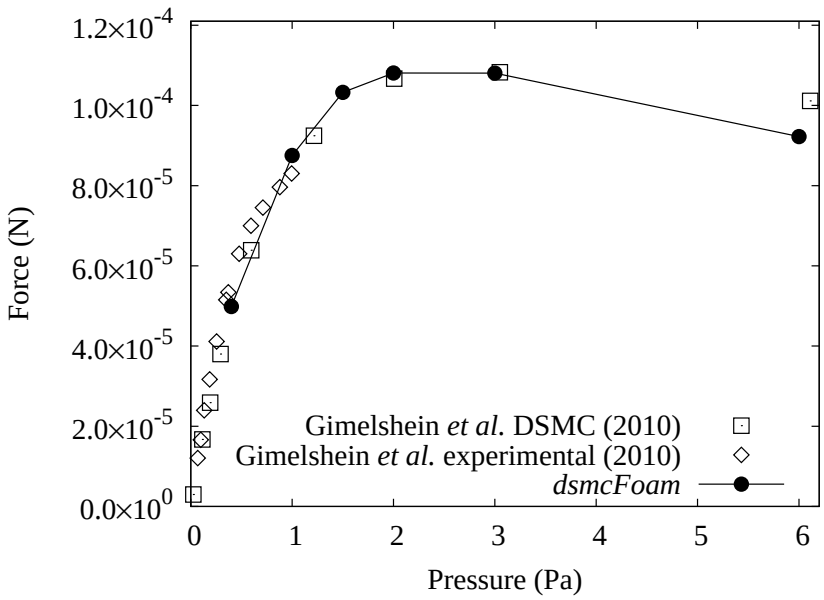

Figure 3.21: Radiometric forces for the helium gas simulations. Comparison of forces from SMILE and *dsmcFoam*, along with forces measured in experiment [56].

pared to analytical solutions, experimental results, and some well established DSMC codes.

Results from *dsmcFoam* for collision rates are in excellent agreement with the kinetic theory analytical solution, indicating that the no-time-counter method is correctly implemented. Scattering angle probability plots show that the *dsmcFoam* diffuse and specular gas-surface interactions are in good agreement with results from the independent MONACO code, and an analytical solution.

We have shown that *dsmcFoam* gives three-dimensional results that are in good qualitative agreement with Bird's DSMC3 and DSMC2A codes, for the supersonic corner flow and flat-nosed cylinder cases, respectively. Two-dimensional hypersonic flow over a cylinder has been compared to the mature MONACO code and good quantitative agreement for slip velocity, temperature jump and pressure coefficient measurements has been demonstrated, along with good qualitative agreement for contours of temperature. Qualitative results for temperature profiles and velocity streamlines surrounding a radiometer vane are in good agreement with the independent SMILE code. Force measurements on a radiometer vane from *dsmcFoam* are in excellent agreement with both experimental measurements and results from SMILE.

Results from this chapter, along with additional cases, are included in a published journal article that benchmarks *dsmcFoam* [58]. Further benchmark cases, including relaxation to rotational equilibrium using the Larsen-Borgnakke energy exchange model, have been performed by Arlemark *et al.* [59].

Chapter 4

New Developments in *dsmcFoam*

Unless we progress, we regress.

- Dwight D. Eisenhower

Having benchmarked the standard *dsmcFoam* code in the previous chapter, we now discuss some extensions to *dsmcFoam* that have been undertaken. As discussed in Chapter 2, there is some functionality missing from *dsmcFoam* that would increase the applicability of the software. We aim to make a significant improvement in the functionality of *dsmcFoam* through the introduction of a vibrational degree of freedom, a state-of-the art air chemistry model, another gas-surface interaction model, and a macroscopic properties measurement framework.

4.1 Vibrational Energy

The vibrational modes of a gas are only active when the system is sufficiently energised, e.g. by being at high temperature. In low speed, standard temperature MEMS flows it is often perfectly acceptable to ignore the vibrational mode for this reason. However, in hypersonic applications, with strong compressibility effects due to shockwaves, there are likely to be regions where the temperature is high enough to excite the vibrational mode, even if the freestream temperature is low.

If this functionality is missing from a DSMC code, a significant physical feature of the gas is being neglected. Vibrational energy plays an essential role in chemical reactions, and restricts the amount of energy available to the translational and rotational

modes. In addition, it often introduces a new mode of non-equilibrium to a rarefied gas system, as the number of collisions required for vibrational relaxation is significantly higher than for translational or rotational equilibrium.

In DSMC, it is normal to assume that vibrational energy can only take discrete quantum level values, as proposed by Haas *et al.* [60] and Bergemann & Boyd [61]. We consider a serial application of the quantum Larsen-Borgnakke method using the harmonic oscillator model to redistribute vibrational energy before rotational energy exchange is considered. In this model the quantum levels are equally spaced. It is desirable in DSMC to try and avoid the use of macroscopic temperature whenever possible; so here we discuss a model for redistribution of vibrational energy based on collision energy, as opposed to the local macroscopic temperature of the gas [62]. The first step is to define a "quantised collision temperature" T_{coll}, based on the collision energy of a particle pair, as

$$T_{coll} = \frac{i_{max}\Theta_v}{(7/2-\omega)}, \tag{4.1}$$

where

$$i_{max} = \left\lfloor \frac{E_c}{k_B\Theta_v} \right\rfloor. \tag{4.2}$$

$\lfloor \ldots \rfloor$ denotes truncation to the lower integer value, i_{max} is the maximum quantum level available to the molecule, Θ_v is the characteristic vibrational temperature (essentially the energy between quantum levels), and E_c is the sum of the relative translational energy of the collision pair and the pre-collision vibrational energy of the molecule under consideration, i.e.

$$E_c = \varepsilon_{tr_{ij}} + \varepsilon_{v_i}. \tag{4.3}$$

The vibrational collision number Z_v can then be calculated as [62]

$$Z_v = \left(\frac{\Theta_d}{T_{coll}}\right)^{\omega} \left[Z_{ref} \left(\frac{\Theta_d}{T_{z_{ref}}}\right)^{-\omega} \right]^{\left[\left(\frac{\Theta_d}{T_{coll}}\right)^{\frac{1}{3}}-1\right] / \left[\left(\frac{\Theta_d}{T_{z_{ref}}}\right)^{\frac{1}{3}}-1\right]}, \tag{4.4}$$

where Θ_d is the characteristic dissociation temperature, and Z_{ref} is the vibrational collision number at a reference temperature $T_{z_{ref}}$ that is usually taken to be the char-

acteristic vibrational temperature Θ_v, such that [63]

$$Z_{ref} = \left(\frac{C_1}{T^{\omega}_{z_{ref}}}\right) \exp\left(C_2 T_{z_{ref}}^{-\frac{1}{3}}\right), \tag{4.5}$$

where C_1 and C_2 are constants from the Millikan & White data and can be found in Appendix A of Ref. [21], and $T_{z_{ref}}$ is set as Θ_v.

Once a vibrational collision number has been calculated, the particle is tested for vibrational energy exchange and is accepted if

$$\frac{1}{Z_v} > R_f. \tag{4.6}$$

A post-collision vibrational quantum level i^* is chosen uniformly between 0 and the maximum possible level i_{max}, and the acceptance-rejection method is used to select a value of i^* from the probability ratio

$$\frac{P}{P_{max}} = \left(1 - \frac{i^* k_B \Theta_v}{E_c}\right)^{3/2-\omega_{ij}}, \tag{4.7}$$

where ω_{ij} is the average viscosity exponent of the collision pair i and j. The relative translational energy of the pair is reduced accordingly and the particle is then considered for rotational relaxation as described in §2.1.2.

When particles are initialised using *dsmcInitialise*, introduced at a freestream boundary, or reflected at a diffuse surface, they must be assigned a vibrational energy. First, a quantum level is chosen by analogy to how rotational energy is chosen for a diatomic molecule, i.e.

$$i = \left\lfloor \frac{-\ln(R_f)\, T_v}{\Theta_v} \right\rfloor, \tag{4.8}$$

where T_v is the vibrational temperature, and then the vibrational energy of the particle is assigned from the relation

$$\varepsilon_v = i k_B \Theta_v. \tag{4.9}$$

4.1.1 Vibrational Temperature

The measurement of vibrational temperature is slightly more complicated than that of the translational and rotational temperatures discussed in Chapter 1, in that it includes

a summation over all species in the gas:

$$T_v = \sum_{m=1}^{n} \left(\zeta_{v,m} T_{v,m}\right) / \sum_{m=1}^{n} \left(\zeta_{v,m}\right), \tag{4.10}$$

where n is the number of species in the gas, and $T_{v,m}$ is the vibrational temperature of species m, calculated as

$$T_{v,m} = \frac{\Theta_{v,m}}{\ln\left(1 + 1/\overline{i}_m\right)}, \tag{4.11}$$

where $\overline{i}_m$ is the average quantum level of particles of species m in the gas. The effective number of vibrational degrees of freedom in species m, $\zeta_{v,m}$, is given as

$$\zeta_{v,m} = \frac{2\Theta_{v,m}/T_{v,m}}{\exp\left(\Theta_{v,m}/T_{v,m}\right) - 1}. \tag{4.12}$$

The overall temperature, including the vibrational mode is then

$$T_{ov} = \frac{3T_{tr} + \overline{\zeta}_{rot} T_{rot} + \overline{\zeta}_v T_v}{3 + \overline{\zeta}_{rot} + \overline{\zeta}_v}, \tag{4.13}$$

where T_{rot} is found from Equation (1.23), $\overline{\zeta}_{rot}$ is the average number of rotational degrees of freedom, and T_v is from Equation (4.10). The average vibrational degrees of freedom $\overline{\zeta}_v$ is over all species and is given by

$$\overline{\zeta}_v = \frac{\sum_{m=1}^{n} \zeta_{v,m}}{n}. \tag{4.14}$$

4.1.2 *dsmcFoam* Implementation

We have implemented vibrational energy into the *dsmcFoam* solver, using a quantum approach and the harmonic oscillator model. Energy is exchanged using the serial application of the Larsen-Borgnakke method, as described above. In order to check that the model is correctly implemented, we perform a series of adiabatic box test cases with a fictitious gas, and compare results to analytical solutions for two different vibrational energy properties.

A single cubic cell with all eight surfaces set as specularly reflecting walls is filled with 1 million DSMC particles, with the system initially in equilibrium. The char-

acteristic vibrational temperature Θ_v of the gas under consideration is 2000 K. The system is set at a temperature of 5000 K and the relative probability P_{rel} distribution of vibrational quantum levels is measured for a total of 1000 time steps, and the result is plotted in Figure 4.1(a) and compared to the analytical Boltzmann distribution:

$$P_{rel}\left(i\right) = \exp\left(\frac{-i\Theta_v}{T_v}\right). \tag{4.15}$$

Excellent agreement is found between our *dsmcFoam* data and the analytical solution. There is some statistical scatter towards the higher vibrational levels, but this is expected as the particles are unlikely to occupy such high quantum states at a temperature of 5000 K. The second test involves measuring the effective number of vibrational degrees of freedom over a range of temperatures and comparing to the analytical solution given in Equation (4.12). The results are shown in Figure 4.1(b) and excellent agreement is found, with the analytical and numerical results all being within 0.7% of one another. These simulations also confirm that the systems remain in equilibrium as we would expect for an adiabatic box with no flow gradients.

In order to test relaxation to equilibrium when vibrational energy is included, a test case from Bird's 2007 DSMC workshop notes [30] is chosen. This is an adiabatic box filled with nitrogen, where the translational and rotational temperatures are initially 20,000 K and there is no energy in the vibrational mode. The reference vibrational collision number Z_{ref} is 19.8 at a reference temperature of 20,000 K. The *dsmcFoam* simulation was performed using the VHS collision model with the properties for a reference temperature $T_{ref} = 273$ K being used, i.e. $m = 46.5 \times 10^{-27}$ kg, $\omega = 0.74$, and $d_{ref} = 4.17 \times 10^{-10}$ m.

The cell is filled with 1.2 million DSMC particles and as the particles begin to collide, energy is transferred to the vibrational mode, with equipartition achieved at a temperature of around 14,720 K after a relaxation period, as shown in Figure 4.2. The 'collision number' for the abscissa has been calculated as the product of the instantaneous collision rate from the simulation and the physical time that has elapsed. The *dsmcFoam* results agree well with those of Bird's DS2V code [30]. The rotational temperature follows the translational temperature closely, and the vibrational temperature takes a longer time to come in to equilibrium. The relaxation rates of all temperatures

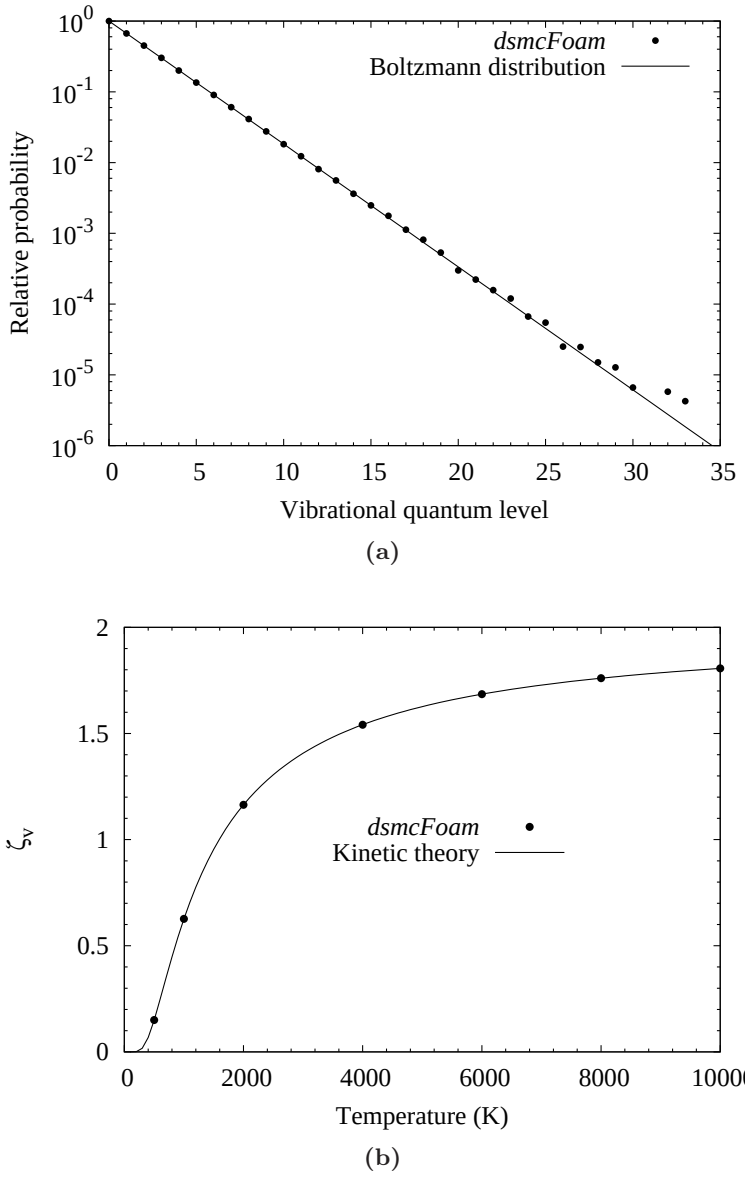

Figure 4.1: Validation plots for the vibrational energy model: (a) distribution function of vibrational quantum levels at 5000 K from *dsmcFoam* compared to the result from Equation (4.15), and (b) number of effective vibrational degrees of freedom from *dsmcFoam* compared with the solution from Equation (4.12).

and the final equilibrium temperature are all in good agreement with Bird's results.

4.2 Quantum-Kinetic Chemical Reactions

Until recently, chemically reacting gas flows in DSMC have relied upon reaction rate coefficients that are derived from equilibrium theory and are functions of macroscopic

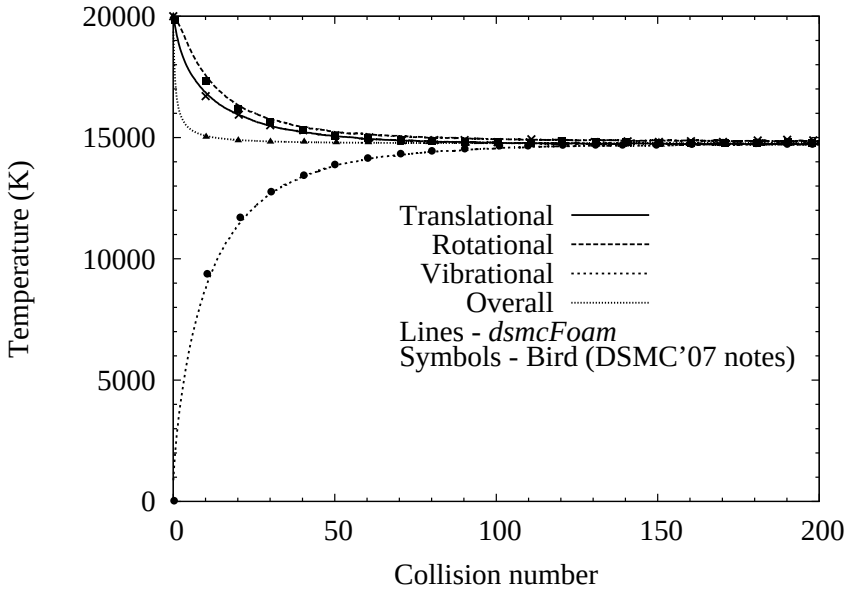

Figure 4.2: Vibrational relaxation of oxygen gas.

temperature. This is undesirable from two points of view: in a microscopic model, it is better to avoid applying macroscopic properties at the molecular level, and the rates may not be valid for reactions in gases with distribution functions that are not of the equilibrium form. This method for treating chemical reactions was introduced by Bird in 1979 and is know as the "total collision energy" (TCE) model [50]. Despite these potential problems, this chemical reaction model is well-developed and is used in the MONACO code [64].

Bird has recently proposed a chemical reaction model that is founded on the quantum Larsen-Borgnakke (L-B) method described in §4.1, has no dependence on macroscopic data, and does not require that the gas be in a state near thermodynamic equilibrium. This is termed the "quantum-kinetic" (QK) model and has been developed over the past five years [62, 65, 66].

In this thesis, we will consider dissociation and exchange reactions with the aim of implementing a five species (oxygen O_2, nitrogen N_2, nitric oxide NO, atomic oxygen O, and atomic nitrogen N) air chemistry model that can eventually be applied to hypersonic DSMC simulations using *dsmcFoam*. These chemical reactions play an important role in the physics of gaseous flow around, for example, a spacecraft during re-entry, and so it is important that a DSMC code have these implemented.

4.2.1 Dissociation Reactions

The condition for a dissociation reaction in the QK model is simple: if the energy in the collision is high enough to allow dissociation to occur, it will always occur. The reaction being considered is $AB + C \rightarrow A + B + C$, where AB is a molecule considered for dissociation, C is the reactant partner and can be either a molecule or an atom, and A and B are the atom products of the dissociation.

Considering the serial application of the quantum L-B model, the collision energy E_c of a particle pair $(AB + C)$ is the sum of the relative translational energy and the pre-collision vibrational energy of the particle currently being considered, see Equation (4.3). The maximum vibrational level that can be selected i_{max} is given by Equation (4.2). If i_{max} is beyond the dissociation limit, i.e.

$$i_{max} > \frac{\Theta_d}{\Theta_v}, \tag{4.16}$$

then the molecule AB must be dissociated before any vibrational or rotational relaxation can be considered.

An advantage of the QK model is that although the DSMC implementation does not require the gas to be in equilibrium, if it is assumed that it is, analytical solutions for the reaction rates can be derived. For a VHS gas in equilibrium, the rate coefficient $k_f(T)$ for the dissociation of a molecule AB with a molecule or atom C is

$$k_f(T) = R_{coll}^{AB,C} \Upsilon (i_{max})^{AB,C}, \tag{4.17}$$

where $R_{coll}^{AB,C}$ is the collision rate between species AB and C divided by the number density product. For an equilibrium VHS gas, this is

$$R_{coll}^{AB,C} = \frac{2\pi^{1/2}}{\nu} \left(r_{ref}^{AB} + r_{ref}^{C}\right)^2 \left(\frac{T}{T_{ref}}\right)^{1-\omega^{AB,C}} \left(\frac{2k_B T_{ref}}{m_r^{AB,C}}\right)^{1/2}, \tag{4.18}$$

where r_{ref}, T_{ref} and ω are the standard VHS properties of the relevant gas species, m_r is the reduced mass of the collision pair, T is the macroscopic temperature of the gas, ν is a symmetry factor, which is set to 2 if the molecules in the collision are the same and 1 for unlike molecules. The $\Upsilon\left(i_{max}\right)^{AB,C}$ parameter defines the fraction of

collisions that will have sufficient energy to dissociate. Taking i as the pre-collisional vibrational state of the dissociating molecule, the result is

$$\Upsilon\left(i_{max}\right)^{AB,C} = \sum_{i=0}^{i_{max}-1} \frac{\left\{Q\left[\frac{5}{2}-\omega^{AB,C}, \left(\frac{(i_{max}-i)\Theta_v^{AB}}{T}\right)\right]\exp\left(\frac{-i\Theta_v^{AB}}{T}\right)\right\}}{z_v\left(T\right)^{AB}}, \tag{4.19}$$

where $Q\left(a,x\right) = \Gamma\left(a,x\right)/\Gamma\left(a\right)$ is a form of the incomplete Gamma function and $z_v\left(T\right)^{AB} = 1/\left[1-\exp\left(-\Theta_v/T\right)\right]$ is the vibrational partition function [66].

4.2.2 Dissociation in *dsmcFoam*

We have implemented the measurement of dissociation reaction rates in *dsmcFoam* for the following nine molecule-molecule dissociations, which we term "Type I" dissociations:

$$O_2 + O_2 \rightarrow O + O + O_2, \tag{4.20}$$

$$N_2 + N_2 \rightarrow N + N + N_2, \tag{4.21}$$

$$NO + NO \rightarrow N + O + NO, \tag{4.22}$$

$$O_2 + N_2 \rightarrow O + O + N_2, \tag{4.23}$$

$$N_2 + O_2 \rightarrow N + N + O_2, \tag{4.24}$$

$$O_2 + NO \rightarrow O + O + NO, \tag{4.25}$$

$$N_2 + NO \rightarrow N + N + NO, \tag{4.26}$$

$$NO + O_2 \rightarrow N + O + O_2, \tag{4.27}$$

$$NO + N_2 \rightarrow N + O + N_2, \tag{4.28}$$

and these six molecule-atom dissociations, or "Type II" dissociations

$$O_2 + O \rightarrow O + O + O, \tag{4.29}$$

$$O_2 + N \rightarrow O + O + N, \tag{4.30}$$

$$N_2 + O \rightarrow N + N + O, \tag{4.31}$$

$$N_2 + N \rightarrow N + N + N, \tag{4.32}$$

$$NO + O \rightarrow N + O + O, \tag{4.33}$$

$$NO + N \rightarrow N + O + N. \tag{4.34}$$

If a DSMC particle meets the criterion for dissociation to occur (Equation (4.16)), we simply update a counter within our DSMC simulation. Particle splitting and the associated conservation of mass, momentum and energy is not considered in the current work. This allows the reaction rates to be calculated at a constant temperature for a gas in equilibrium and compared to the analytical QK solution of Equation (4.17). In his 2011 QK paper [66], Bird does not present any DSMC simulation data: it is solely analytical work with a description of the DSMC implementations of each reaction. Gallis *et al.* [3] have presented some DSMC simulation data, however this work was performed using a DSMC implementation for exchange reactions that has since been superseded.

Adiabatic box simulations are performed to measure the dissociation rate coefficients for each reaction. A box with six specularly reflective surfaces is used for this purpose. Our DSMC simulations consider each of the five species to have a number density of 1×10^{19} m^{-3}, and the number of real molecules/atoms that each DSMC particle represents F_N is chosen such that there will be 1 million DSMC particles of each species in the box. The simulations were run until the number of "reactions" was of the order 10^5 - 10^6 for most cases, but at low temperatures it was necessary to accept a lower sample size due to small reaction rates. The particles were not allowed to move, but they were allowed to exchange energy in order to increase the sample size.

For each case, we show the relative difference between the analytical and the simulated QK reaction rates. The difference is calculated as

$$\text{Relative difference} = 100\left(1 - \frac{k_{f_{simulated}}}{k_{f_{analytical}}}\right), \tag{4.35}$$

and we also include the TCE rate for each reaction, which take the form

$$k_f(T) = C_3 T^{C_4} \exp(-C_5/T) \tag{4.36}$$

where C_3, C_4 and C_5 are reaction specific constants, the values of which can be found in Reference [64] and are presented in Table 4.1.

Reaction	C_3	C_4	C_5
$O_2 + O_2 \rightarrow O + O + O_2$	3.321×10^{-9}	-1.5	59400
$N_2 + N_2 \rightarrow N + N + N_2$	1.162×10^{-8}	-1.6	113200
$O_2 + O \rightarrow O + O + O$	1.660×10^{-8}	-1.5	59400
$N_2 + N \rightarrow N + N + N$	4.980×10^{-8}	-1.6	113200

Table 4.1: TCE dissociation reaction rate parameters [64] for the plotted reactions.

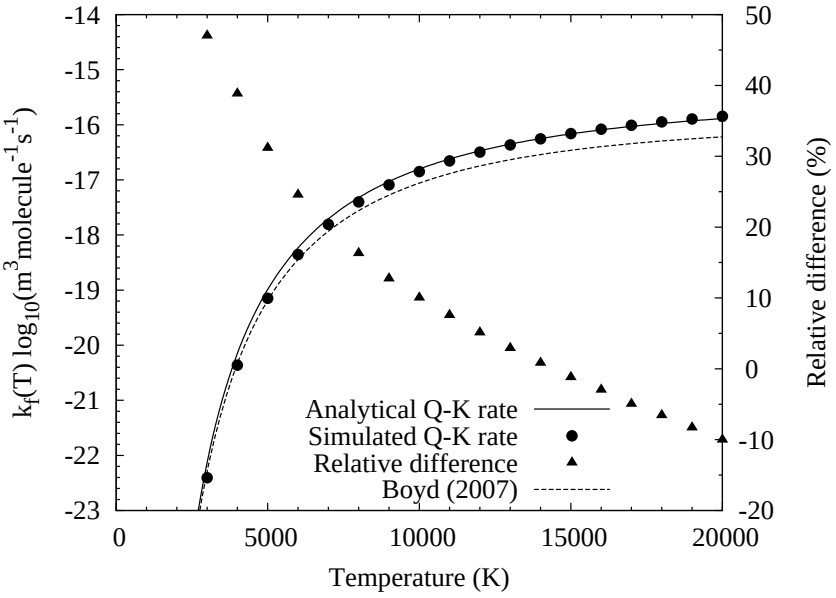

Figure 4.3: Dissociation rate coefficients for Type I dissociation, $O_2 + O_2 \rightarrow O + O + O_2$.

Figure 4.3 shows the Type I dissociation reaction rate coefficient for the dissociation of oxygen in collisions with another oxygen molecule. Good agreement is found between the simulated and analytical QK rates, with the maximum percentage relative error being around 50% at 3000 K. The degree of uncertainty in the rate coefficients for high temperature air is accepted to be around a factor of five, so in this context, a maximum relative error of much less than an order of magnitude is acceptable, especially at lower temperatures where chemical reactions are not as important. The TCE analytical solution from Boyd [64] is one of the currently accepted rates. Our *dsmcFoam* implementation of oxygen dissociation is in reasonably good agreement with the TCE

solution, only returning slightly higher rate coefficients at the highest temperatures considered here.

Figure 4.4 shows the reaction rate coefficients for the Type I dissociation reaction defined in Equation (4.21), i.e. dissociation of a nitrogen molecule in a collision with another nitrogen molecule. The analytical and numerical QK solutions are again in excellent agreement, with a very similar level of relative differences being evident. The relative difference in both Figures 4.3 and 4.4 display the same pattern: highest at low temperatures, crosses through 0%, and eventually obtains a small negative value at the highest temperatures. The agreement with the TCE data of Boyd is acceptable, but is not as close as in the oxygen reaction.

The rate for the Type II dissociation reaction defined in Equation (4.29) is plotted in Figure 4.5, and that for Equation (4.32) in Figure 4.6. Excellent agreement is found between the analytical and simulated QK rates, and good agreement with the accepted TCE rates of Boyd [64] is observed for both reactions.

Although they are not shown in this thesis for conciseness, the remaining dissociation reactions listed previously have all been implemented in *dsmcFoam*, and the simulated rates are all in relative agreement with the analytical QK rates and Boyd's TCE rates.

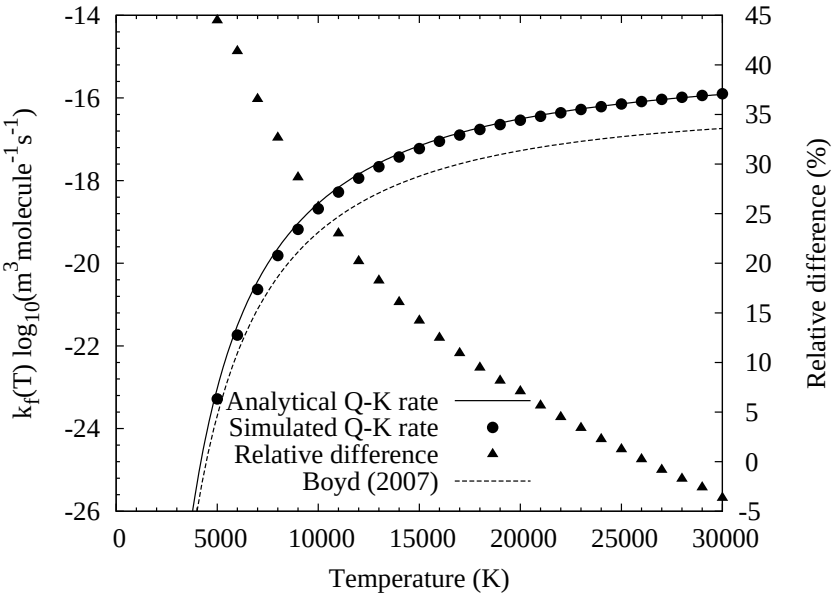

Figure 4.4: Dissociation rate coefficients for Type I dissociation, $N_2 + N_2 \rightarrow N + N + N_2$.

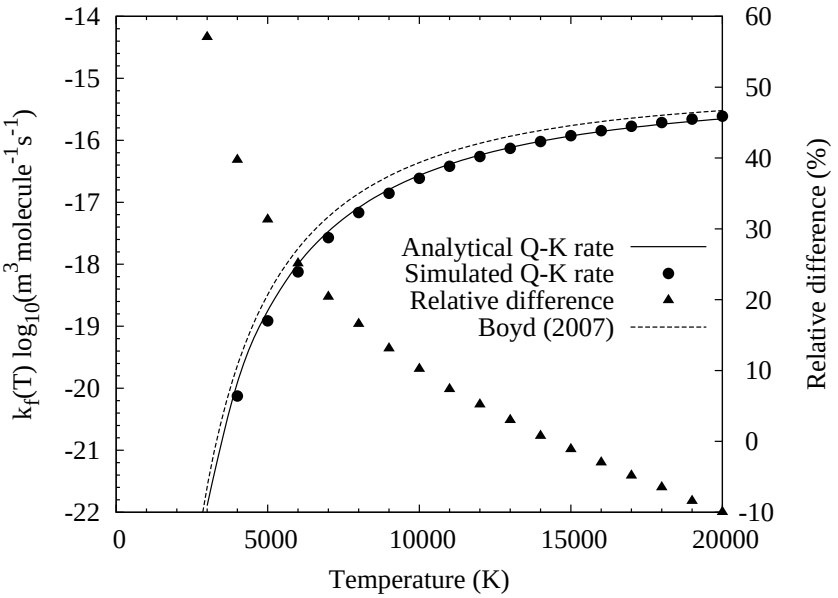

Figure 4.5: Dissociation rate coefficients for Type II dissociation, $O_2 + O \rightarrow O + O + O$.

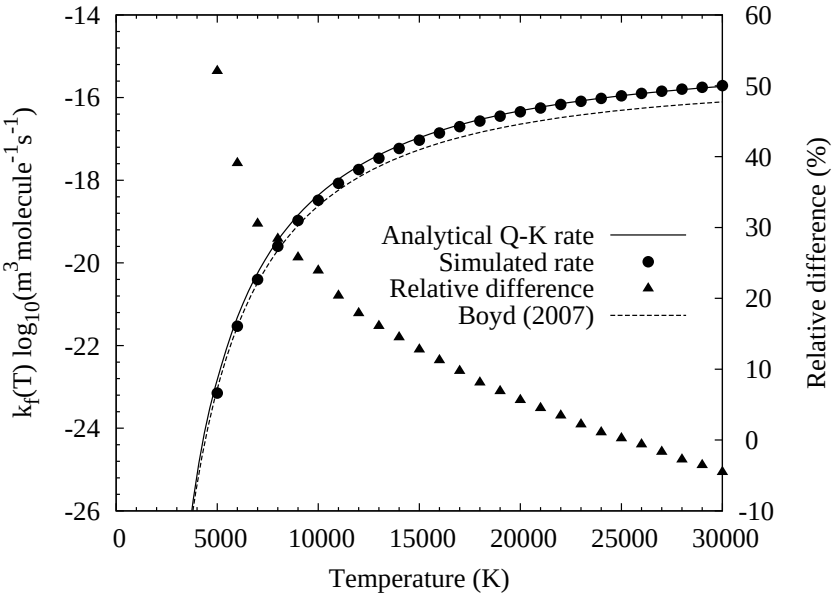

Figure 4.6: Dissociation rate coefficients for Type II dissociation, $N_2 + N \rightarrow N + N + N$.

4.2.3 Exchange Reactions

An exchange reaction contains one stable molecule and one radical before and after the reaction takes place. These reactions take the form $A + B \leftrightarrow C + D$, where A and C are molecules and B and D can be either atoms or molecules. In the five species air

model that we are currently considering, there are two exchange reactions:

$$NO + O \leftrightarrow O_2 + N, \tag{4.37}$$

and

$$N_2 + O \leftrightarrow NO + N. \tag{4.38}$$

Each of these has a forward (or endothermic) direction and a backward (or exothermic) direction.

The DSMC implementation of exchange reactions is that the reaction is possible if the collision energy E_c is greater than the activation energy E_a, with a probability of

$$P = \left(1 - \frac{E_a}{E_c}\right)^{3/2-\omega} \Bigg/ \sum_{i=0}^{i_{max}} \left(1 - \frac{ik_B\Theta_v}{E_c}\right)^{3/2-\omega}. \tag{4.39}$$

The summation in the denominator can be taken as unity when $E_a/k_B < \Theta_v$ [66]. The analytical QK reaction rates given by Bird are

$$k_f(T) = R_{coll}^{A,B} \exp\left(\frac{E_a^{A,B}}{k_B T}\right) \Bigg/ z_v(T)^A, \tag{4.40}$$

and

$$k_r(T) = R_{coll}^{C,D} \exp\left(\frac{E_a^{C,D}}{k_B T}\right) \Bigg/ z_v(T)^C, \tag{4.41}$$

where $k_f(T)$ and $k_r(T)$ are the forward and reverse reaction rates, respectively, $z_v(T)$ is the vibrational partition function, and R_{coll} is the collision rate between the species defined in the superscript and is given by Equation (4.18).

The default activation energy for forward exchange reactions is the heat of reaction E_r and for the reverse reactions it is zero. However, in order to ensure that the ratio of the forward to reverse reactions is in agreement with statistical mechanics predictions, it is necessary to adjust the activation energies. In addition, there is physical evidence for activation energies higher than the default values. For forward reactions, the adjusted activation energy $E'_{a,f}$ is

$$E'_{a,f} = E_r \left[1 + a\left(\frac{T}{273}\right)^b\right], \tag{4.42}$$

and for reverse reactions it is

$$E'_{a,r} = E_r \left[a \left(\frac{T}{273} \right)^b \right], \tag{4.43}$$

where a and b are tunable parameters. In addition, to eliminate the use of macroscopic temperature in Equations (4.42) and (4.43), a collision temperature T_{coll} is introduced

$$T_{coll} = \frac{m_r^{A,B} c_r^2}{(2k_B)\,(5/2 - \omega^{A,B})}, \tag{4.44}$$

based on the relative translational energy of a collision pair with a relative velocity c_r. The average of T_{coll} over all collisions is the macroscopic temperature T in an equilibrium gas, however T_{coll}^b is not necessarily equal to T^b, and so the coefficient a is replaced by a':

$$a' = \left[\left(5/2 - \omega^{A,B}\right)^b \Gamma\left(5/2 - \omega^{A,B}\right) / \Gamma\left(5/2 - \omega^{A,B} + b\right) \right] a. \tag{4.45}$$

Reaction	E_a (J)	a	b
$NO + O \rightarrow O_2 + N$	2.710×10^{-19}	0.085	0.65
$O_2 + N \rightarrow NO + O$	0	0.25	0
$N_2 + O \rightarrow NO + N$	5.175×10^{-19}	0.15	0
$NO + N \rightarrow N_2 + O$	0	0.07	0.62

Table 4.2: Parameters for our adjusted activation energies.

In the current work, we have chosen values of a and b for the four exchange reactions that ensure that the ratio of the forward to reverse reactions matches that of statistical mechanics. These are given in Table 4.2, and these values were found using Bird's QKRates program [47] and the modified forward activation rates stated in Reference [66].

4.2.4 Exchange Reactions in *dsmcFoam*

Adiabatic box simulations are performed to measure the reaction rate coefficients for each of the exchange reactions. The simulations have the same set-up as those for the

dissociation reactions discussed in §4.2.2. The particles were not allowed to move, but they were allowed to exchange energy in order to increase the sample size. Note that each exchange reaction can also be a Type II dissociation, so the pair is considered for exchange after it has been tested for dissociation. The TCE rates from Reference [64] are again plotted for comparison and the parameters are listed in Table 4.3. We also plot representative rates from the National Institute of Standards and Technology (NIST) experimental database [67] for each exchange reaction, which take the form:

$$k(T) = C_6 \left(T/298\right)^{C_7} \exp\left(-C_8/\Re T\right) \tag{4.46}$$

where $\Re$ is the universal gas constant expressed in kJ K^{-1} $mole^{-1}$ and the parameters are given in Table 4.4

Reaction	C_3	C_4	C_5
$NO + O \rightarrow O_2 + N$	1.389×10^{-17}	0	19700
$O2 + N \rightarrow NO + O$	4.601×10^{-15}	-0.546	0
$N_2 + O \rightarrow NO + N$	1.069×10^{-12}	-1	37500
$NO + N \rightarrow N_2 + O$	4.059×10^{-12}	-1.359	0

Table 4.3: TCE exchange reaction rate parameters [64] for the plotted reactions.

Reaction	C_6 (m^3 $molecule^{-1}$ s^{-1})	C_7	C_8 (kJ/mole)
$NO + O \rightarrow O_2 + N$	1.88×10^{-18}	1	173
$O2 + N \rightarrow NO + O$	4.47×10^{-18}	1	27.19
$N_2 + O \rightarrow NO + N$	3.01×10^{-16}	0	318
$NO + N \rightarrow N_2 + O$	7.11×10^{-17}	0	6.57

Table 4.4: NIST exchange reaction rate parameters [67] for the plotted reactions.

Figure 4.7 shows forward reaction rates for the $NO + O \leftrightarrow O_2 + N$ reaction: the TCE rate from Reference [64], and a reaction rate that is representative of the NIST database [67] is also included. The simulated QK rates are not in particularly good agreement with the analytical QK data; however, the agreement is almost exact if the macroscopic temperature with the unmodified a coefficient is imposed, rather than the collision temperature and a' used in these calculations. Both the TCE and the QK

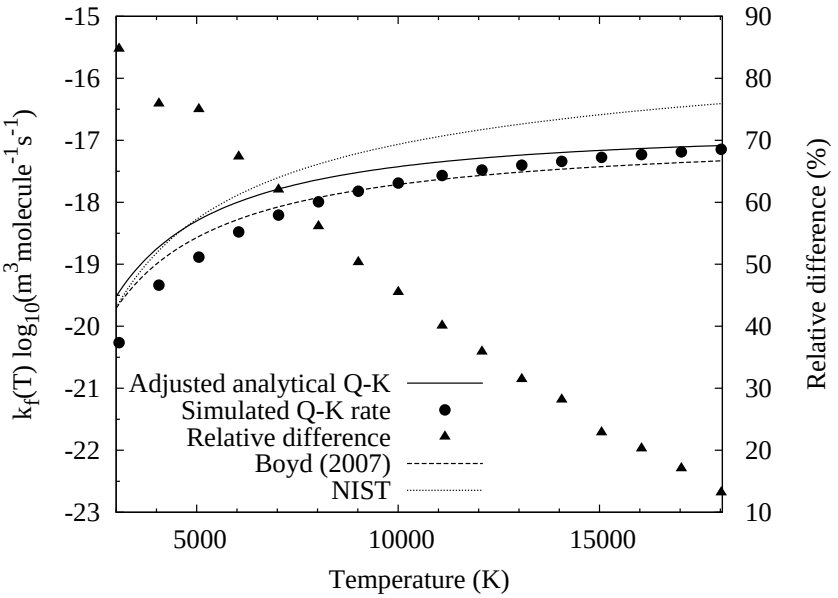

Figure 4.7: Forward exchange rate coefficients for $NO + O \leftrightarrow O_2 + N$.

rates are in reasonably good agreement with the NIST rates that are derived from experimental measurements.

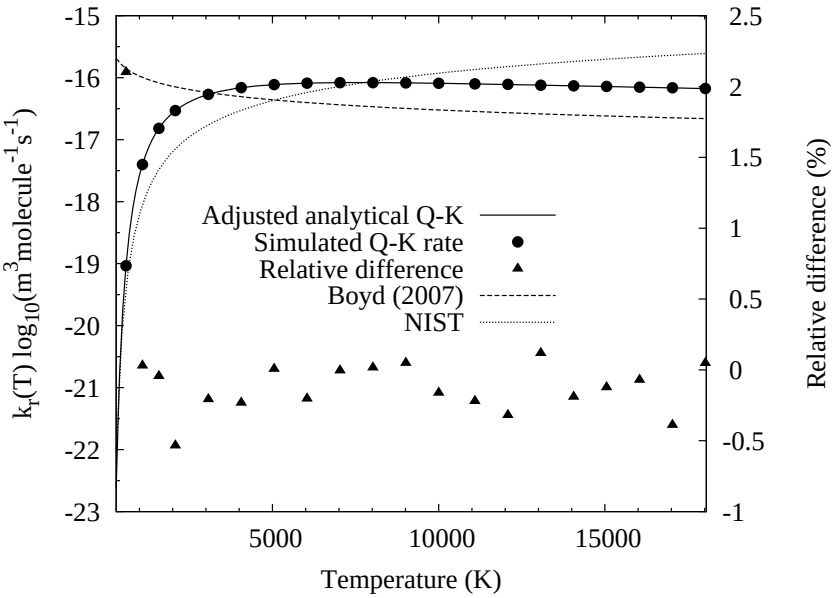

Figure 4.8: Reverse exchange rate coefficients for $NO + O \leftrightarrow O_2 + N$.

The corresponding reverse reaction rates are shown in Figure 4.8. Generally, good agreement is found between the QK, TCE and NIST rates, with the adjusted QK rate following the trend of the NIST database data more closely than the TCE rate. All

of the simulated and analytical QK rates are in very good agreement for the range of temperatures investigated here.

Figure 4.9 shows the forward reaction rates for the $N_2 + O \leftrightarrow NO + N$ reaction. The simulated and analytical QK rates are in good agreement, and all QK results are in good agreement with the accepted TCE and NIST rates.

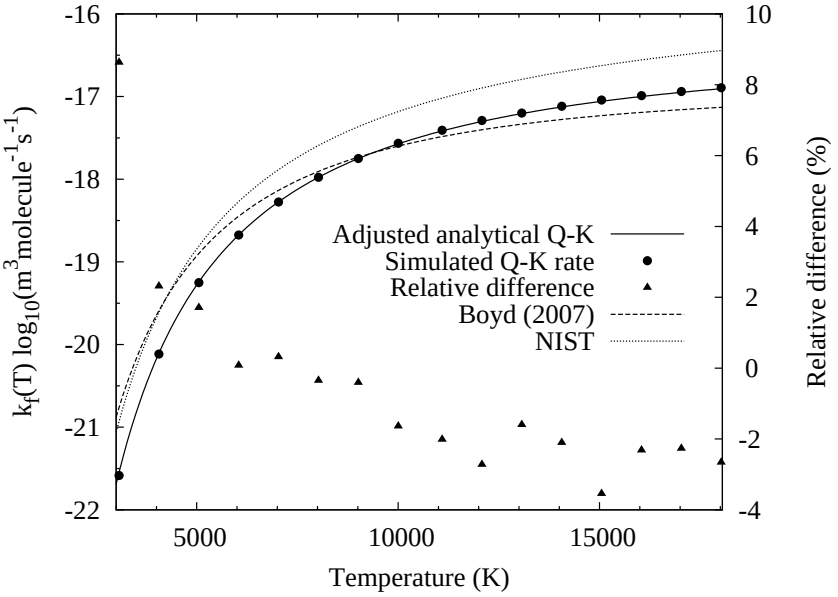

Figure 4.9: Forward exchange rate coefficients for $N_2 + O \leftrightarrow NO + N$.

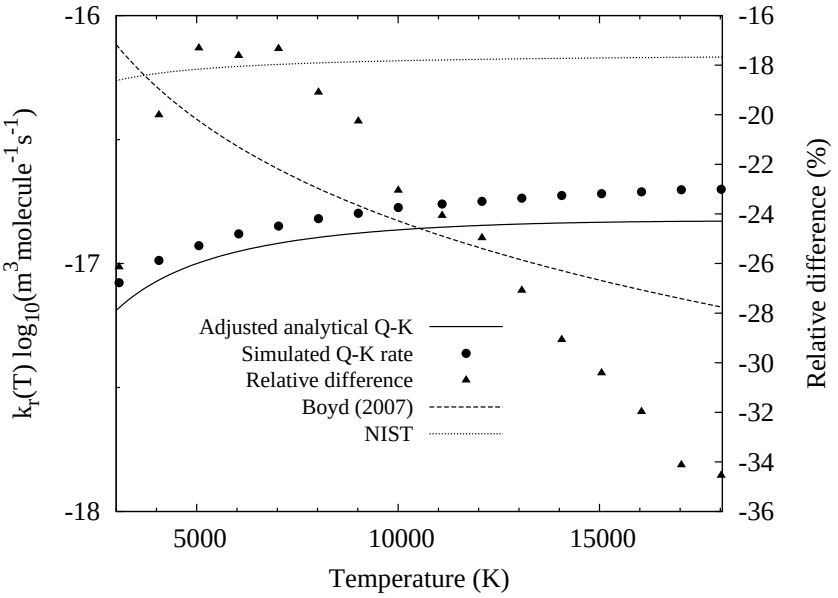

Figure 4.10: Reverse exchange rate coefficients for $N_2 + O \leftrightarrow NO + N$.

The reverse reaction rate is plotted in Figure 4.10. Similar to the forward $NO+O \leftrightarrow O_2 + N$ reaction, the differences between the analytical and simulated QK rates are significant, but the simulated rates are closer to the accepted NIST rates. Again, if the macroscopic temperature and the unmodfied a coefficient is used, the agreement between the simulated and analytical QK rates is excellent. Using the a' and T_{coll} does not lead to exact agreement unless the value of b is 0 or 1, as we have observed in these four exchange reactions.

We have implemented a set of dissociation and exchange reactions for a five species air model in *dsmcFoam*, using the newly developed QK chemical reaction model. All of the reaction rates are in reasonable agreement with currently accepted rates, but we find that the inclusion of the T_{coll} and a' procedures leads to significant differences between the analytical and simulated exchange reactions if the b parameter is not 0 or 1.

4.3 Measurement Framework

When using DSMC to solve engineering problems, it is important to be able to recover macroscopic properties in a meaningful and accurate manner, while minimising the statistical scatter. With this in mind we have added a robust and extendable measurement framework to *dsmcFoam*. This work is very closely related to the measurement framework in OpenFOAM's MD solver, *mdFoam*, which was first introduced by Borg [28]. This framework enables us to add a variety of models to measure macroscopic properties (such as velocity, pressure, temperature, heat flux) and microscopic properties that are important in DSMC simulations (velocity distribution functions, vibrational quantum level distribution functions, etc). All measurement tools have been fully parallelised, allowing them to be utilised in the most effective manner.

We use the `fieldPropertiesDict` input file to define what measurement models are used in each DSMC simulation. Each entry in the dictionary is a measurement model, and are read in at the start of the simulation. Basic particle properties (e.g. position, velocities, species type) are written out to hard disk every write interval, but these are only useful for viewing snapshots of particle distributions, making movies or most importantly for starting a simulation from a recent time-state. It would be

too memory intensive if these properties are first written out to disk every time-step and then re-read for measuring properties after the simulation has finished, because of the large number of time-steps we run our DSMC simulations for. Instead, we perform measurements "on the fly" and store only vital but less memory intensive macroscopic properties. These properties can written whenever they are required by the user. This also enables the measurement of fluxal properties such as mass flux, and allows the measurement framework to be extended to incorporate coupling of DSMC with a continuum technique in a future hybrid solver.

All measurements that we have introduced can be made over all species in the simulation, or can be restricted only to species that we are currently interested in simply by neglecting species identifications that are not required. All measurement tools have a capability to reset their measurements until steady state is achieved, and time averaging can then be activated during the run. Several different measurement techniques have been implemented and these are described in the following sections.

4.3.1 Method of Zones

The method of zones (MOZ) measurement technique enables the measurement of properties in a user-defined region of a DSMC domain. The measurement zone Z consists of a number of connected cells on the mesh. The measurement zone can therefore take any size and shape (including being the whole mesh), and be at any location on the mesh. Measurements performed in a zone can return only the spatial average of that zone; spatial gradients cannot be captured using this method.

The indexing feature of the DSMC algorithm means that *dsmcFoam* knows what particles are in each cell on the mesh after the movement stage. We take advantage of this to increase the efficiency of the measurement of zones technique, i.e. there is no need to loop over all particles in the simulation and determine if they are currently located in the measurement zone, we simply loop over the cell occupancy of each cell C in the measurement zone in turn, sampling the relevant properties of the particles. To return the correct values, it is necessary to account for the fact that the measurement is being made over all cells in the zone n^Z_{cells}, and so Equation (2.15) for the number

density in a zone n_Z becomes

$$n_Z = \frac{F_N \overline{N_Z}}{\sum_{C=1}^{n_{cells}^Z} V_C}, \tag{4.47}$$

where $\overline{N_Z}$ is the average number of DSMC particles in the zone over the measurement time interval, V_C is the volume of cell C, and F_N is the number of real atoms or molecules that each DSMC particle represents.

If parallel processing is used, the sampling zone may be split over a number of different processors. For example, the number of DSMC particles N in a zone Z split over n_{proc} processors is given by:

$$N_Z = \sum_{p=1}^{n_{proc}} \sum_{C=1}^{n_{cells}^Z} N_C, \tag{4.48}$$

where N_C is the number of DSMC particles in cell C. Immediately after they have been written to disk, the measured properties are reset to zero if the problem has not reached steady state, or they will continue to be accumulated if the simulation is already at its steady state.

4.3.2 Method of Bins

The method of bins (MOB) is a simple, common and useful method for measuring properties, particularly in micro-scale applications, where the macroscopic properties vary spatially, e.g. velocity in a pressure-driven micro-Poiseuille flow, or the heat flux profile in micro-Fourier flow. The technique splits a domain into a user-defined number of bins n_b, and measures the spatial average of the desired properties inside each bin b. The results are written to disk in histogram format.

The binning method is independent of the computational mesh, allowing for measurements that are finer or coarser than the sampling cells. We have merged the method of bins with the method of zones technique, such that a zone of cells in a domain is split into bins. This reduces the computational expense of the measurement because only particles in that zone need to be looped over, rather than every particle in the domain, many of which may not currently reside in any bin and so do not contribute

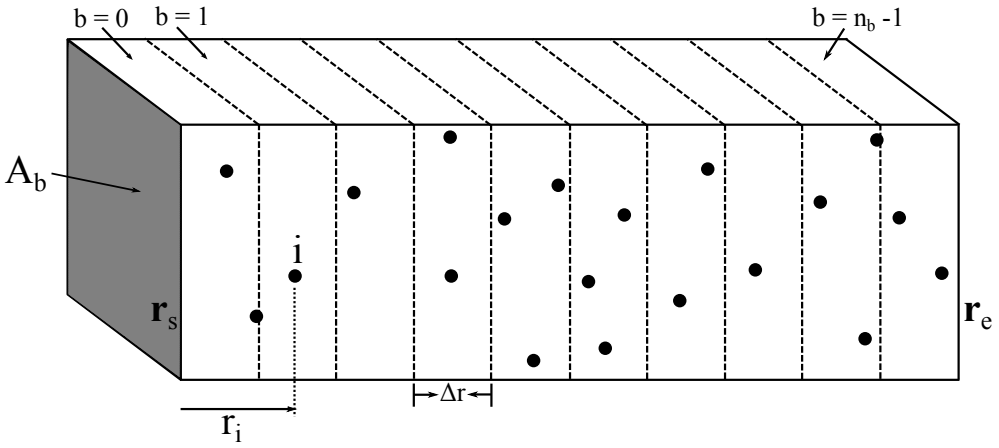

Figure 4.11: Schematic for sampling properties with the method of bins.

to the measurement.

We consider the region between a start point $\mathbf{r}_s$ and an end point $\mathbf{r}_e$, split into n_b equally sized bins, each with volume $A_b \Delta r$, as shown in Figure 4.11, with A_b the cross-sectional area of the bins (usually that of the domain), and Δr the width of one bin $(|r_s - r_e|)/n_b$. At each sampling interval, every particle i in the zone is looped over and the required properties from it are appended to the bin in which that particle is resident. The bin index b_i is calculated from the normal distance of the particle r_i from the start point r_s, i.e.

$$b_i = \left\lfloor \frac{(r_i - r_s)(r_e - r_s)}{\Delta r (|r_e - r_s|)} \right\rfloor . \tag{4.49}$$

A histogram is created with n_b entries, where the first column in the histogram is the centre position of the bins and the second is the property that is being measured. Similar to the MOZ technique, after each write interval the measured properties are reset to zero if the problem has not reached steady state. Currently, we have only implemented 1-dimensional planar bins, however as future work the *dsmcFoam* MOB technique could be extended to 2-dimensional bins [28], or radial bins for cylindrical geometries.

As an example of the bins measurement in use, we consider the case of rarefied force-driven Poiseuille flow. The working gas is hard sphere argon with a Knudsen number (based on the hard sphere mean free path and the length between the surfaces L) of 0.1. The gas temperature is initially 273 K and the surface temperatures are constant at 273 K and are modelled as fully diffuse. The normalised driving acceleration applied

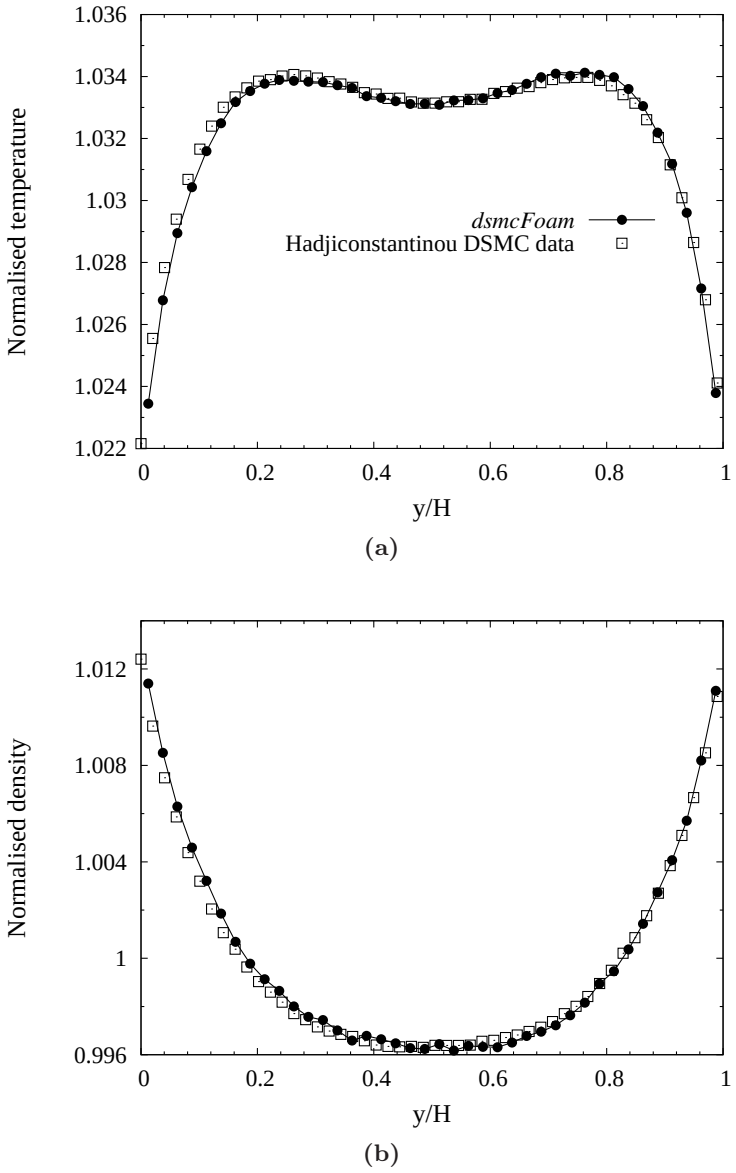

Figure 4.12: Measurement of (a) temperature normalised by the reference temperature of 273 K and, (b) density normalised with the average density in the system using the MOB measurement scheme.

to the particles is $\tilde{g} = 0.22$, where the normalisation scheme is $\tilde{g} = g\left(L/V_m^2\right)$, with $V_m = \sqrt{k_B T/m}$.

A domain of 30×30 cells is used to run the simulation, but we measure properties in 40 bins across the distance between the surfaces. Each bin had a total volume of 22.5 times the cell volume. A total run time of 18 hours resulted in a sample size of 2.75 million with 22,360 DSMC particles in the domain. The temperature and

normalised density profiles are plotted in Figure 4.12 and compared to independent DSMC data supplied by Hadjiconstantinou [68]. Each *dsmcFoam* data point is the calculated value at the centre of a bin. The density is normalised with the value of density that the domain was uniformly initialised with. Excellent agreement is found for both properties, and the dip at the centre of the temperature profile is characteristic of rarefied force-driven Poiseuille flow.

4.3.3 Fluxal Measurements

Macroscopic fluxes from particles crossing faces on the mesh can be measured, and this is particularly useful for measuring mass flow rates. The particle tracking algorithm in OpenFOAM [69] is used to keep track of particles as they cross faces on the mesh during a time step. In OpenFOAM, two neighbour cells P and Q are connected by a common face f and the face normal vector $\mathbf{n}_f$ is always defined as being positive in the direction of owner cell P to neighbour cell Q, as defined in Figure 4.13.

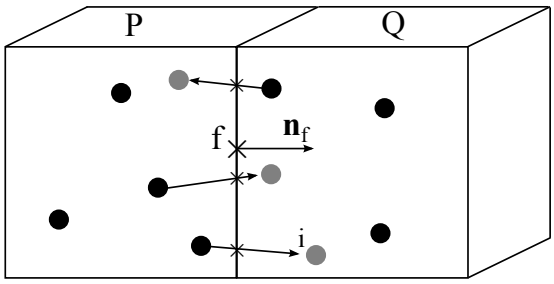

Figure 4.13: Schematic for sampling fluxes across faces.

The direction that a particle i crosses face f can be defined as $sgn(\mathbf{c}_i \cdot \mathbf{n}_f)$, which equals 1 if $\mathbf{c}_i \cdot \mathbf{n}_f > 0$, or -1 if $\mathbf{c}_i \cdot \mathbf{n}_f < 0$. A particle that moves on the plane of face f will have $\mathbf{c}_i \cdot \mathbf{n}_f = 0$ and so $sgn(\mathbf{c}_i \cdot \mathbf{n}_f) = 0$ for this case. This is measured and summed for all particles crossing all faces each time step.

The average mass flow rate crossing face f is then defined as:

$$\langle \dot{m}_f \rangle = \frac{1}{t_{av}} \sum_{i}^{\Delta N_f(t \to t_n)} m_i \; sgn(\mathbf{c}_i \cdot \mathbf{n}_f), \tag{4.50}$$

with

$$sgn\,(x) = \begin{cases} -1 & \text{if } x < 0 \\ 0 & \text{if } x = 0 \\ 1 & \text{if } x > 1 \end{cases} \tag{4.51}$$

where t_{av} is the physical time that the mass flow rate is averaged for, and $\Delta N_f(t \to t_n)$ is the total number of molecules that cross face f during the time period $t \to t+t_{av}$. The mass flux can be calculated from $\langle \dot{m}_f \rangle / A_f$, where A_f is the area of face f. Analogous to joining a group of cells in the MOZ technique, a group of faces can be joined and the mass flux measured over their entire area. Results are only written to disk for the user-defined faces that are selected.

Currently, only a mass flux measurement tool has been implemented in *dsmcFoam*, although the fluxal properties measurement framework could be extended to include momentum flux and energy flux measurement tools as future work, as described in Reference [28] for MD simulations.

In order to demonstrate the measurement of mass flux, a series of pressure-driven Poiseuille flows are performed for a large range of Knudsen number, the mass flow rate $\dot{m}$ is measured and normalised as follows:

$$Q = \frac{\dot{m} L \sqrt{2RT}}{h^2 w \left(P_{in} - P_{out}\right)}, \tag{4.52}$$

where L, h and w are the length, height and width of the planar Poiseuille flow geometry, respectively. A rarefaction parameter δ_m is defined at the average of the inlet and outlet Knudsen numbers (based on the variable hard sphere mean free path and the channel height h) Kn_m in each case as:

$$\delta_m = \frac{\sqrt{\pi}}{2Kn_m}. \tag{4.53}$$

The inlet to outlet pressure ratio in all cases is 3 and the aspect ratio of the planar Poiseuille geometries considered is 20. Our *dsmcFoam* results are compared to previous DSMC results [70] for the same aspect ratio in Figure 4.14. Experimental results from Ewart *et al.* [7] are also plotted for comparison. The DSMC results are in good agreement with one another and the agreement with the experimental data is excellent at low Kn and reasonable at high Kn. It has previously been noted [71] that the

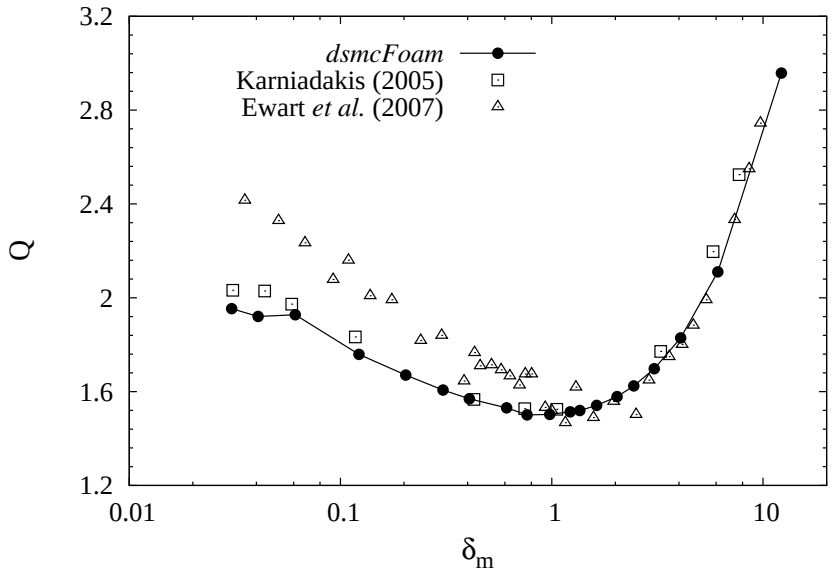

Figure 4.14: Normalised mass flow rate, showing the Knudsen minimum phenomenon.

asymptotic value that Q obtains is proportional to $\ln(L/h)$; since the experimental work was performed on geometries with very large aspect ratio ($L/h = 1000$), it is expected that the DSMC results for aspect ratio 20 will not match exactly. Unfortunately, it is not be possible to simulate an aspect ratio of 1000 using DSMC, as the velocities would be too low for a converged solution to be obtained in a practical time scale. The famous Knudsen minimum behaviour [72] can clearly be observed, where the normalised mass flow rate has a minimum at around $Kn = 1$.

4.3.4 Cell Measurements

A final measurement technique that has been implemented is that of macroscopic fields over all sampling cells in the mesh. This can be seen as a three-dimensional method of the bins approach, with spatial variation of properties in accordance with the coarseness of the mesh. *dsmcFoam* writes some useful fields, but lacks capability to measure some additional fields that could be of use. For example, it should be able to measure the mass density of a single species; but in its original version it can only measure the total mass density. In addition, due to the species-dependent form of the vibrational temperature measurement (see Equation (4.10)) it would not be possible to measure this variable for a gas mixture.

With this in mind, we have implemented a measurement framework that enables macroscopic properties to be measured and results are written to disk in a format that can be viewed in the same post-processing software as the fields that *dsmcFoam* was previously capable of producing. Every cell in the mesh is looped over at each measurement interval and the necessary particle properties are sampled. At averaging intervals (typically the write intervals) the accumulated particle properties are converted to the desired macroscopic property and written to disk. All of these measurement tools measure properties for an arbitrary number of species simply by ignoring any particles that are not of the desired species during the sampling steps.

Examples of measurement tools already implemented with this framework include vibrational temperature, overall temperature and mass density.

4.4 CLL Gas-Surface Interaction Model

In kinetic theory, a gas-surface interaction takes the form of a boundary condition that is applied to molecules when they are incident on a solid surface. The two most common gas-surface interactions employed in DSMC simulations are the Maxwell model and the Cercignani-Lampis-Lord (CLL) model. The Maxwell model was already implemented in *dsmcFoam*, and a detailed description of the model can be found in Reference [52]. The *dsmcFoam* implementation of this was benchmarked in Chapter 3.

The CLL model is based on a scattering kernel first proposed by Cercignani & Lampis [73] and was demonstrated to provide scattering angle distributions consistent with experimental data for a limited number of hypersonic test cases. The main features of this scattering kernel are that it is assumed that the normal and tangential components of the reflected velocity have separate accommodation coefficients; this is in contrast to the Maxwell model where only a single accommodation coefficient is required. In addition, the scattering angle is always a function of the incoming angle in the Cercignani-Lampis (CL) kernel; in the Maxwell model the scattering angle is independent of the incoming angle for the diffuse fraction. A DSMC implementation of the CL scattering kernel was proposed by Lord [74, 75] through a relatively simple algorithm, and the model was extended to account for rotational energy exchange at a surface. Lord later extended the CLL model further [76] to include vibrational en-

ergy exchange at a surface along with the capability to have diffuse reflections with incomplete energy accommodation.

The DSMC implementation of the CL model is that the post-interaction normalised normal component of the particle velocity u^* is given by:

$$u^* = \left[r_n^2 + (1 - \varrho_n)\, u^2 + 2r_n\, (1 - \varrho_n)^{1/2}\, u \cos\theta_1\right]^{1/2}, \tag{4.54}$$

with

$$\theta_1 = 2\pi R_{f,1}, \tag{4.55}$$

and

$$r_n = \left[-\varrho_n \ln\left(R_{f,2}\right)\right]^{1/2}, \tag{4.56}$$

where u^* and u are respectively, the post- and pre-interaction normal components of the velocity of the particle normalised by the most probable thermal velocity based on the local temperature of the surface. The normal energy accommodation coefficient $\varrho_n = \sigma_n$ where σ_n is the normal momentum accommodation coefficient; $R_{f,1}$ and $R_{f,2}$ are random fractions selected uniformly between 0 and 1.

The post-interaction normalised tangential component v^* in the interaction plane is:

$$v^* = (1 - \varrho_t)^{1/2}\, v + r_t \cos\theta_2, \tag{4.57}$$

where

$$\theta_2 = 2\pi R_{f,3}, \tag{4.58}$$

$$r_t = \left[-\varrho_n \ln\left(R_{f,4}\right)\right]^{1/2}, \tag{4.59}$$

and the other post-interaction tangential component w^* is

$$w^* = r_t \sin\theta_2, \tag{4.60}$$

with $R_{f,3}$ and $R_{f,4}$ two more random fractions selected uniformly between 0 and 1, and the tangential energy accommodation coefficient $\varrho_t = \sigma_t(2 - \sigma_t)$ where σ_t is the tangential momentum accommodation coefficient (TMAC).

For diatomic molecules with rotational energy, a rotational energy coefficient ϱ_r is

introduced with its own normalisation scheme, and the selection of post-interaction rotational energy ω_r^* is analogous to the selection of a normal velocity component, i.e:

$$\omega_r^* = \left[r_r^2 + (1 - \varrho_r)\, \omega_r^2 + 2 r_r\, (1 - \varrho_r)^{1/2}\, \omega_r \cos\theta_3 \right]^{1/2}, \tag{4.61}$$

with

$$\theta_3 = 2\pi R_{f,5}, \tag{4.62}$$

and

$$r_r = \left[-\varrho_r \ln\left(R_{f,6}\right) \right]^{1/2}. \tag{4.63}$$

Polyatomic molecules require special treatment and the details of this can be found in Reference [74].

We have implemented the CLL gas-surface interaction model in *dsmcFoam*. Our results for the scattering angle of DSMC particles incident on two positions of a flat plate subjected to rarefied hypersonic flow are compared to those from the MONACO code [52, 53]. The geometry and case set up is the same as that previously considered in §3.2.

The flat surface is now considered to reflect particles using the CLL model. The normal momentum accommodation coefficient σ_n is not usually well known [77], and therefore it, along with the rotational energy accommodation coefficient ϱ_r, is maintained as unity for all of the simulations performed here. Different values of σ_t are simulated. For each case, the scattering angles of each particle are recorded at two stations on the flat plate surface: at the leading edge of the plate (0 mm), and at a position 5 mm from the leading edge. Our *dsmcFoam* results are compared to those from MONACO in Figure 4.15.

Good agreement is found between the two DSMC codes. When both σ_t and σ_n are unity, it is clear that the CLL model gives the same scattering angle probability as a fully diffuse Maxwellian surface (see Figure 3.6), and that the *dsmcFoam* implementation captures this behaviour. As the value of σ_t is reduced, the scattering angle probability becomes biased towards the freestream direction and this is in good agreement with the MONACO results.

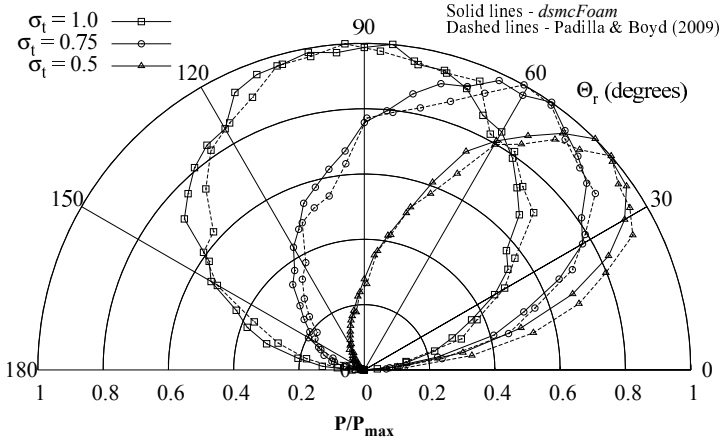

Figure 4.15: CLL scattering angle probabilities Θ_r for different values of TMAC at (a) 0 mm, and (b) 5 mm positions on the flat plate surface.

4.5 Summary

We have undertaken the implementation of some important new features in *dsmcFoam*, and provided descriptions and validations of this procedure. Molecular vibrational energy has been added to the code, and has been benchmarked against analytical solutions for some simple properties, and previous DSMC work for relaxation to equilibrium. The first stages of implementing the modern quantum-kinetic chemical reactions model have been shown, with the simulated DSMC reaction rates compared to their analytical counterparts, and total collision energy rates. Most of the reactions show good agreement; however, the DSMC results for the exchange reaction with the lowest activation energy tend to greatly overpredict the rate, according to the analytical QK

solution. It has been demonstrated that using the collision temperature T_{coll} and the modified a coefficient does not give particularly good agreement between the simulated and analytical QK rates unless the b coefficient is 0 or 1. Future work in this area could include performing the particle splitting and the associated conservation of mass, momentum and energy, in order to enable more realistic simulations of hypersonic flows to be performed using *dsmcFoam*.

A new measurement framework has been introduced, and this includes measurements in bins that are independent of the DSMC mesh, zones comprised of joined groups of cells, and fluxal properties at faces. Examples of the use of this measurement framework have been provided, including an example of the Knudsen minimum phenomenon with a comparison to experimental measurements of mass flow rates. This measurement framework can be used to help develop a method for performing hybrid continuum-DSMC simulations in the future.

We have introduced the CLL gas-surface interaction model to *dsmcFoam* and it has been partially validated by comparing the scattering angle probability distributions to those presented by Padilla [52, 53], which were produced using the MONACO software. Future work on the CLL model will include further validation studies for the post-interaction rotational energy distribution, and include the capability to deal with vibrational energy as described by Lord [76].

Chapter 5

Microscale Applications

The only way of discovering the limits of the possible
is to venture a little way past them into the impossible.
- Arthur C. Clarke

Having benchmarked and extended *dsmcFoam* in previous chapters, we now apply the code to an emerging engineering field: gas flows at the micro-scale. This is an increasingly important area of research for the design of micro-electro-mechanical system (MEMS) technologies such as micro-pumps, micro-turbines and micro-fuel cells. Gas flows in MEMS are characteristically low speed and often driven by a pressure gradient. Unlike more traditional hypersonic DSMC simulations, it is likely that particles will have thermal velocities that will be orders of magnitude larger than the stream velocity. This stochastic motion makes it probable that particles do not flow uninterrupted in the streaming direction, but instead may, for example, exit at the inlet or enter at the outlet. The velocity profiles at the inlet and outlet are not known due to current experimental limitations at the micro-scale; pressure and temperature are usually the only known thermo-mechanical properties at the boundaries.

The thermal velocities of the particles being at least an order of magnitude larger than the macroscopic velocity also makes it statistically difficult to recover fields such as the macroscopic velocity. A large sample size is required to reduce the statistical error in the measurement of certain macroscopic fields to an acceptable level. Simulations involving very low velocities ($Ma < 0.01$) are often impractical as the required sample

sizes would simply be too large [46]. This problem of statistical scatter restricts particle methods such as DSMC to the study of shorter micro-channels operating at much higher velocities than experimental micro-channels. However, recently, variance reduction techniques have begun to offer the promise of allowing particle methods to be used for extremely small Mach number or temperature difference problems [78, 79].

In this chapter we describe the implementation of sub-sonic implicit boundary conditions in *dsmcFoam*, propose an extension to these boundary conditions to account for rotational non-equilibrium, and apply these boundaries to the problem of gaseous flow in micro-channels with bends. The non-planar problem of cylindrical Couette gas flow between two concentric microscale cylinders is also considered.

5.1 Pressure Boundary Conditions

Piekos & Breuer [80] proposed pressure boundary conditions for low speed flows in micro-channels, intended to be applied far from the high and low pressure reservoirs, and they achieved excellent agreement between their DSMC results and an analytical solution in the slip flow regime for a straight micro-channel of aspect ratio 30. Nance *et al.* [81] developed a set of boundary conditions suitable for DSMC simulation of low speed flows in micro-channel geometries by adapting computational fluid dynamics theory of characteristics boundary conditions at the exit boundary and using particle flux conservation at the inlet. They found that elongated cell sizes in the streamwise direction provided solutions consistent with much smaller (i.e. fraction of the mean free path) cell sizes. The macroscopic gradients in low speed flows tend to be small in the stream-wise direction, enabling a large decrease in the computational expense of a micro-channel simulation. Again, only straight micro-channel geometries were considered in this work.

Wu *et al.* [82] developed low speed boundary conditions using particle flux conservation at both inlet and outlet boundaries, and applied these boundaries to geometries that were not simply straight micro-channels. For example, they simulated argon gas flow in a pressure-driven T-junction geometry with a single inflow boundary and two exit boundaries [83].

Liou & Fang [84–86] improved the Nance *et al.* boundary conditions by removing

the particle flux dependence at the inlet and replacing it with a first order extrapolation and time average of the streamwise velocity from the boundary cells. The theory of characteristics outlet boundary remained unchanged from the Nance *et al.* implementation. This improved convergence speed at the inlet boundaries by reducing the statistical scatter. A variety of benchmark cases for straight micro-channels with aspect ratio 5 were presented. Wang & Li [87] further improved the convergence behaviour of these boundary conditions by applying the theory of characteristics at the inlet in addition to the outlet. They also presented work for flow in a micro-channel with a single ninety-degree bend, but this was not a detailed study of micro-channels with bends.

More recently, Ye *et al.* [88–90] proposed boundaries similar to those of Nance *et al.* [81] and Wang & Li [87], but they used different correction factors at the inlets and outlets in order to improve the heat transfer results in micro-channels whose surface temperature is substantially different from the gas inflow temperature.

The general starting point for the treatment of a boundary condition, as described in the literature, is to impose a particle flux at an inlet or outlet boundary. The rate of particle insertion, $\dot{N}$, can be computed from the equilibrium Maxwell-Boltzmann distribution (see Equation (2.1)) The streaming velocity profile at the inlet boundary is generally not known, so we must rely on boundary values of temperature, density and pressure to derive the corresponding local velocity required in Equation (2.1).

5.1.1 Upstream boundaries

Here we describe the boundary conditions proposed by Wang & Li [87]. Target gas properties of pressure P_{in} and temperature T_{in} are prescribed at the inflow boundary, and the perfect gas law is used to calculate the inlet number density n_{in}

$$n_{in} = \frac{P_{in}}{k_B T_{in}}. \tag{5.1}$$

Based on the theory of characteristics, the stream-wise u_{in} and tangential v_{in} velocities at two-dimensional inlet boundary faces f, using values from the boundary cell centres

j, are calculated as

$$(u_{in})_f = u_j + \frac{P_{in} - P_j}{\rho_j a_j}, \tag{5.2}$$

and

$$(v_{in})_f = v_j, \tag{5.3}$$

where u_j and v_j are first order extrapolations from the cells attached to the relevant boundary face, ρ is mass density and a is the local speed of sound. The pressure P_j is calculated in these boundary conditions from the overall temperature as:

$$P_j = \rho_j R \left[\left(\frac{3T_{tr} + \bar{\zeta}_{rot} T_{rot}}{3 + \bar{\zeta}_{rot}} \right) \right]_j. \tag{5.4}$$

5.1.2 Downstream boundaries

At the exit boundaries, only the pressure is defined and the boundary conditions are the same as those used by Nance *et al.* [81] and Liou & Fang [84]:

$$(\rho_{out})_f = \rho_j + \frac{P_{out} - P_j}{(a_j)^2}, \tag{5.5}$$

$$(u_{out})_f = u_j + \frac{P_j - P_{out}}{\rho_j a_j}, \tag{5.6}$$

$$(v_{out})_f = v_j, \tag{5.7}$$

$$(T_{out})_f = P_{out} / \left[R \left(\rho_{out} \right)_f \right]. \tag{5.8}$$

The pressure P_j is again calculated from Equation (5.4). The process for selecting the required translational and rotational energies for particles at the boundaries is standard in DSMC and details can be found in Reference [21].

5.1.3 Benchmarking

Micro-Couette Flow

We have implemented the boundary conditions described above in *dsmcFoam* and here we compare results from simulations using them against some fundamental test cases and Navier-Stokes-based analytical solutions. All test cases use the VHS binary colli-

sion model with the NTC collision partner selection routine and the Larsen-Borgnakke rotational energy exchange model. The vibrational mode has been excluded in the current work as it is not likely to be active at the low temperatures considered.

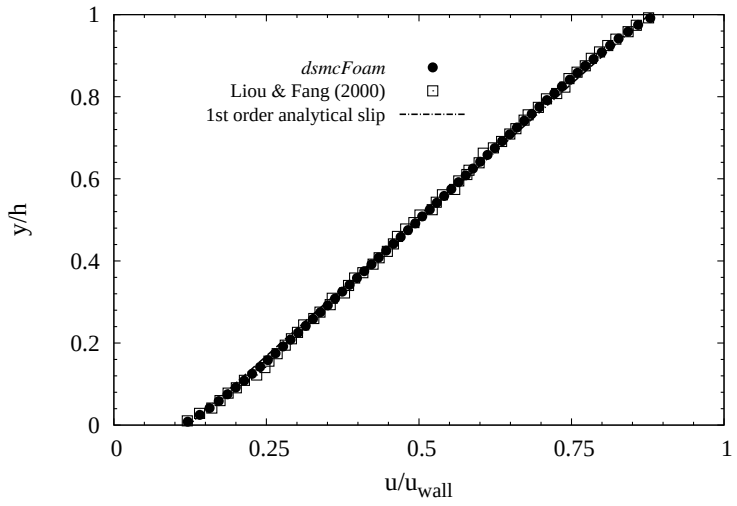

(a)

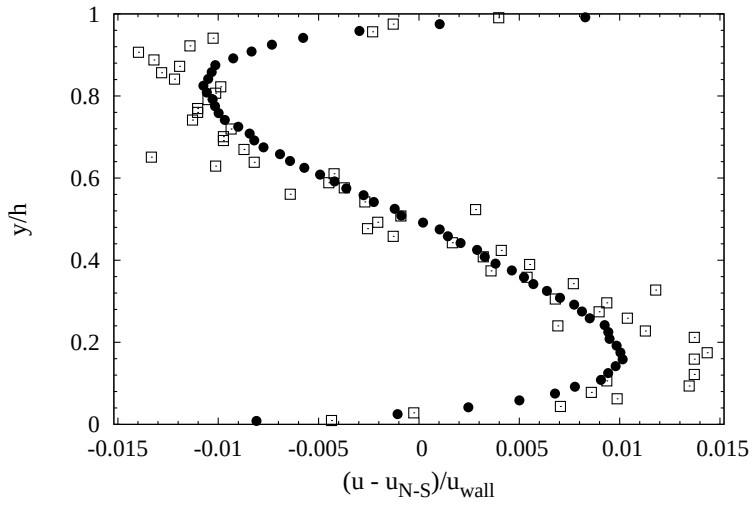

(b)

Figure 5.1: Comparisons with previous numerical work from Reference [84] for the micro-Couette flow geometry: (a) cross-sectional velocity profile, and (b) deviation from the continuum velocity solution. All velocities have been normalised with the velocity of the moving wall, i.e. 100 m/s.

The first case tested is a two-dimensional micro-Couette flow of nitrogen gas, first presented in Reference [84]. Both wall temperatures and the inlet gas temperature were set to 300 K. The lower wall is stationary and the upper wall moves with a

velocity of 100 m/s. The inlet and outlet pressures are equal at 0.83 *atm*. The domain channel height is 0.4 μm, so the Knudsen number of this case is 0.163, which is in the transition flow regime. A channel length of 4 μm was chosen and was meshed using 100 $\times$ 60 computational cells. The simulation contained around 320,000 DSMC simulator particles and was performed in parallel on 4 processors. A total of 400,000 samples required 20 hours of run time, and the macroscopic velocity was measured in 60 bins across the channel height using the MOB method described in §4.3.2. It should be noted that the inlet and outlet are not periodic; the implicit boundary conditions are being used to introduce new particles at both the inlet and outlet.

Figure 5.1 shows the results from *dsmcFoam* compared with the DSMC results presented by Liou & Fang [84] and an analytical continuum-based solution. Excellent agreement is seen in Figure 5.1(a) between the *dsmcFoam* results and those of Liou & Fang. Figure 5.1(b) shows the difference between both DSMC solutions and the continuum result. The continuum solution is clearly unable to capture the non-linear nature of the velocity profile at this Knudsen number. Again, excellent agreement is found between the DSMC solutions, although the *dsmcFoam* results display significantly less scatter.

Micro-Poiseuille Flow

The second test case is the simple micro-channel Poiseuille flow of nitrogen gas. The geometry is a channel of height 0.4 μm and 2 μm length, meshed with 100 $\times$ 60 computational cells. The surface and inlet gas temperatures are set to 300 K. The outlet pressure is atmospheric, and the inlet to outlet pressure ratio is 2.5. The Knudsen number at the inlet is 0.055 and 0.123 at the exit. The simulation contained around 225,000 DSMC simulator particles at steady state, ensuring that there were around 20 particles per cell at the exit, and was solved in parallel on 2 processors on a desktop PC with an i7 processor. A total of 250,000 samples required a run time of 18 hours.

Figure 5.2 shows our results from *dsmcFoam* compared with previous numerical work of the same case from both Liou & Fang [84] and Roohi *et al.* [91]. A first order analytical slip solution is also provided for reference. Good agreement between the DSMC data, and good agreement with the continuum solution, can be seen in

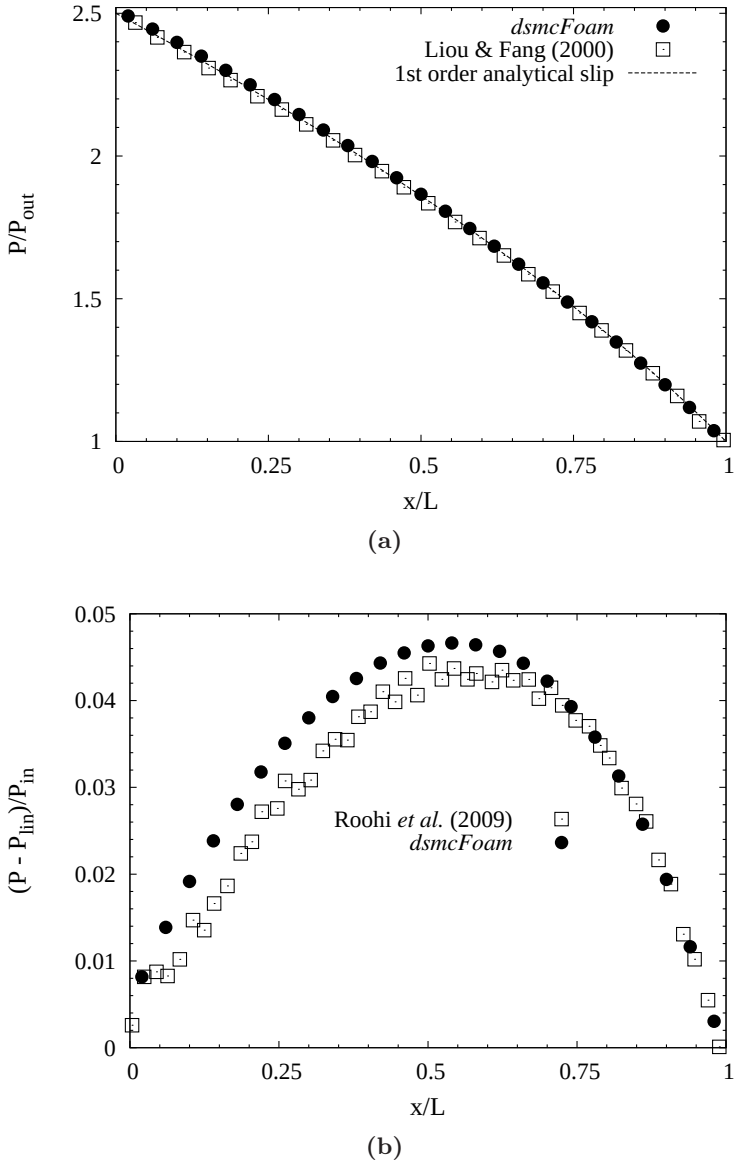

Figure 5.2: Comparisons with previous numerical work from References [84, 91] for the micro-Poiseuille flow geometry: (a) streamwise centre-line pressure distribution, and (b) deviation from a conventional linear pressure profile.

Figure 5.2(a). The relative deviation from a conventional linear pressure drop along the channel centre-line is show in Figure 5.2(b). The results published in Reference [91] were obtained using Bird's DS2V code [47]; considering that different solvers and meshes were used, the agreement between the results for this sensitive parameter is good.

Case	P_i (kPa)	P_{e1} (kPa)	P_{e2} (kPa)	P_i:P_{e1}:P_{e2}
I	26.79	8.93	8.93	3:1:1
II	26.79	8.93	17.86	3:1:2
III	26.79	17.86	8.93	3:2:1

Table 5.1: Micro-manifold inlet and outlet pressures.

Micro-Manifold Flow

The final test case consists of the flow of argon gas through a T-junction micro manifold, which was investigated first by Wu & Tseng [83]. A diagram of the geometry is shown in Figure 5.3, where the height h is 1 μm, H is 3 μm and the length L is 7 μm. In this case the geometry has two outlet channels and one inlet channel that require separate treatment with pressure boundary conditions. Three different pressure configurations are tested, as detailed in Table 5.1, where P_i is the inlet pressure, and P_{e1} and P_{e2} are the outlet pressures. The working gas is argon; all surface temperatures and gas inlet temperatures are constant at 300 K. The inlet Knudsen number, based on the VHS mean free path and the micro-manifold height, is 0.2. The time step employed was 8.33 $\times$ 10^{-11} s for all cases. Our *dsmcFoam* results use the boundary conditions described above, but the Wu & Tseng results used boundary conditions which employ particle flux conservation at both inlets and outlets.

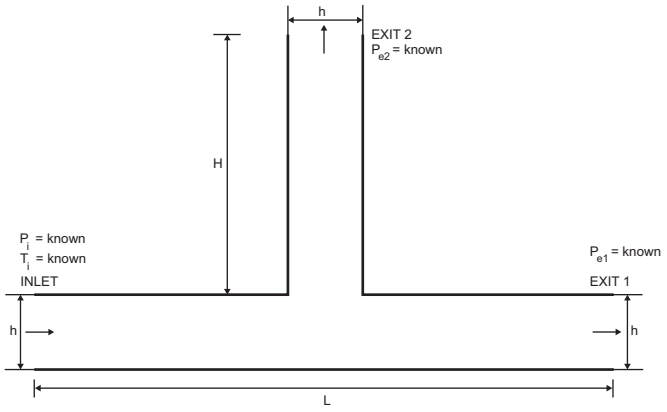

Figure 5.3: Schematic of the micro-manifold test case geometry [83].

Table 5.2 lists the results for the normalised mass flow rates at each inlet and outlet boundary. All of the mass flow rate results from *dsmcFoam* exhibit less than 0.01% statistical uncertainty based on the standard error from the standard deviation of the

Case	P_i:P_{e1}:P_{e2}	$(\dot{m}_i/\dot{m}_{i,I})$	$(\dot{m}_i/\dot{m}_i)$	$(\dot{m}_{e1}/\dot{m}_i)$	$(\dot{m}_{e2}/\dot{m}_i)$	Summation	Error (%)
I	3:1:1	1.00	1.00	0.541	0.465	1.006	0.60
I	**3:1:1**	**1.00**	**1.00**	**0.534**	**0.466**	**0.9999**	**-0.002**
II	3:1:2	0.755	1.00	0.981	0.028	1.009	0.90
II	**3:1:2**	**0.758**	**1.00**	**0.958**	**0.042**	**0.9999**	**-0.005**
III	3:2:1	0.751	1.00	0.098	0.910	1.008	0.80
III	**3:2:1**	**0.744**	**1.00**	**0.0878**	**0.912**	**0.9999**	**-0.0095**

Table 5.2: Mass flow rate results for the micro-manifold flow cases; *dsmcFoam* results in bold text. $\dot{m}_{i,I}$ refers to the mass flow rate at the inlet for Case I.

instantaneous samples. The Wu & Tseng results are displayed in standard text and the *dsmcFoam* results are presented below them in bold font. The summation column has been calculated as $(\dot{m}_{e1} + \dot{m}_{e2})/\dot{m}_i$ and the error as $(\dot{m}_{e1} + \dot{m}_{e2} - \dot{m}_i)/\dot{m}_i$.

Good agreement has been found with the results of Wu & Tseng. The summation values from *dsmcFoam* are closer to unity than the Wu & Tseng results and so the percentage errors in the conservation of mass are as much as two orders of magnitude smaller for the *dsmcFoam* results.

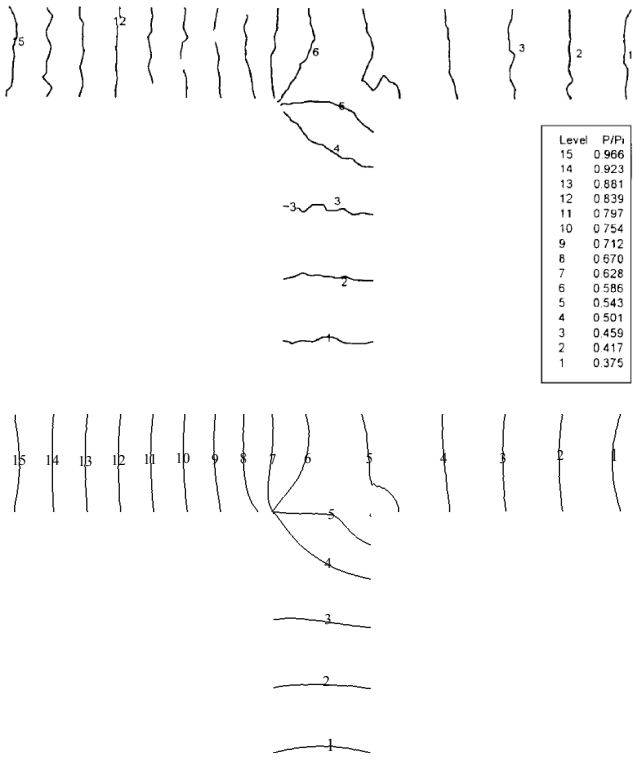

Figure 5.4: Micro-manifold flow: pressure contours for Case I. Top: Wu & Tseng [83]. Bottom: *dsmcFoam*.

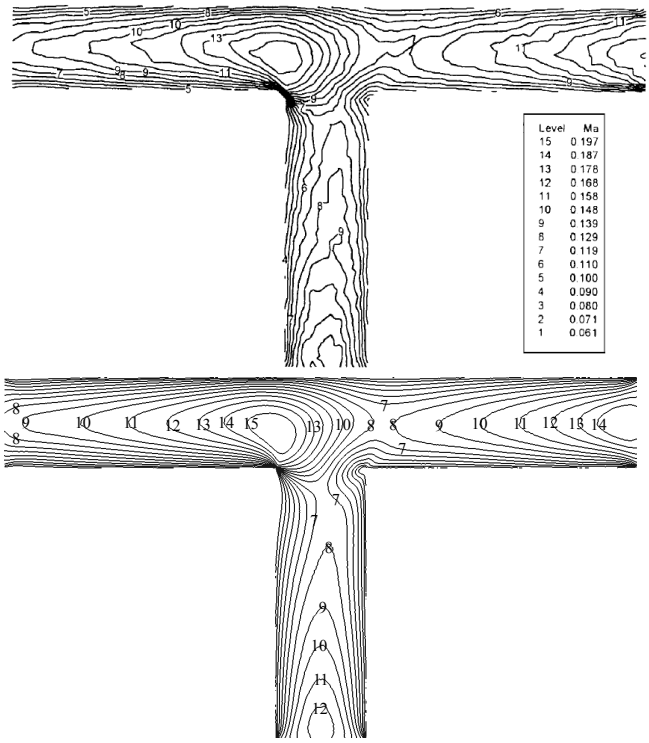

Figure 5.5: Micro-manifold flow: Mach number contours for Case I. Top: Wu & Tseng [83]. Bottom: *dsmcFoam*.

Figures 5.4 and 5.5 compare contours of pressure and Mach number for Case I from *dsmcFoam* with those presented by Wu & Tseng [83]. Excellent agreement has been found in both cases. The *dsmcFoam* simulation contained around 285,000 DSMC particles at steady state, and the results have been averaged for 590,000 time steps in parallel on 6 cores for a total run time of around 64 hours, and they exhibit much less scatter than the Wu & Tseng results.

5.2 Non-Equilibrium Boundary Conditions

The outlet boundary conditions described in §5.1.2 are essentially CFD boundary conditions that have been applied to DSMC simulations. They therefore inherently assume the gas is always in perfect thermodynamic equilibrium. Here, we propose that this is not the case and so develop a modified outlet boundary condition that accounts for rotational non-equilibrium. According to the kinetic theory of dilute gases [21, 92, 93], the pressure should be measured using the translational temperature, as it depends

only on the translational kinetic motions of the molecules. If the gas is in perfect thermodynamic equilibrium, the overall temperature will be equal to both the translational and rotational temperatures and so this is not an issue. However, it is not certain that a gas will remain in equilibrium along the length of a micro-channel, particularly if the inlet to outlet pressure ratio is high or the aspect ratio of the micro-channel is small.

As a gas travels downstream under the influence of a pressure gradient, the density decreases and the gas expands and cools. This decrease in thermal energy per unit mass initially appears in the translational mode, and is redistributed to the rotational mode through inter-molecular collisions, only after a corresponding relaxation time [94]. Although this rotational relaxation time is not large, if the gas is sufficiently rarefied there may not be enough molecular collisions occurring for the translational and rotational energies to equilibrate with one another. If the energy is not being redistributed to the rotational mode effectively enough, there will be a local deficit of energy in the translational mode compared to an equilibrium gas of the same density and total energy. This in turn means that the pressure will be lower than in the corresponding equilibrium gas.

A new form of the characteristics-based boundary conditions is proposed here. At the inlet, the boundary conditions remain unchanged from those of Wang & Li [87], which means that it is assumed that the gas is always in rotational equilibrium at the inlet. At the outlet, a state of rotational equilibrium is not assumed and the boundary conditions have been modified as follows to account for a degree of non-equilibrium between the translational and rotational modes. All of the following macroscopic properties are measured after the movement and collision stages and are time-averaged for the entire duration of the simulation. The pressure P_j in outlet boundary cells is measured as:

$$P_j = n_j k_B \left(T_{tr}\right)_j . \tag{5.9}$$

The mass density and velocities at the exit boundaries are then calculated as described in §5.1.2, but with our new definition of pressure included in the relevant terms.

The translational temperature at the exit boundary $\left(T_{tr}\right)_{out}$ is calculated using the perfect gas law:

$$\left[\left(T_{tr}\right)_{out}\right]_j = P_{out} / \left[k_B \left(n_{out}\right)_f\right], \tag{5.10}$$

and the rotational temperature at the exit boundary $(T_{rot})_{out}$ is simply taken as a first order extrapolation of the measured rotational temperature from the boundary cell, i.e.

$$[(T_{rot})_{out}]_f = (T_{rot})_j \,. \tag{5.11}$$

When particles are introduced at the boundaries, they are assigned translational energies based only on the value of $(T_{tr})_{out}$ by substituting this term into Equation (2.2) for T_{in}. Use of Equation (2.1) to calculate the entering particle flux means that translational equilibrium is being assumed at both the inlet and outlet. Their rotational energies are assigned only from the value of $(T_{rot})_{out}$ and the usual rotational energy selection routine. In this way a more realistic representation of gas flows with a degree of rotational non-equilibrium can be modelled.

5.2.1 Rotational non-equilibrium

In order to demonstrate that a gas may be out of rotational equilibrium inside a micro-channel geometry, a test case from the literature is chosen and speed distribution functions at various locations in the channel are measured and compared to the equivalent equilibrium distribution functions.

The chosen test test case is a micro-Poiseuille flow from Liou & Fang [84]. The channel geometry and surface temperature are the same as those in §5.1.3. The inlet pressure is 72640 Pa, with an inlet-to-outlet pressure ratio of 4.54. The working gas is nitrogen and the Knudsen number based on the channel height and the VHS mean free path ranges from 0.19 at the inlet to 0.72 at the outlet. The boundary conditions used for the current problem are those described in Reference [87].

To remain consistent with the test case in the literature, 100×60 regular rectangular computational cells are used to mesh the computational domain and the system has around 180,000 DSMC simulator particles at steady state. The method of zones measurement technique (§4.3.1) was used to measure the temperature and speed distribution functions in each of the measurement zones shown in Figure 5.6 in order to determine whether the system is in local rotational equilibrium at these points.

Around 1 million statistical samples were employed to obtain the following results, and the problem was solved in parallel on 2 processors. The total run time was 47

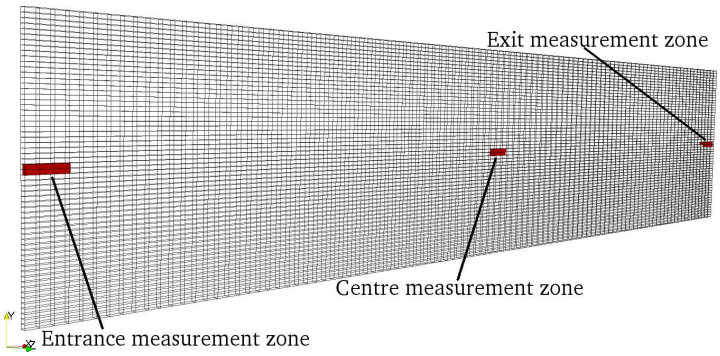

Figure 5.6: Snapshot of the mesh showing the measurement zones.

hours. Figure 5.7 shows the measured speed distribution functions in the entrance and exit measurement zones, alongside the equilibrium speed distributions based on the measured value of overall temperature in the respective measurement zones. If the gas is in rotational equilibrium, the measured distribution should match the theoretical one exactly. In the entrance measurement zone this is the case, as as is the case in the centre measurement zone (not shown here); however, in the exit measurement zone the measured distribution is shifted slightly to the left of the theoretical one and has a slightly higher peak value. This is consistent with a cooler distribution function and comes about because a degree of rotational non-equilibrium is present by the exit.

As discussed previously, the gas expands and the thermal energy per unit mass decreases as it travels downstream. The translational mode cools first and the rotational mode comes into equilibrium with this only after a certain relaxation time. This relaxation process occurs through inter-molecular collisions, but in this moderately rarefied flow there are not enough collisions occurring for the rotational mode to come into equilibrium with the translational mode. This means that the translational temperature in the exit measurement zone is significantly lower than the rotational temperature. The overall temperature is a weighted average of the translational and rotational temperatures, so this will also be higher than the translational temperature; hence the theoretical distribution function is that of a slightly warmer gas compared to the measured one.

The results in Figure 5.7 show that it may be necessary to account for rotational non-equilibrium at the exit of a micro-channel, so a series of cases are performed in order to compare results obtained using the boundary conditions from Reference [87]

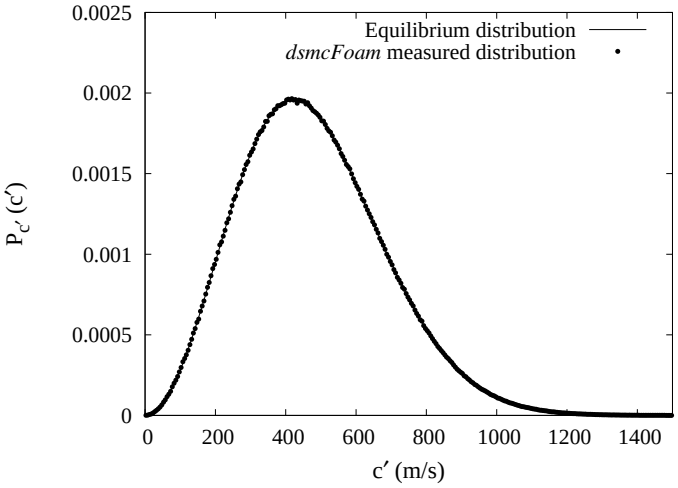

(a)

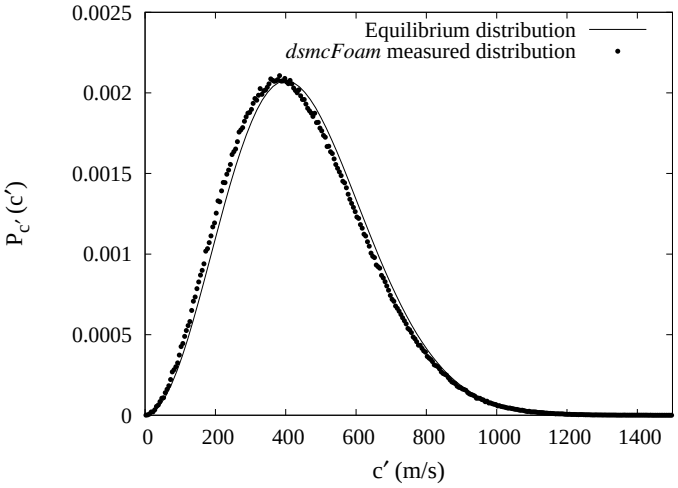

(b)

Figure 5.7: Comparison of measured and equilibrium speed distribution functions: (a) entrance measurement zone, and (b) exit measurement zone. The probability on the ordinate is defined in Equation (1.7).

Case	Length (μm)	Height (μm)	P_{in} (Pa)	P_{out} (Pa)	Boundaries
1	2	0.4	72,640	16,000	Wang & Li [87]
2	2	0.4	72,640	16,000	Current work
3	20	0.4	100,000	50,000	Wang & Li [87]
4	20	0.4	100,000	50,000	Current work

Table 5.3: Micro-channel simulation details to evaluate rotational non-equilibrium boundary conditions.

and the new boundary conditions described in §5.2. The micro-channel dimensions and inlet/outlet pressures used in each case are detailed in Table 5.3. Cases 1 and 2 were meshed with 100 × 60 computational cells, while cases 3 and 4 were meshed using 1000 × 60 computational cells. The working gas is nitrogen in all cases, where the inlet gas temperature is 300 K and all walls are fully diffuse at 300 K. All simulations use the VHS collision model with the phenomenological Larsen-Borgnakke internal energy redistribution technique.

Cases 1 and 2 were run in parallel on 2 cores each and sampled for 1 million time steps. At steady state, Case 1 had roughly 182,000 DSMC simulator particles and Case 2 had slightly more at 183,000. The total run time was around 47 hours for each case, with Case 2 being around 3% slower than Case 1. This indicates that the new outlet boundary condition proposed here does not introduce any significant computational expense with respect to that found in Reference [87].

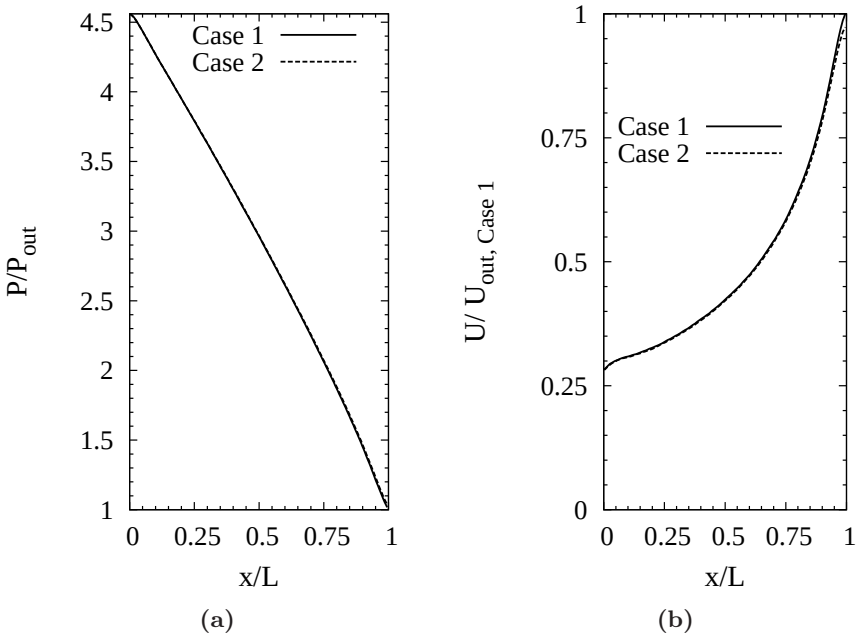

Figure 5.8: Centre-line distributions in Cases 1 and 2 of (a) normalised pressure, and (b) velocity. The velocities have been normalised with the centre-line outlet velocity from Case 1.

Figure 5.8(a) shows the centre-line pressure distributions obtained from Cases 1 and 2. In general, the pressure profiles match very well, with the new boundary conditions resulting in slightly higher pressures towards the channel exit. Figure 5.8(b) shows the

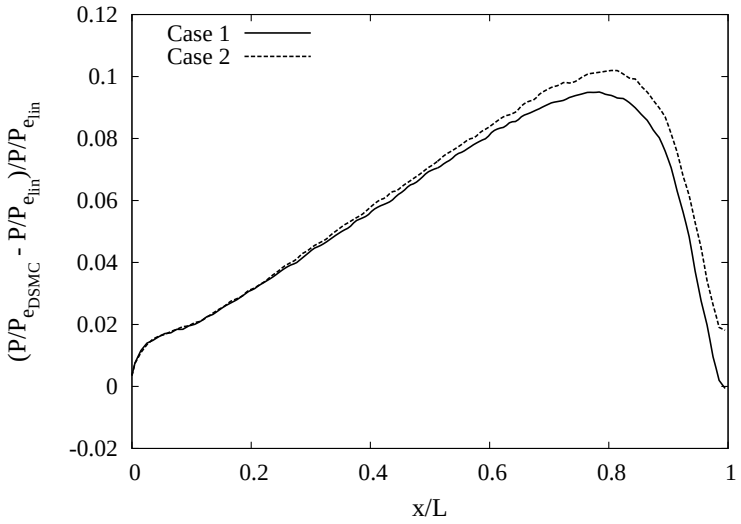

Figure 5.9: Deviation from a linear pressure profile for Cases 1 and 2.

centre-line velocity profiles from Cases 1 and 2. The velocity profiles match well until near the channel exit, where the new boundaries achieve a slightly lower value (around 6 m/s slower). Figure 5.9 shows how the pressure profile varies from that of a linear pressure drop along the length of the centre-line for both the old and new boundary conditions. There is a difference in the pressure profile towards the exit when using the new boundary conditions, because the measured pressure at the outlet is based on the translational temperature rather than the overall temperature.

The translational, rotational and overall temperature profiles at the channel centre-line in Cases 1 and 2 are shown in Figure 5.10. The translational temperature profiles match well for both boundary conditions, however the rotational temperature near the exit is increased slightly when using the newly developed boundary conditions. As a result, the overall temperature profiles match well until near the exit, and because the overall temperature is a weighted average of the three translational modes and the two rotational modes, the magnitude of the difference in overall temperature is smaller than that observed for the rotational temperatures. In order to compare with another solution, the same case was repeated using large reservoirs at the inlet and outlet as boundary conditions. This is a more realistic representation of the problem, but it is also far more computationally demanding.

The temperature profiles highlight the fact that the overall temperature can be

significantly higher than the translational temperature at the channel exit (around 15 K in these cases). This demonstrates why it is important to measure pressure using only the translational temperature, and introduce new particles based on the respective local translational and rotational temperatures, as opposed to a single value of overall temperature.

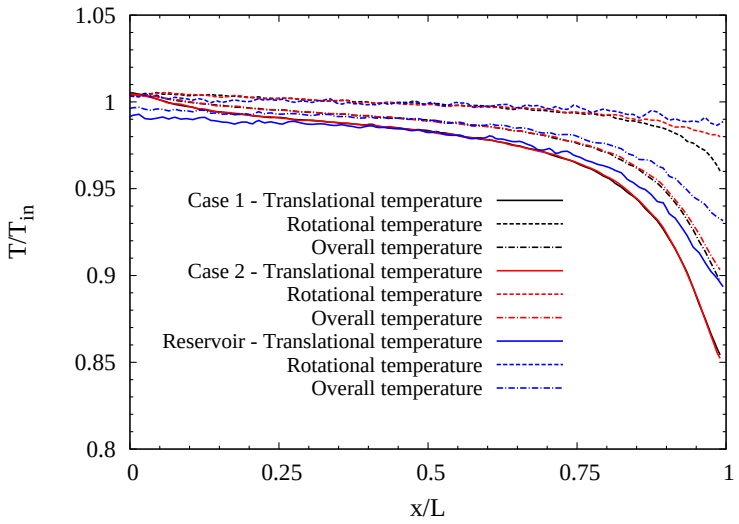

Figure 5.10: Centre-line temperature distributions for Cases 1 and 2. All of the temperatures have been normalised with the inlet gas temperature of 300 K.

The translational temperatures achieved when using both types of boundary conditions are lower than those found when using the reservoirs, but the rotational temperature achieved using the new boundary conditions is much closer to that in the reservoir, compared to the Wang & Li implementation of the boundaries. An apparent weakness of the implicit boundary conditions that this work highlights is the inability to capture the same translational temperature as the reservoir method. The reservoirs are a more realistic representation of the problem, but the implicit boundaries do have the advantage of being much more computationally efficient. For example, the reservoir case displayed here required over a week of run-time on 64 cores.

Cases 3 and 4 were run in parallel on 8 cores for a total of 2 million time steps. The domain was meshed using 1000×60 regular rectangular cells. The signal-to-noise ratio was low in these two cases because the channel is much longer and the pressure difference is also reduced with respect to Cases 1 and 2. Two million statistical samples were employed to reduce the error to an acceptable level. Using equations

from Reference [46], the estimated error in the macroscopic velocity at the channel exit centre-line is less than 1%. Both cases contained around 920,000 DSMC simulator particles at steady state.

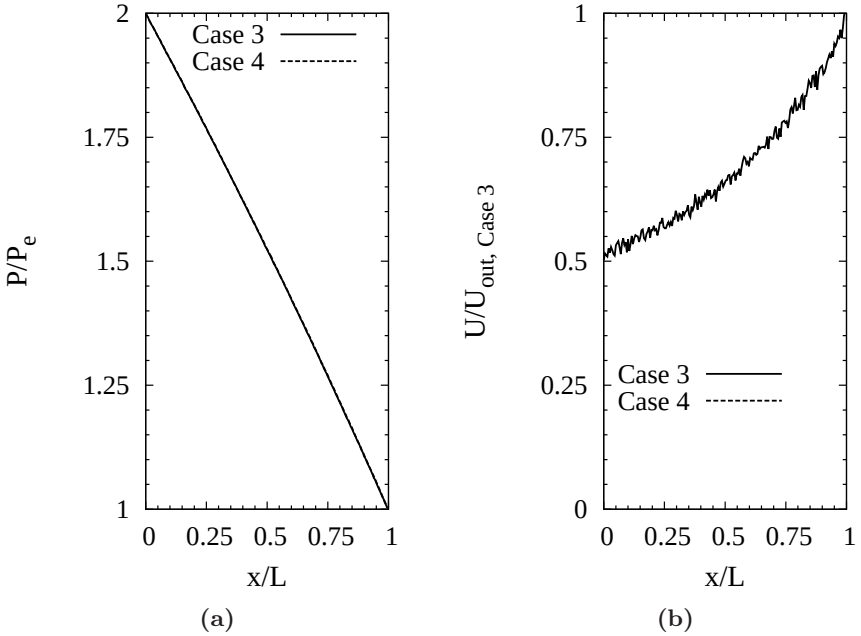

Figure 5.11: Centre-line distributions in cases 3 and 4 for (a) normalised pressure, and (b) velocity. The velocities have been normalised with the centre-line outlet velocity from Case 1.

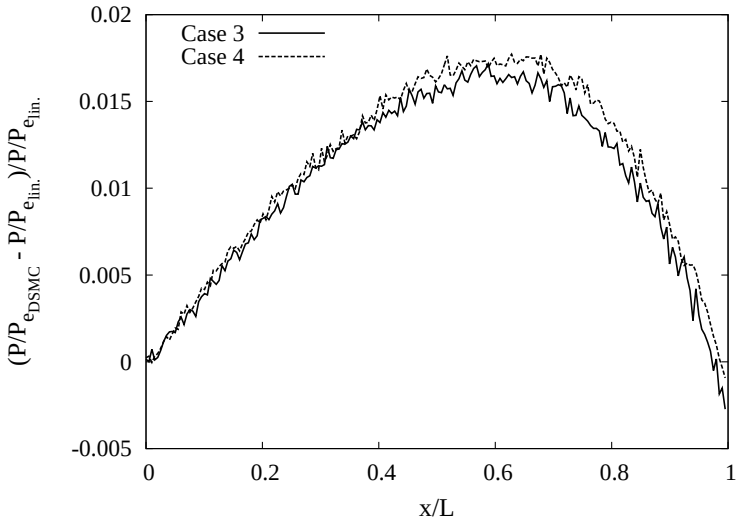

Figure 5.12: Deviation from a linear pressure profile for Cases 3 and 4.

Figure 5.11(a) shows the centre-line pressure distributions obtained from Cases 3

and 4. The pressure profiles are in excellent agreement along the whole length of the micro-channel. The centre-line streamwise velocity profiles for Cases 3 and 4 are shown in Figure 5.11(b) and good agreement is found between the two cases, although the relatively high amount of statistical scatter makes it difficult to see exactly how well these profiles match. Figure 5.12 shows how the pressure profile varies from that of a linear pressure drop along the length of the centre-line for both the old and new boundary conditions. The magnitude of the deviation from a linear profile is reduced by about an order of magnitude with respect to the results shown in Figure 5.9, and the results when using the new boundary conditions (Case 4) are in much closer agreement with those using the Wang & Li boundary conditions (Case 3).

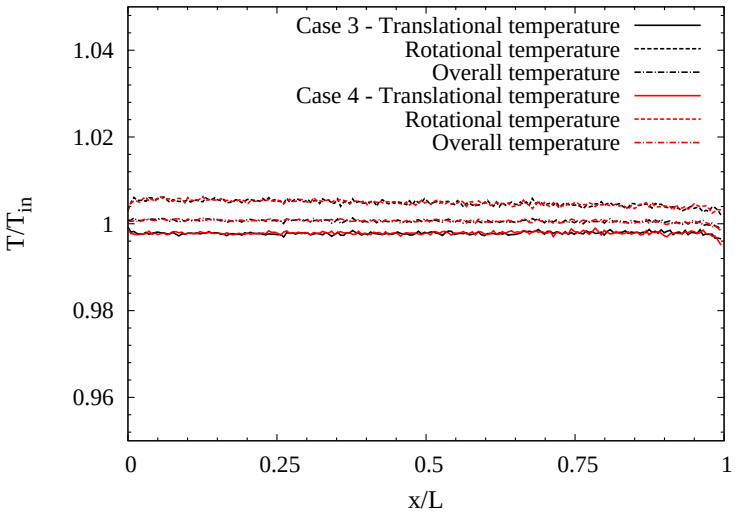

Figure 5.13: Centre-line temperature distributions for Cases 3 and 4. All of the temperatures have been normalised with the inlet gas temperature of 300 K.

Figure 5.13 shows the translational, rotational and overall temperature profiles at the channel centre-line in Cases 3 and 4: each temperature profile is in excellent agreement between Cases 3 and 4.

The results for Cases 3 and 4 are consistent with a gas which is in (or at least very close to) rotational equilibrium. This would be expected because the micro-channel length is greater than in Cases 1 and 2 and the pressure difference is also smaller. There will be fewer compressibility effects and so the gas does not expand and cool, as illustrated by the translational temperature profiles in Figure 5.13. The deviation from a linear pressure profile is also expected to be smaller when compressibility effects are

reduced, as was seen in Figure 5.12. The results from Cases 3 and 4 show that the new boundary conditions give the same results as those proposed by Wang & Li [87] when there is no, or very little, rotational non-equilibrium present in a gaseous micro-channel flow.

The inability of the implicit boundary conditions to match the translational temperature profile from the reservoir simulations is possibly due to a degree of translational non-equilibrium, and so future work on these boundaries could include measuring the temperatures from each translational degree of freedom (see Equation (1.22)), and further modifying the boundary conditions to account for translational non-equilibrium.

5.3 Micro-Channels with Bends

5.3.1 Previous Numerical Work

There has been very little numerical work concerning flows in micro-channels with bends in the slip and transition regimes, despite this being a very important area in the design of MEMS. The only work that has explicitly dealt with this kind of problem using DSMC is that by Wang & Li [87]. Here, we repeat one of their ninety-degree bend micro-channel cases, and propose some improvements on how to mesh these types of geometries in order to capture some of the surprising and significant flow features.

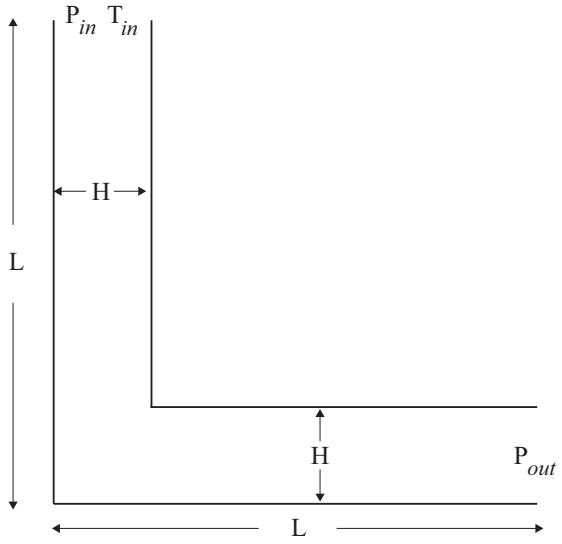

Figure 5.14: Schematic of the single ninety-degree bend micro-channel, as considered by Wang & Li [87].

The geometry is shown in Figure 5.14, where L is 5 μm and H is 1 μm. The working gas is nitrogen and the wall and inlet gas temperatures are all equal at 300 K. In Reference [87] it is stated that 100 $\times$ 100 rectangular computational cells were used to mesh the geometry. A different mesh is used in the current work: 200 $\times$ 60 rectangular cells in each arm of the channel, with 60 $\times$ 60 square cells in the corner region. This has been done to achieve a higher resolution of macroscopic properties in the corner region. The outlet pressure is 100 kPa and the inlet to outlet pressure ratio is 3. This gives Knudsen numbers ranging from 0.018 to 0.055 along the length of the micro-channel; the outlet Reynolds number was calculated as 18.18 in post-processing. The *dsmcFoam* simulation contained 1.6 million DSMC particles at steady state, and over 1 million samples were employed.

A comparison of the resulting mass density contours with velocity streamlines is shown in Figure 5.15. The values of the contours are not given in Reference [87], so it has not been possible to use the exact same values for the *dsmcFoam* results. In general though, good qualitative agreement can be found between the two cases. It is stated by Wang & Li [87] that no flow separation was found at the corner, however *dsmcFoam* has captured a region of separated flow — a close up view of this separation can be seen in Figure 5.16. Some experimental work [95] in micro-channels with bends found evidence that there may be separation zones in the corner regions. Considerable evidence of flow separation has been found in related geometries operating at similar Reynolds and Knudsen numbers, such as constriction micro-channels [96] and backward facing steps [97]. The mechanism for this flow separation is not well understood. Interestingly, the flow from our DSMC results do not exhibit the features of Stokes flow (i.e. no separation even at sharp corners) that would be expected at the low Reynolds numbers under consideration.

It is probable that the cell size used in Reference [87] is simply too large to capture the relatively small macroscopic gradients in the separation zone. Although it is possible to use elongated cell sizes in the streamwise direction of micro-channel flows because the macroscopic gradients are small [81], care must be taken when a bend is introduced to ensure that cell sizes are small enough to capture the larger gradients present in any separation zones near the corners.

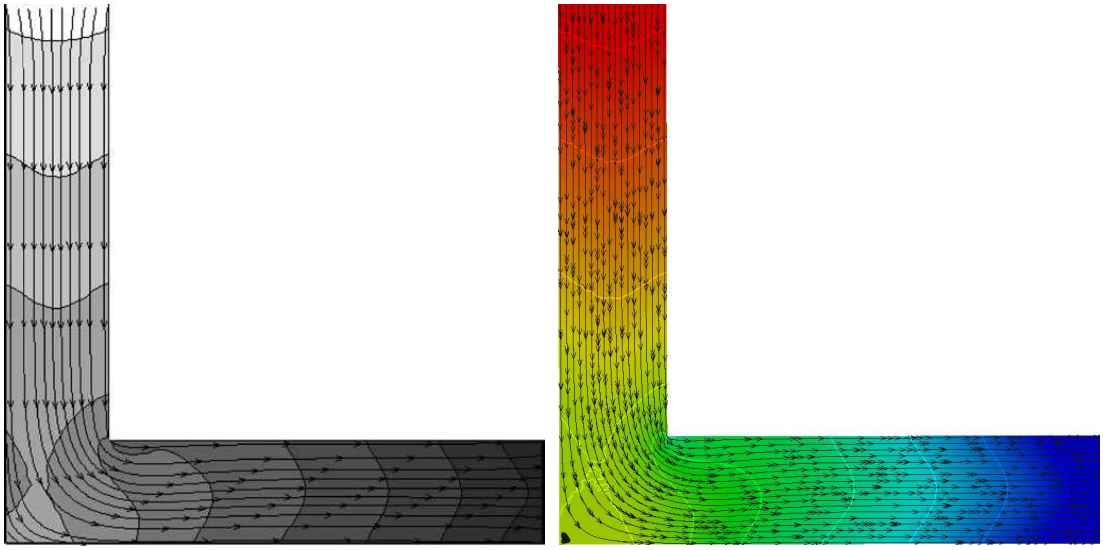

Figure 5.15: Comparison of mass density contours with velocity streamlines. Left: results of Wang & Li [87]; right: *dsmcFoam* results. Note the presence of a separated flow region in the corner region of the *dsmcFoam* results, as shown magnified Figure 5.16.

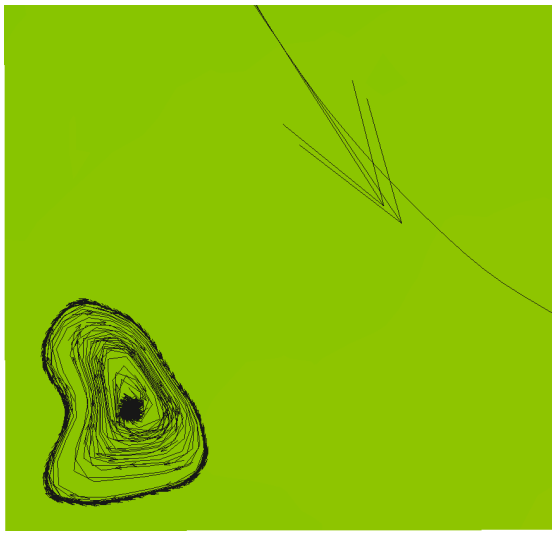

Figure 5.16: Enlarged view of the separated flow in the corner region.

The micro-channel considered here remains entirely in the slip flow Knudsen number regime, and as such this problem could have been solved with the Navier-Stokes-Fourier equations. There is no DSMC data for this kind of geometry in the transition regime, but there is some lattice Boltzmann data [98] that extends into the transition regime, achieving a maximum Knudsen number of 0.286. The geometry considered there is a micro-channel with a single ninety-degree bend and a larger aspect ratio than that of Reference [87]. Flow separation at the corners was seen in the lattice Boltzmann results,

and the size of the separation regions decreased with increasing Knudsen number.

5.3.2 DSMC Investigation of Micro-Channels with Bends

We focus on providing DSMC data in the late slip and early transition Knudsen number regimes. Micro-channel geometries with both one and two ninety-degree bends are considered and compared to an equivalent straight channel, as shown schematically in Figure 5.17. Mass flow rates are measured, and pressure and Mach number profiles along the micro-channel centre-lines are plotted for a range of Knudsen and Reynolds numbers. Each case contained approximately one million DSMC simulator particles and required one week of sampling in parallel on eight cores to achieve a sufficient number of statistical samples, i.e. in excess of one million.

	P_{in} (Pa)	P_{out} (Pa)	Time step (s)	Kn_{in}	Kn_{out}	Re_{out}	Ma_{out}
Case 1	500,000	166,666	3×10^{-12}	0.011	0.029	27.943	0.640
Case 2	200,000	66,666	6×10^{-12}	0.027	0.078	5.411	0.337
Case 3	100,000	33,333	6×10^{-12}	0.055	0.158	1.686	0.213
Case 4	61,000	20,333	6×10^{-12}	0.090	0.260	0.792	0.166
Case 5	50,000	16,666	6×10^{-12}	0.110	0.317	0.604	0.153
Case 6	18,500	6,166	6×10^{-12}	0.300	0.862	0.176	0.122

Table 5.4: DSMC micro-channel simulation case details.

Table 5.4 details the inlet and outlet pressures for each case considered, along with values for the time step, and the Knudsen, Reynolds and Mach numbers at the inlet ("*in*") and outlet ("*out*"). The working gas is argon, set at 300 K at the inlet for all cases. All walls are modelled as fully diffuse boundaries at 300 K. The cases cover a range of situations: Cases 1 and 2 are completely in the slip regime, in Cases 3 and 4 the inlet flow is the slip regime and the outlet flow is in the transition regime, and Cases 5 and 6 are entirely in the transition regime. A slightly smaller time step has been used for the case at the highest pressure to ensure that the time step remained much smaller than the mean collision time. The values of Kn_{out}, Re_{out} and Ma_{out} were calculated during post-processing at the exit centre-line; Kn_{out} was calculated using the local temperature and density with the VHS mean free path, and Re_{out} and Ma_{out}

are calculated using the following formulations:

$$Re_{out} = \frac{U_{out}\rho_{out}H}{\mu_{out}}, \tag{5.12}$$

and

$$Ma_{out} = \frac{U_{out}}{\sqrt{\gamma RT_{out}}}, \tag{5.13}$$

where γ is the ratio of specific heats and μ is the local gas viscosity calculated from a viscosity power law with the VHS ω parameter as the exponent. Figure 5.17 is a diagram of the three geometries considered here, where L is 15 μm and H is 1 μm. The total flow length was maintained constant for all three geometries to ensure a fair comparison could be made between the different geometries. It should be noted that all of the current cases are two-dimensional, effectively representing a cross-section of a wide micro-channel.

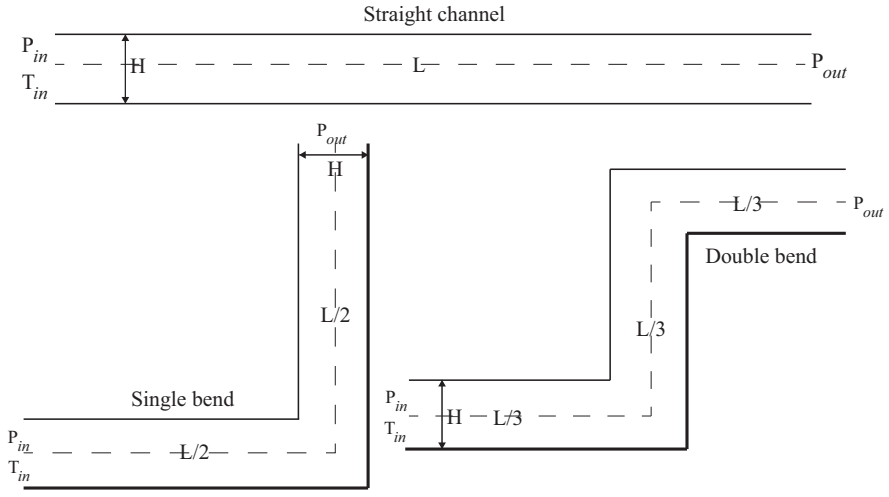

Figure 5.17: Schematics of the three different micro-channel geometries considered. The thicker lines on the single and double bend channels represent the "lower walls" and the thinner lines are the "upper walls"; $L = 15$ μm, $H = 1$ μm.

The normalised centre-line pressure distributions for the six cases are shown in Figure 5.18. In Figure 5.18(a), the profiles in the straight micro-channel geometries are presented. As expected, non-linear pressure profiles have been found, and the degree of non-linearity decreases with increasing Knudsen number as rarefaction effects (Kn) begin to dominate the compressibility effects (Ma).

Figure 5.18(b) shows the normalised pressure profiles for the channel with a single

ninety-degree bend. The pressure profiles differ from the straight channel by having noticeable jumps in local pressure at the bend location. These jumps are compressibility effects, which are introduced by a reduction of the gas velocity in the flow direction, due to the abrupt changes in channel geometry. For cases of lower Mach number, however, the compressibility effects are less, and proportionally so are the pressure jumps at the bend locations. Figure 5.18(c) shows very similar behaviour for a micro-channel with two ninety-degree bends, but instead there are two pressure peaks. This analysis is further verified by the Mach number plots shown in Figure 5.19; local Mach number decreases significantly at bend locations.

It is clear that the pressure and Mach number profiles for all 3 geometries are very similar outside of the bend regions and this suggests that there are no significant pressure losses introduced by the inclusion of a bend, and consequently similar mass flow rates should be expected. Indeed, lattice Boltzmann results in Reference [98] indicate that the presence of a bend may result in a modest increase in the mass-carrying capacity of a micro-channel.

To investigate this phenomenon using DSMC, we plot the mass flow rates in Figure 5.20 for the single bend and double bend micro-channel geometries. Each of the data points has been normalised with the mass flow rate in the corresponding straight micro-channel. The measured error in all of the mass flow rate values is less than 0.5%, based on the standard error from the standard deviation of the instantaneous samples. The error bars associated with the data points are much smaller than the plotted points and have therefore been omitted. We define the percentage flow enhancement, ϵ, as

$$\epsilon = 100 \left[\frac{(\dot{m}_{bend} - \dot{m}_{straight})}{\dot{m}_{straight}} \right], \tag{5.14}$$

where $\dot{m}_{bend}$ is the mass flow rate from the bent channel simulation and $\dot{m}_{straight}$ is the mass flow rate from the corresponding straight channel.

In agreement with lattice Boltzmann [98] and continuum [99] results, we find a relative increase of up to 1% in the amount of mass that a channel with a single bend can carry when $0.02 \leq Kn_{in} \leq 0.08$. For the micro-channels with two ninety-degree bends, a 1.7% flow enhancement is observed, and roughly in the same range of Knudsen numbers. For the other Knudsen numbers considered in this work there is a negative

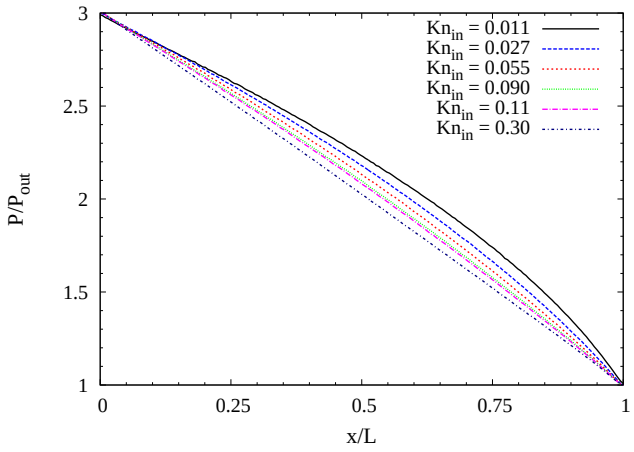

(a)

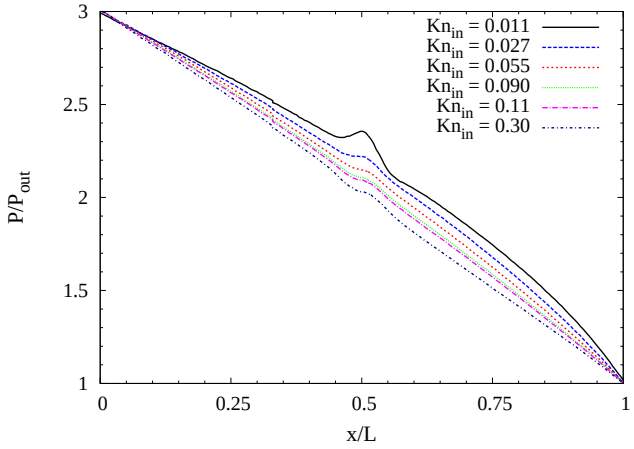

(b)

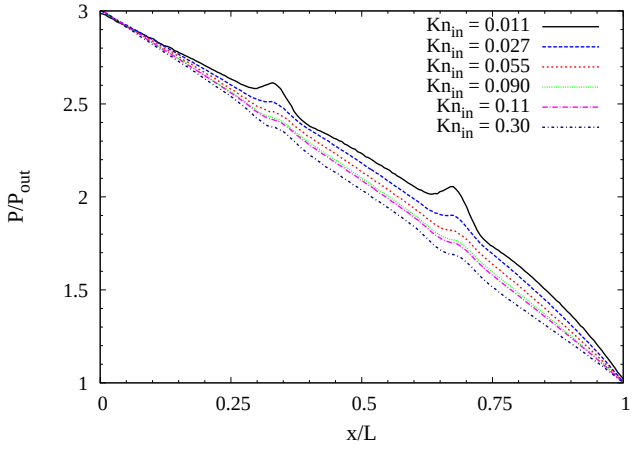

(c)

Figure 5.18: Streamwise centre-line pressure profiles; (a) straight channel, (b) channel with single bend, and (c) channel with two bends.

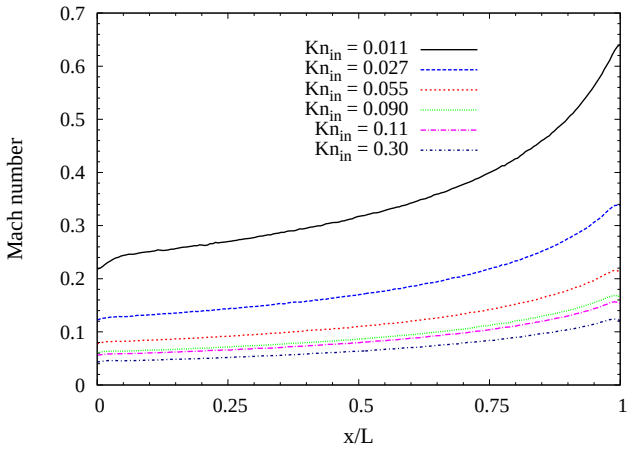

(a)

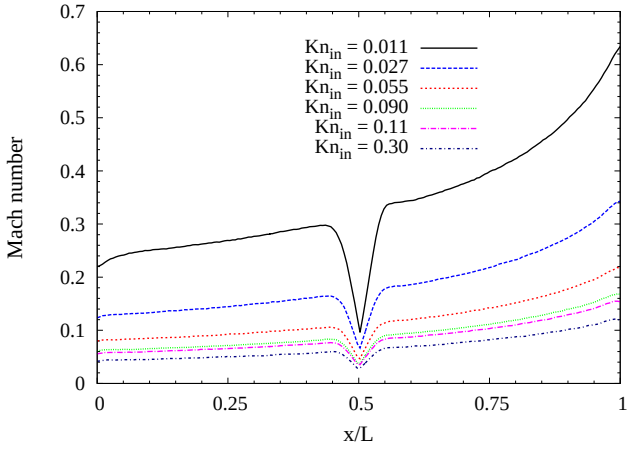

(b)

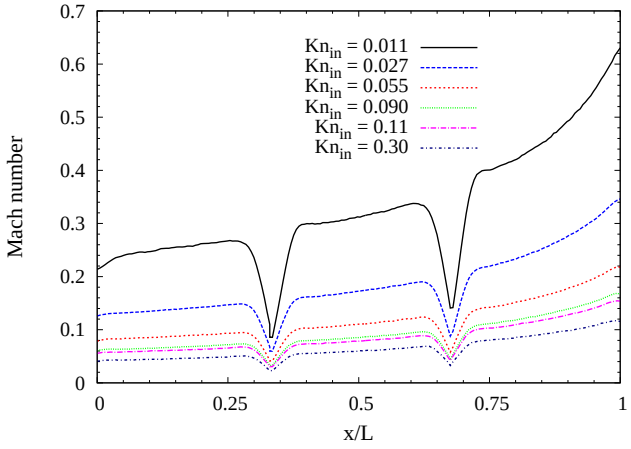

(c)

Figure 5.19: Streamwise centre-line Mach number profiles; (a) straight channel, (b) channel with single bend, and (c) channel with two bends.

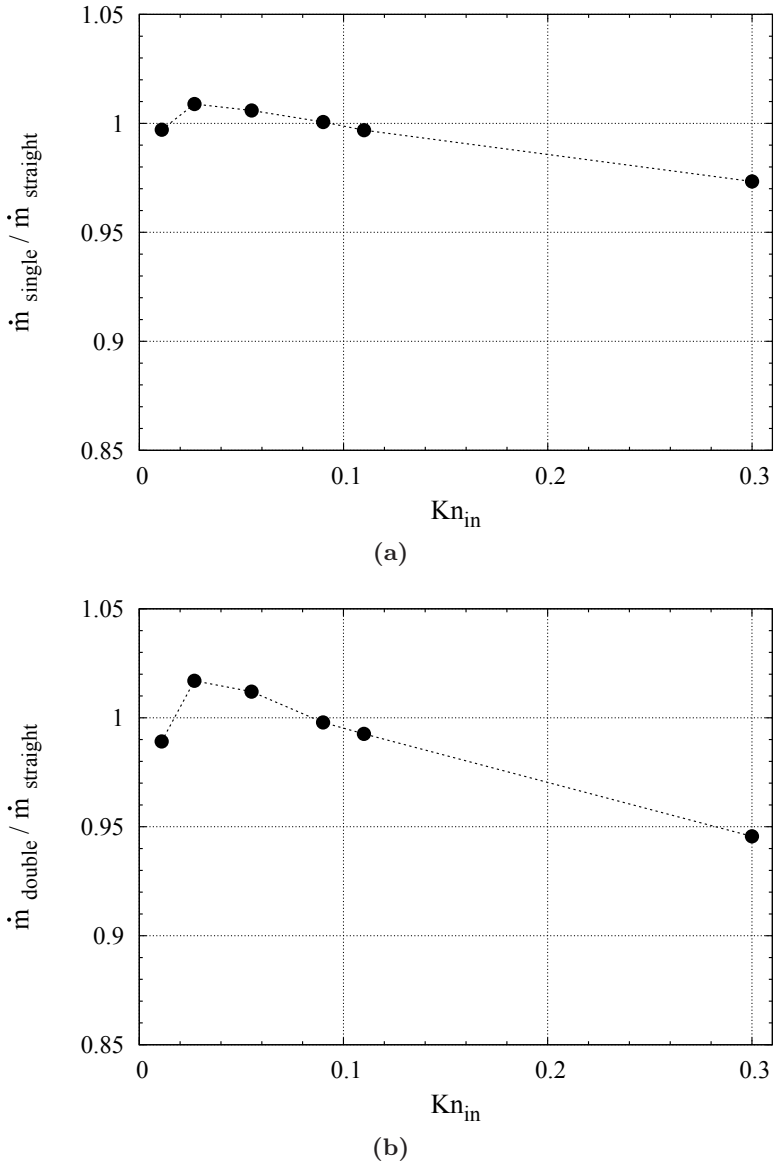

Figure 5.20: Mass flow rate measurements in micro-channels; (a) single bend, and (b) two bends. Values of mass flow rate are normalised by the mass flow rate in the corresponding straight channel.

flow enhancement for both types of bent channels when compared to the corresponding straight channel cases. For example, at $Kn_{in} = 0.3$, a 3% decrease in mass flow rate is found for the single bend, and a 6% decrease for the double bend channel.

Table 5.5 shows the DSMC results for the average shear stress $\overline{\tau}$ at both channel walls for a double bend, normalised with the average shear stress at the walls of the equivalent straight channel. The double bend results have been chosen here because the wall lengths are equal to that of the straight channel case and a fair comparison can

	$\overline{\tau}$ / $\overline{\tau}_{straight}$	
Kn_{in}	Upper wall	Lower wall
0.011	0.7650	0.7484
0.027	0.8157	0.7898
0.055	0.8198	0.7932
0.09	0.8110	0.7872
0.11	0.8069	0.7854
0.30	0.7752	0.7652

Table 5.5: Average shear stresses at the wall in the micro-channels with two bends, relative to those in the straight channel.

therefore be made. The shear stress was calculated from the pre- and post-interaction components of particle momentum tangential to the surface, as described in Reference [86]. It is found that the inclusion of bends in a micro-channel always reduces the average shear stress at the walls for the current cases. In systems where a positive mass flow rate enhancement is found ($Kn_{in} = 0.027$ and 0.055) the shear stress ratios are closer to unity for both the upper and lower walls than those in which a decrease is found.

Figure 5.21 shows the normalised values of shear stress and velocity slip at the upper and lower walls of the micro-channel with two bends at $Kn_{in} = 0.027$, the Knudsen number where the largest mass flow rate enhancement has been found. The results from the equivalent straight channel have also been plotted for reference. The double bend channel has been chosen for comparison again because, unlike the channel with a single bend, the total wall lengths are equal to those in a straight channel and this allows for a fair comparison. The shear stress and velocity slip profiles follow very similar patterns to one another. It is clear that most of the roughly 20% reduction in average shear stress in the channel with bends comes at the outside of the bends, i.e the first bend for the lower wall, and the second bend for the upper wall. There is a small decrease in shear stress after the inside of a bend, but this is offset by a small increase immediately prior to the bend. The decrease in shear stress in regions of lower slip velocity is expected from Maxwell's velocity slip relation, since $|\vec{u}_{slip}| \propto |\vec{\tau}|$ [2, 100].

Figure 5.22 shows the differences between the centre-line pressure profiles along micro-channels with a single bend and a double bend, with respect to the equivalent straight micro-channels. Here, different behaviour can be observed at the Knudsen

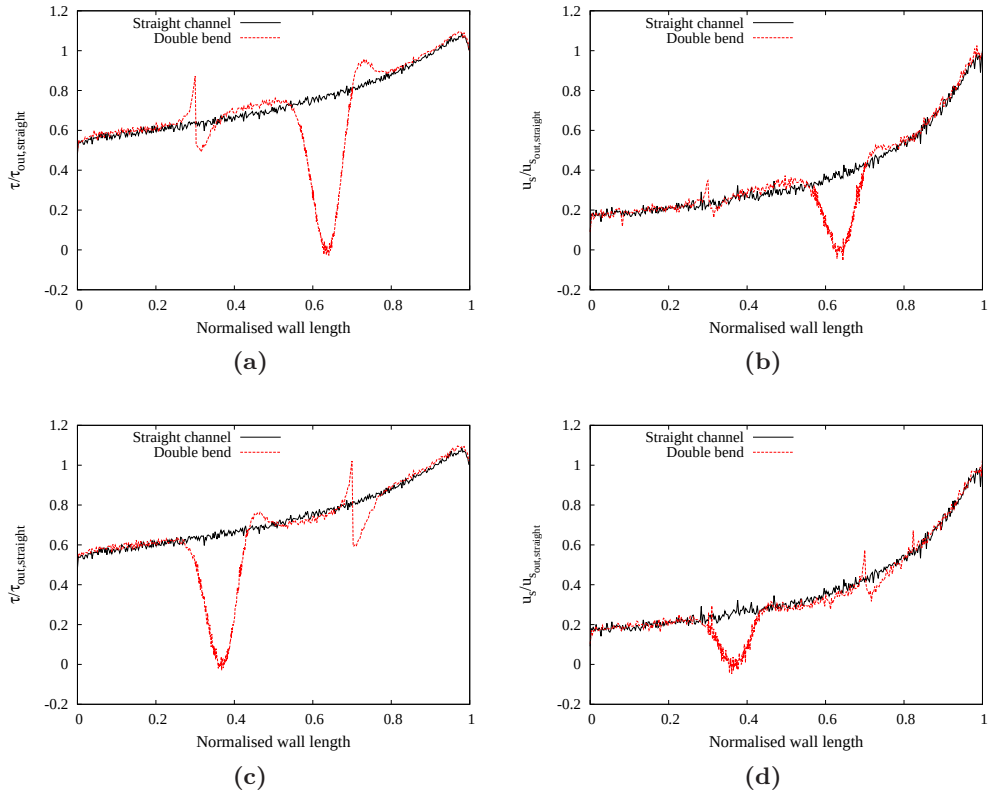

Figure 5.21: Results for the $Kn_{in} = 0.027$ case: (a) shear stress at the upper wall, (b) slip velocity at the upper wall,(c) shear stress at the lower wall, and (d) slip velocity at the lower wall. All of the shear stresses have been normalised with the shear stress at the exit of the straight channel, and the slip velocities with the slip velocity at the exit of the straight channel.

numbers where the positive and negative flow enhancements are found: for a micro-channel with a single bend, at the two Knudsen numbers where a small increase is observed ($Kn_{in} = 0.027$ and 0.055), the pressure difference from a straight micro-channel is negative before the bend and positive after it. At an inlet Knudsen number of 0.3, the opposite behaviour is found, i.e. positive difference before the bend and negative after it. For the remaining two Knudsen numbers where the mass flow rate is nearly the same as in the straight channel, there is very little difference in the pressure profiles outside of the bend region. Similar patterns are found for a micro-channel with two bends, with some different behaviour being evident in the length between the two bends.

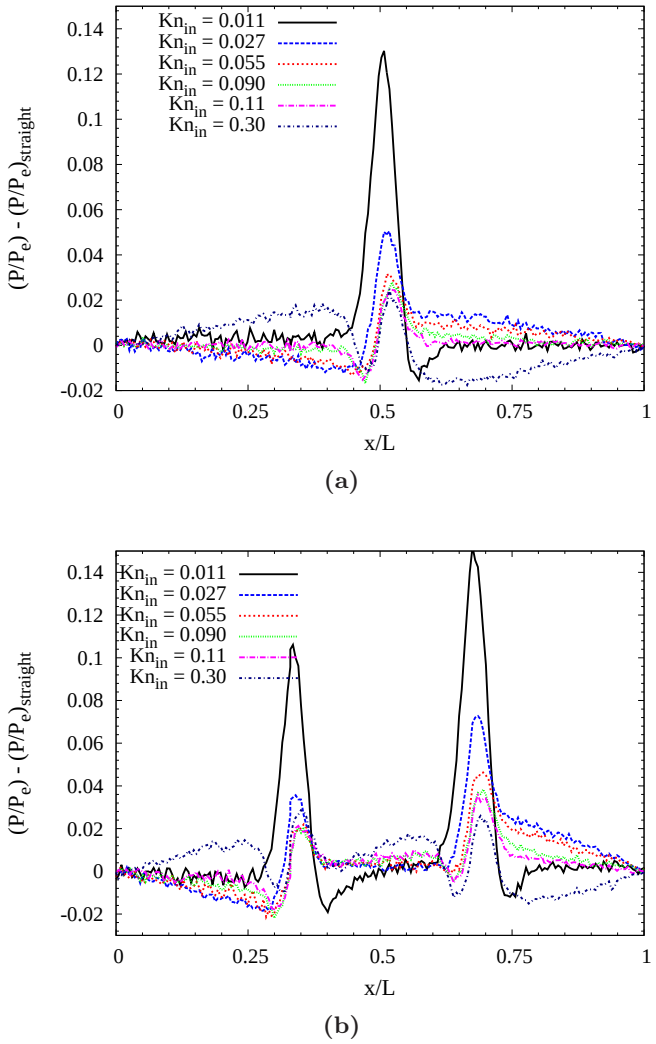

Figure 5.22: Differences from normalised straight-channel streamwise pressure profiles along the centre-line for (a) single bend channel, and (b) double bend channel.

5.4 Cylindrical Couette Flow

A canonical non-planar flow test case is the isothermal rarefied gas flow between two concentric rotating cylinders, as shown schematically in Figure 5.23. This is a classical fluid dynamics problem that is covered for the no-slip case extensively in the literature. However, under certain conditions, the flow between the cylinders can exhibit highly non-intuitive behaviour. For example, if the outer cylinder is stationary and the inner cylinder is rotating, it is possible for the velocity profile to become inverted, i.e. the velocity will increase from the inner to the outer cylinder wall. This unusual phenomenon was first predicted by Einzel *et al.* [101] for the case of liquid helium. Tibbs *et al.* [102]

extended the analysis to the case of a rarefied gas and, using DSMC, demonstrated that velocity inversion could occur provided the accommodation coefficient for the surfaces was small. This early work has led to a number of important curvature studies for rotating Couette flow [100, 103–105].

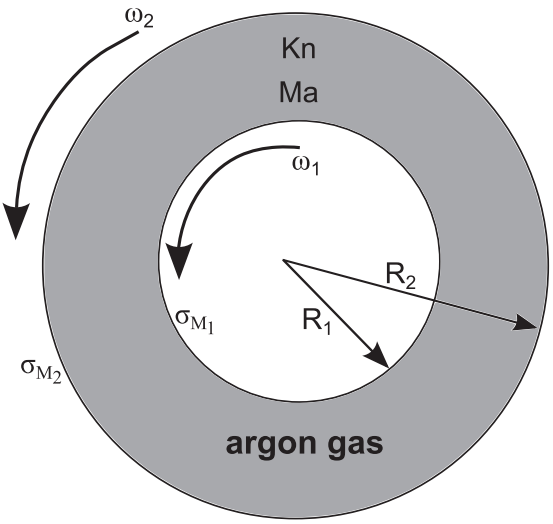

Figure 5.23: Schematic of the geometry used for the study of cylindrical Couette flow.

Existing simulations [102, 106] do not cover a wide range of Knudsen numbers, and they are also carried out for limited number of ratios of the outer (R_2) to inner (R_1) cylinder radii. Tibbs *et al.* [102] performed DSMC simulations for a Knudsen number of 0.5, based on the hard sphere mean free path and the gap between the cylinders, with $R_2/R_1 = 5/3$, while Kim's [106] MD numerical experiments were conducted for $Kn \simeq 0.01$, with $R_2/R_1 = 5$. Although Jung [107] has carried out MD simulations for various radii ratios, their R_2/R_1 values are quite large ($\gg 5$) and so the rotating inner cylinder may not have a significant influence on the velocity profile results. On the other hand, curvature effects are more pronounced at higher Kn. There is also no published torque data for the rarefied rotating Couette flow test case. The existing experimental data can be traced back to Kuhlthau [108]; however, that experimental set-up consisted of an inner cylinder with length comparable to its radius. It has been mentioned by Agrawal & Prabhu [109] that this makes it necessary to incorporate a correction factor to match the classical theories even in the continuum regime.

In view of the above, we carry out DSMC simulations for Knudsen numbers covering the slip ($Kn = 0.1$) and transition flow regime ($Kn = 0.5$ and 1). At each Kn a variety

of accommodation coefficients (σ_M) and R_2/R_1 values are used to check the sensitivity of surface and curvature effects, respectively. The resultant torque data is compared with classical slip theory.

For all of the DSMC simulations here, the cell size is chosen to be smaller than the mean free path, and so that enough cells are placed throughout the domain to recover macroscopic properties with sufficient resolution. The Knudsen number is based on the unconfined mean free path and the radial distance between the cylinder surfaces ($R_2 - R_1$). The time step is smaller than the mean collision time and also small enough that particles are likely to spend multiple time steps within a single computational cell. All simulations are initialised with at least 20 DSMC simulator particles per cell, with 500,000 particles in the whole domain. Each case was solved in parallel on 4 cores on the HPC facility at the University of Strathclyde. The physical run time for each case was around 60 hours to simulate 9 μs of problem time. Due to the low signal-to-noise ratio expected in these simulations, one million statistical samples are employed for each case. The VHS collision model is used to perform collisions and all gas-surface interactions are dealt with as a mixture of specular and Maxwellian diffuse interactions in order to simulate various surface accommodation values. The torque on the rotating cylinder is calculated from the viscous drag force acting on the cylinder surface. In the current analysis, we fix the accommodation coefficient of each cylinder to be the same, but it has been shown [104] that the velocity inversion phenomenon only depends on the accommodation coefficient of the outer cylinder.

Numerical results are obtained for a variety of outer-to-inner cylinder radius ratios (R_2/R_1 = 6/5, 5/3, 2, 3 and 5), Knudsen numbers (Kn = 0.1, 0.5 and 1.0) and accommodation coefficients (σ_M = 0.1, 0.4, 0.7 and 1.0). The accommodation coefficient is always equal for both surfaces in our case, but it has been shown that it is only the accommodation coefficient of the outer cylinder that is important in the prediction of an inverted velocity profile [104]. The inner cylinder is rotating at a Mach number ($Ma = R_1\omega_1/\sqrt{\gamma RT}$) of 0.2. The surface temperature of both cylinders is constant at 273 K. The radii ratio is varied by fixing R_1 and increasing R_2 , and Kn is set by proportionally modifying the gas density. As the Mach number is fixed, the Reynolds number (Re) remains constant for different geometric configurations, as long as Kn is

the same.

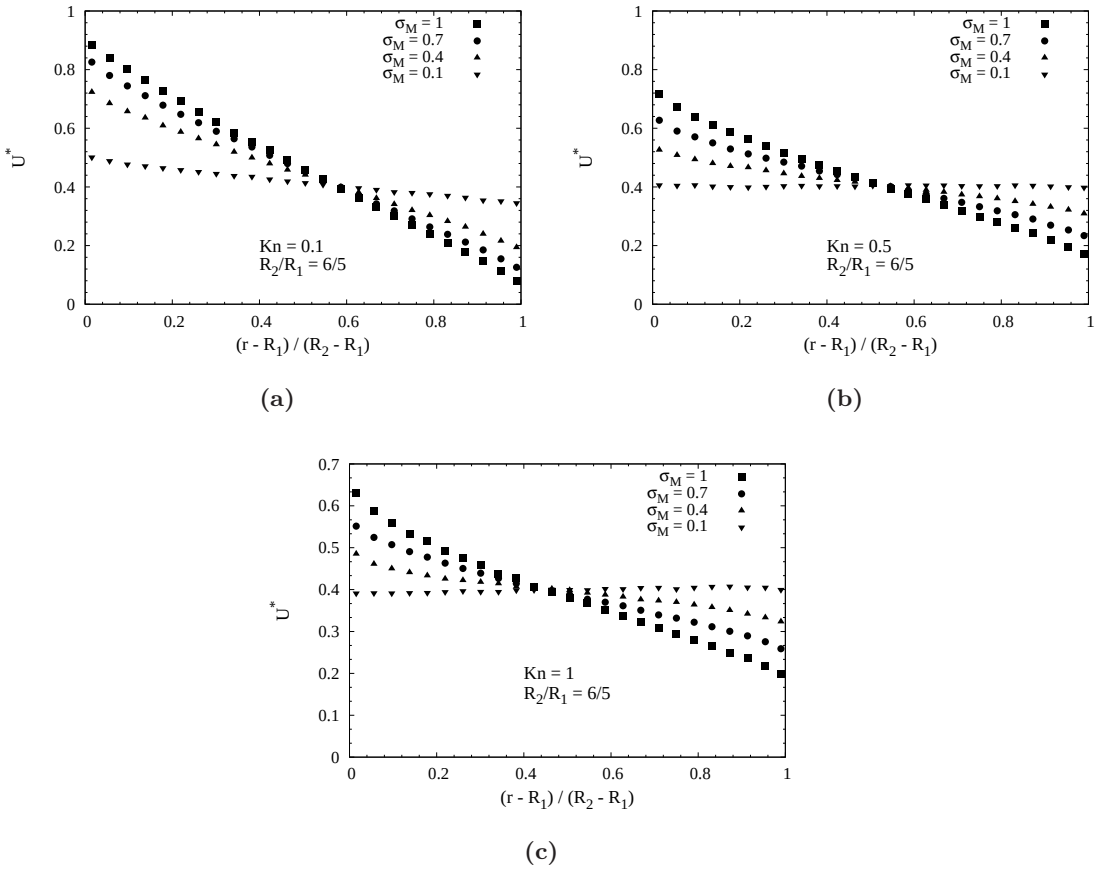

Figure 5.24: Radial velocity profiles normalised by the velocity of the rotating inner cylinder for $R_2/R_1 = 6/5$: (a) $Kn = 0.1$, (b) $Kn = 0.5$, and (c) $Kn = 1$.

Figure 5.24 shows the radial velocity profiles normalised by the velocity of the rotating inner cylinder for $R_2/R_1 = 6/5$, for the three different Knudsen numbers. This shows the effect of rarefaction and accommodation coefficient on the velocity profiles. As would be expected, as the degree of rarefaction increases, the magnitude of velocity slip increases as non-equilibrium effects become more pronounced. No velocity inversion is found at the lowest Knudsen number, even for the smallest accommodation coefficient. At the two higher Knudsen numbers our DSMC results do predict inverted velocity profiles only for the lowest accommodation coefficient considered. An interesting feature at each Knudsen number is the point where the family of velocity profiles cross over one another. As rarefaction increases, this point moves closer to the inner cylinder.

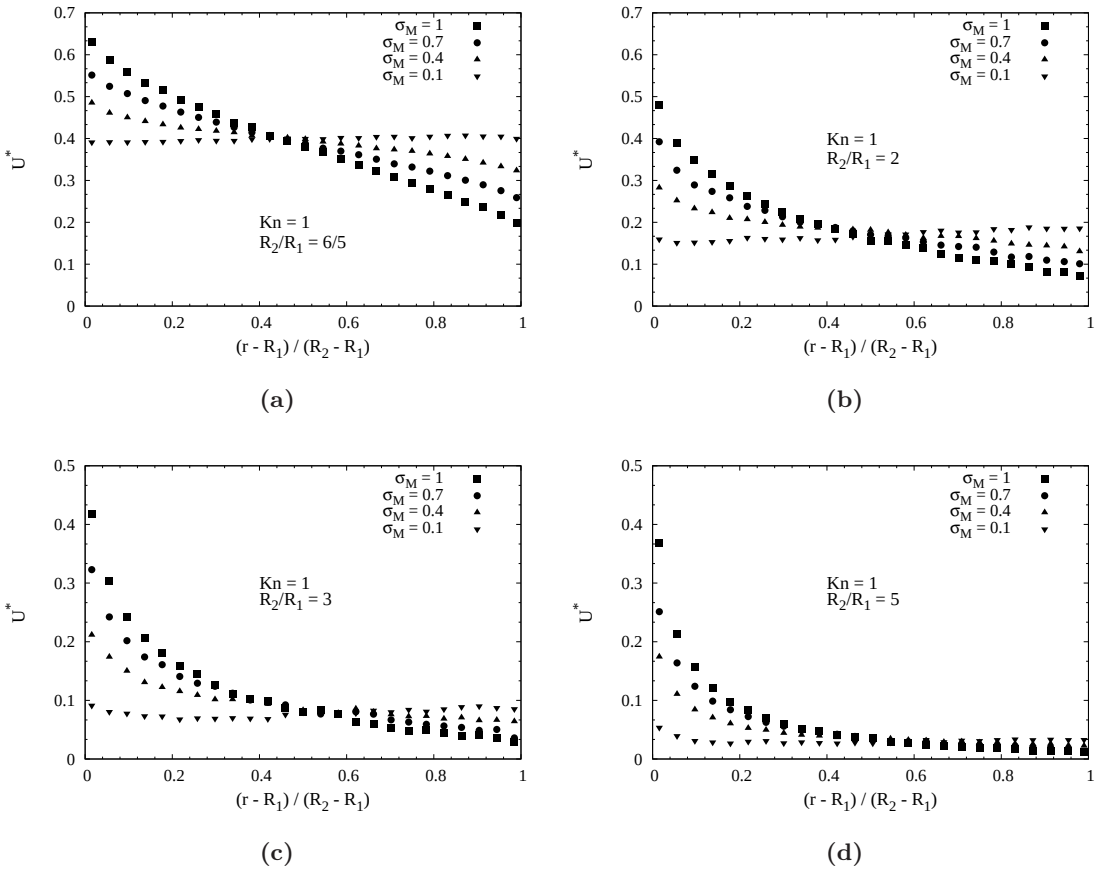

Figure 5.25: Radial velocity profiles normalised by the velocity of the rotating inner cylinder for $Kn = 1$: (a) $R_2/R_1 = 6/5$, (b) $R_2/R_1 = 2$, (c) $R_2/R_1 = 3$, and (d) $R_2/R_1 = 5$.

In order to study the effect of changing curvature and accommodation coefficient on the velocity profiles, Figure 5.25 shows the velocity profiles for a Knudsen number of 1, but different radii of the outer to inner cylinders. Inverted velocity profiles are found for $R_2/R_1 = 6/5$ and 2 at the lowest accommodation coefficient; however, only partially inverted velocity profiles are found for $R_2/R_1 = 3$ and 5. As the R_2/R_1 value increases, the velocities at the outer cylinders become progressively less dependent on the accommodation coefficient; they are all tending towards a constant value near zero velocity. As the outer cylinder radius increases it is becoming closer to a planar geometry and so the gas molecules are not as affected by the curvature at this surface. Conversely, at the inner cylinder, the curvature increases with R_2/R_1, and this causes an increase in non-equilibrium effects characterised by the increasing magnitude of slip velocity. Unlike the case where the rarefaction is modified, the point where the family of

velocity profiles cross over one another is relatively insensitive to changes in curvature through alteration of the R_2/R_1 value.

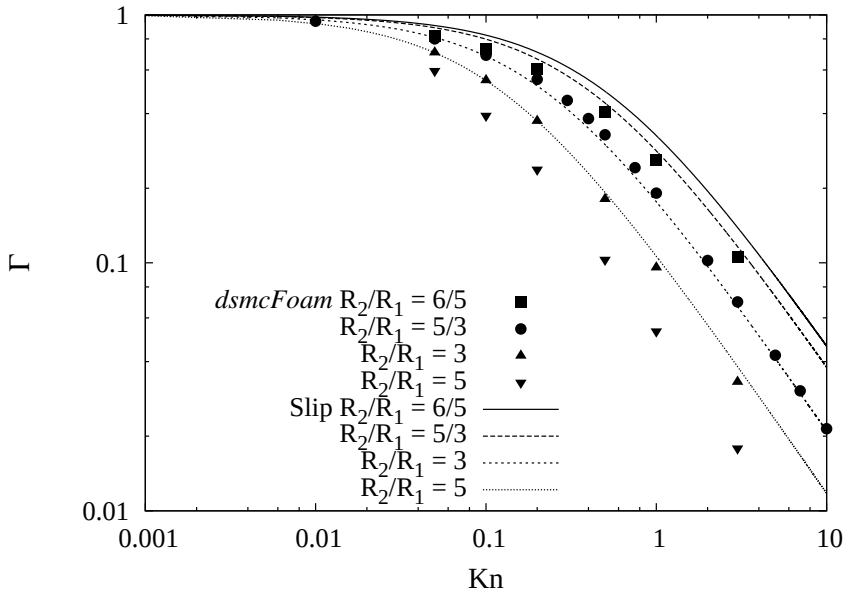

Figure 5.26: Torque normalised by the continuum value Γ against Kn for different values of R_2/R_1, for the cases where $\sigma_{M_1} = \sigma_{M_2} = 1$.

Torque values normalised by the continuum value Γ at the inner cylinder are shown in Figure 5.26 for various Knudsen numbers and $R_2/R_1 = 6/5$, 5/3, 3, and 5, when the accommodation coefficient of both cylinders is unity. The continuum value of torque T_c is calculated as:

$$T_c = \frac{8\pi^2\omega_1\mu R_1}{\frac{1}{R_1^2} - \frac{1}{R_2^2}}, \tag{5.15}$$

where ω_1 is the angular velocity of the inner cylinder and μ is the viscosity of the gas calculated from a power law model using the VHS viscosity exponent. The torques are normalised with the continuum value in order to quantify the degree of non-equilibrium in each value. The values predicted by the continuum fluid model with slip boundary conditions T_s are also plotted for comparison, and have been calculated as [109]:

$$T_s = \frac{8\pi^2\omega_1\mu R_1}{\left[\left(\frac{1}{R_1^2}\right)\left(1 + \frac{2\lambda}{R_1}\right)\right] - \left[\left(\frac{1}{R_2^2}\right)\left(1 - \frac{2\lambda}{R_2}\right)\right]}, \tag{5.16}$$

where λ is the unconfined mean free path of the gas. Clearly, an increase in R_2/R_1 results in a decrease in the torque (because of an increase in non-equilibrium effects) at

the inner cylinder; as does an increase in Kn at constant R_2/R_1. None of the slip model torque values are in good agreement with our DSMC results; however, at constant Kn and constant Ma (i.e. fixed Re) it is clear that the deviations are less significant at smaller values of R_2/R_1. This, in conjunction with the results from Figure 5.25 shows that the non-equilibrium effects are not merely dependent on rarefaction, they are also influenced by curvature.

5.5 Summary

The implementation of sub-sonic, implicit pressure boundary conditions in DSMC simulations has been undertaken within *dsmcFoam* and benchmarked against numerical and analytical solutions. We have identified a weakness in these boundary conditions, and proposed an extension to them that accounts for rotational non-equilibrium at the exit. Our results using this new outlet boundary condition are promising, but future work should consider also taking translational non-equilibrium into account to try and match the translational temperature profiles from the simulations with explicit gas reservoirs.

Micro-channels with bends have been considered and we have shown that *dsmcFoam* finds separation at the outside of a sharp bend, even for very low Reynolds number. Micro-channel geometries with one and two sharp ninety-degree bends in the late slip and transition regimes have been simulated. For the range of Kn, Ma and Re we have tested, it is found that the inclusion of a sharp bend in a micro-channel geometry does not introduce any significant losses on top of those in a straight micro-channel. In fact, a modest mass flow rate enhancement can be achieved in a small range of Knudsen number. This mass flow rate enhancement has been found previously with continuum and lattice Boltzmann solvers, but has been found here for the first time using DSMC. Shear stress and slip velocity profiles have been plotted for the Knudsen number where the largest mass flow rate enhancement is predicted.

The problem of rarefied micro-scale cylindrical Couette flow has been considered, and the effects of curvature, rarefaction and surface properties have been investigated using *dsmcFoam*. We find that increasing the outer-to-inner radius ratio leads to increased non-equilibrium effects near the inner cylinder even when the rarefaction (Kn)

and compressibility (Ma) is maintained constant, and that the behaviour near the outer cylinder surface tends towards that of a planar geometry as the ratio is increased. Torque values at the inner cylinder surface have been presented for the first time, and they also show that non-equilibrium effects are dependent on both rarefaction and curvature effects.

Chapter 6

SpaceChip Applications

Poyekhali [Let's go]!

- Yuri A. Gagarin

In the previous chapter we used *dsmcFoam* to investigate low speed flows in micro-scale geometries. One strength of the DSMC method is how wide its range of applicability has proved to be. Here, we demonstrate this through investigation of rarefied gas effects on high area-to-mass spacecraft in low Earth orbit. Recent advances in miniaturisation enable the fabrication of such spacecraft, with sensing, computing and communication capabilities down to the dimensions of a single microchip. These are so-called "satellites-on-a-chip" or "SpaceChips" [110], and an example of one is shown in Figure 6.1.

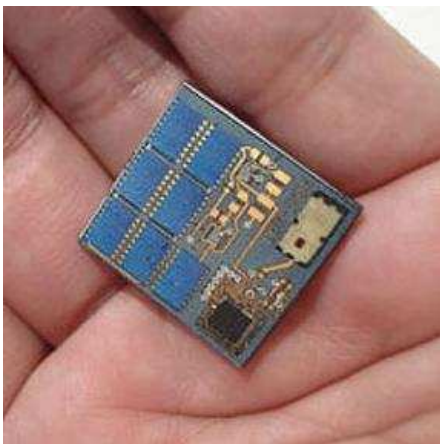

Figure 6.1: Photograph of a SpaceChip produced at Cornell University. Image credit: http://www.spaceref.com/news/viewpr.html?pid=33438.

Miniaturisation reduces production, launch and deployment costs, hence vast numbers of 'smart dust' devices can be fabricated for use in swarm applications [111, 112]. Increased launch opportunities and low manufacturing costs reduce the total mission cost. For this reason the use of SpaceChips can accept higher risk in investigating new phenomena or exploring the harsh space environment. Their fundamental payload and power limitations mean that they are ideally suited for distributed sensor networks with separations of less than one kilometre. SpaceChips are cost-effective and mass-producible, and would most usefully carry out brief, but novel, distributed sensing missions in low-Earth orbit.

A high surface-area-to-mass ratio A/m is typical of these miniature spacecraft. As mass scales with length as L^3, while surface area scales as L^2, the effective areal density scales as L^{-1} with diminishing spacecraft size. For high area-to-mass spacecraft, surface perturbations, such as solar radiation pressure (SRP) and atmospheric drag, are therefore no longer negligible. For example, solar radiation pressure was found to reduce the perigee of the ECHO balloon satellite by 44 km in the first 12 days of its mission [113]. But rather than being counteracted, they could instead be exploited to generate new families of highly perturbed non-Keplerian orbits and potentially new mission applications [114]. The SpaceChip considered in this chapter has dimensions of 1 cm $\times$ 1 cm $\times$ 25 μm [115], and an area-to-mass ratio of 17.39 m^2/kg. Figure 6.2 is an example of how the acceleration due to atmospheric drag changes with area-to-mass ratio of four different spacecraft: LAGEOS [116], a CubeSat [117], ECHO [113], and a SpaceChip [115]. For the purposes of this example, it has been assumed that each spacecraft is orbiting at 600 km, and it is clear that the acceleration due to drag is significantly more important for the higher area-to-mass ratio satellites (the ECHO balloon and a SpaceChip).

A SpaceChip is usually considered to operate isothermally [110, 115]. Here we assume that this is not the case; in fact, if there is a temperature gradient across the shortest side of the SpaceChip it may experience forces akin to those generated in a Crookes radiometer [57]. Objects in the exosphere can have a significant temperature difference across them: the Sun-facing side can be at a significantly higher temperature than the shaded side. Although SpaceChips are thin and would reach an equilibrated

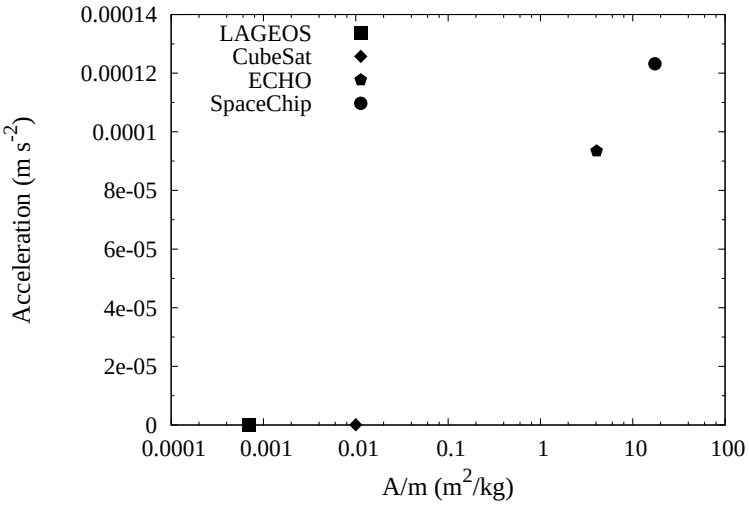

Figure 6.2: Variation of acceleration due to atmospheric drag with area-to-mass ratio A/m for a spacecraft at 600 km altitude.

temperature quickly [110], insulating layers and heater plates could be implemented to maintain a temperature gradient across them. Gas molecule-surface interactions are highly influenced by the surface temperature, particularly in the transition and free-molecular Knudsen number regimes. Here we will first investigate whether a temperature gradient across the SpaceChip can generate additional radiometric forces, and then we will study how the surface temperature affects the drag coefficient.

Since atmospheric drag remains the most important force at the altitudes we are most interested in, it is assumed throughout this chapter that the forces and accelerations due to solar radiation pressure will not be modified by any heater plates or insulating layers added. Also, the orbit perturbation due to the Earths oblateness will be neglected in this study, as it does not depend on the spacecraft parameters, hence it cannot be engineered as a means of control. This allows an investigation solely of the effects of the radiometric forces and SpaceChip temperature on the drag coefficient.

6.1 Radiometric Forces

A rarefied gas surrounding a thin plate – such as a Crookes radiometer vane, or a SpaceChip – with a temperature difference between its two largest sides results in a force being generated that tends to move the plate in the direction from the hot to the

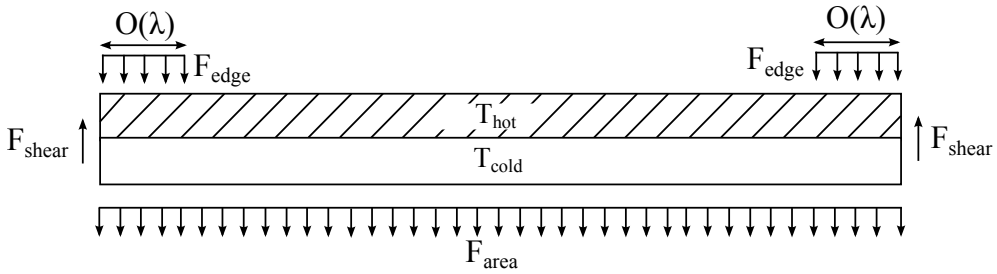

Figure 6.3: Schematic of the forces acting on a radiometer vane. The area force F_{area} acts over the large edge of the vane in the direction hot-to-cold, the edge force F_{edge} acts in the same direction in the order of a mean free path from the vane sides, and the shear force F_{shear} acts in the opposite direction along the short edge.

cold side. This problem was considered previously in §3.6, where the *dsmcFoam* code was benchmarked for radiometer applications. This radiometric force is composed of three components [56, 118, 119], as shown in Figure 6.3:

1. Area force – gas molecules that strike the hot side are reflected with greater energy than those which strike the cold side, causing a pressure difference across the vane, which acts in the direction hot-to-cold. This was first proposed by Reynolds [120]. Since this acts over the whole surface area of the vane face, it is called an area force.

2. Edge force – there is an increased pressure difference near the edges of the vane caused by non-uniformity of gas heating near the edges. This uneven heating was first shown by Maxwell [8] and is believed to act in a zone with dimensions of a mean free path from the edge. Einstein proposed a theory that related the magnitude of the radiometric force to the vane perimeter [121].

3. Shear force – a well known phenomenon in rarefied gases is gas molecules "creeping" from a cold region to a hot region. This is known as thermal transpiration or thermal creep. An analytical model [122] predicted that the shear force will act in the same direction as the area and edge forces, thus increasing the total radiometric force. However, numerical results [119] using both DSMC and the ellipsoidal-statistical Bhatnagar-Gross-Krook (ES-BGK) kinetic model contradict the analytical model and predict that the shear force acts in the opposite sense and therefore decreases the total radiometric force. It has been found [119] that the magnitude of the shear force decreases with decreasing vane thickness and

that angled vane edges can reduce the shear force contribution, or even change the direction in which it acts.

The area force is dominant under free molecular conditions. The pressure on the hot side of the vane is higher than on the cold side and so the resultant force moves the vane in the direction of hot to cold. However, as the surrounding gas density increases, inter-molecular collisions become significant and this leads to a situation where the area force eventually decreases to zero. Particles leaving the hot side do so with higher momentum and this makes them more effective at deflecting oncoming particles away from the vane surface. This reduces the particle flux hitting the vane and therefore reduces the pressure at the vane surface. The two effects cancel one another out and the overall result is that the pressure at the hot and cold surfaces become equal. This phenomenon has been demonstrated numerically using ES-BGK simulations [56].

As the pressure increases from the free molecular regime towards the transition regime, the radiometric force increases as the edge and shear forces become more important than the area force. The force then decreases again as the pressure increases further towards the continuum regime where no rarefaction effects are exhibited. This gives a bell-shaped force dependence on gas rarefaction, with the maximum force occurring at the point where the edge force effects are dominant. An example of radiometric forces being used for a practical purpose can be found in References [123, 124], where remote laser heating is used to heat a vane assembly in a rarefied gas environment with application as a microactuator.

It should be noted that the flow Mach numbers produced in the rarefied gas as a result of radiometric effects are typically very small, leading to problems with statistical scatter as discussed in the previous chapter [46]. A validation of *dsmcFoam* for radiometric forces can be found in §3.6, including a comparison of measured forces from our DSMC simulations to experimental results.

6.2 Non-Isothermal SpaceChips

Here we consider that the larger sides of a SpaceChip are at different temperatures – either passively (as a result of one side facing the Sun and the other being in shade, with

an insulating layer between the two sides), or actively controlled through a system such as a heater plate. Alternatively, electrochromic coating could be used, but this will also alter the forces due to solar radiation pressure, which may dominate in this situation. DSMC simulations are conducted considering a 50 K temperature difference across the thickness of the SpaceChip. While this is a very large temperature difference, the statistical nature of the numerical technique makes it prohibitively computationally expensive to simulate flows with temperature differences of 5 K or below; however, low variance DSMC methods [78] could be implemented in *dsmcFoam* in the future to remove this restriction. Low Earth orbit altitudes from 75 km to 1300 km are considered and SpaceChip flows are simulated in two dimensions using *dsmcFoam*. Comparison is then made with analytical solutions for both the radiometric force and the drag coefficient in the free-molecular flow regimes.

H (km)	n_{O_2} (m^{-3})	n_{N_2} (m^{-3})	n_O (m^{-3})	n_{Ar} (m^{-3})	n_{He} (m^{-3})	n_H (m^{-3})
75	1.522×10^{20}	5.726×10^{20}	-	-	-	-
100	2.151×10^{18}	9.210×10^{18}	4.298×10^{17}	9.501×10^{16}	1.133×10^{14}	-
200	1.918×10^{14}	2.925×10^{15}	4.050×10^{15}	1.938×10^{12}	1.310×10^{13}	1.630×10^{11}
400	1.252×10^{11}	4.669×10^{12}	9.583×10^{13}	2.124×10^{8}	4.868×10^{12}	8.960×10^{10}
600	1.880×10^{8}	1.575×10^{10}	3.707×10^{12}	6.351×10^{4}	2.154×10^{12}	7.231×10^{10}
800	4.105×10^{5}	7.377×10^{7}	1.732×10^{11}	3.027×10^{1}	1.001×10^{12}	5.961×10^{10}
1000	1.251×10^{3}	4.626×10^{5}	9.562×10^{9}	2.188×10^{-2}	4.850×10^{11}	4.967×10^{10}
1300	4.084×10^{2}	1.510×10^{5}	3.122×10^{9}	7.143×10^{-3}	1.583×10^{11}	1.620×10^{10}

Table 6.1: Atmospheric composition at different altitudes H; n is number density, i.e. the number of molecules of the indicated species per unit volume.

The case of a SpaceChip orbiting the Earth has similarities to the heated plate in a vacuum chamber. The surrounding gas is rarefied because of the extremely low gas density in the upper reaches of the atmosphere and, as outlined above, a temperature gradient is present across the 25 μm thickness of the SpaceChip [115]. This differs from previous numerical work on radiometer vanes and similar geometries because the gas is not single species and indeed even changes composition as altitude changes. Table 6.1 shows the atmospheric composition variation with altitude, taken from the US Standard Atmosphere 1976 [125]. The surrounding gas temperature initially decreases with altitude, but then rises to reach 1000 K by around 250 km [125]. A thermal analysis [115] of a SpaceChip geometry found that the surface temperatures of the chip would be well below the surrounding gas temperature at altitudes above 150 km.

Previous numerical work has been on vanes in stationary gases (see §3.6), or exposed to only very modest velocities [126]. However, the SpaceChip will be exposed to freestream velocities of approximately 7000 m/s as it orbits the Earth. It may be expected that the extremely low density wake produced behind a SpaceChip will prevent a radiometric force from being produced, but that similar rarefied gas physics should mean that the drag force acting on the SpaceChip will vary with surface temperature.

The velocity at which the SpaceChip orbits in the atmosphere is

$$U_\infty = \sqrt{\frac{G_{Earth}}{r_{orbit}}}, \tag{6.1}$$

where G_{Earth} is the gravitational parameter of the Earth, and the orbit radius r_{orbit} is defined as $(R_{Earth} + H)$, where R_{Earth} is the equatorial radius of the Earth (6378 km). The velocity U_∞ and atmospheric temperature T_∞ are given in Table 6.2 (the rotational velocity of the atmosphere has been neglected here).

H (km)	T_∞ (K) [125]	U_∞ (m/s)	ρ_∞ (kg/m^3)	Analytical drag force (N)
75	208.4	7859	3.47×10^{-5}	0.23
100	195.1	7840	5.60×10^{-7}	3.42×10^{-3}
200	854.6	7780	2.54×10^{-10}	1.77×10^{-6}
400	995.8	7670	2.80×10^{-12}	1.70×10^{-8}
600	995.9	7560	1.14×10^{-13}	8.72×10^{-10}
800	1000	7450	1.14×10^{-14}	6.82×10^{-11}
1000	1000	7350	3.56×10^{-15}	1.71×10^{-11}
1300	1000	7205	1.16×10^{-15}	6.32×10^{-12}

Table 6.2: Atmospheric temperature, SpaceChip orbit velocity, freestream mass densities and analytical drag forces at different altitudes.

The theoretical drag forces acting on the SpaceChip at each altitude can be calculated using the drag equation:

$$F_{\text{drag}} = \frac{1}{2} c_D \rho_\infty A U_\infty^2, \tag{6.2}$$

where c_D is the drag coefficient, ρ_∞ is the freestream atmospheric density, and A is the cross-sectional area exposed to the flow; c_D has initially been estimated to be 2.1 for the SpaceChip geometry. It is usual for preliminary mission analysis studies to consider a constant drag coefficient in the range 2.1 – 2.2 [127]; for high area-to-mass

ratio spacecraft, it is important to use an accurate drag coefficient and a later section will analyse the validity of this assumption. Table 6.2 contains the calculated values for the drag forces.

6.2.1 Stationary SpaceChips

First, we consider SpaceChips that are artificially stationary with respect to the atmosphere, in order to help distinguish radiometric force effects from atmospheric drag. All of the altitudes and gas compositions given in Tables 6.1 and 6.2 are simulated. Figure 6.4 is a schematic of the forces expected to be acting on these artificially stationary SpaceChips. The hot sides are considered to be at a constant temperature of 405 K, the cold sides are constant at 355 K and molecule-surface interactions are fully diffuse. The average temperature of 380 K is consistent with that predicted for a SpaceChip in orbit [110, 115].

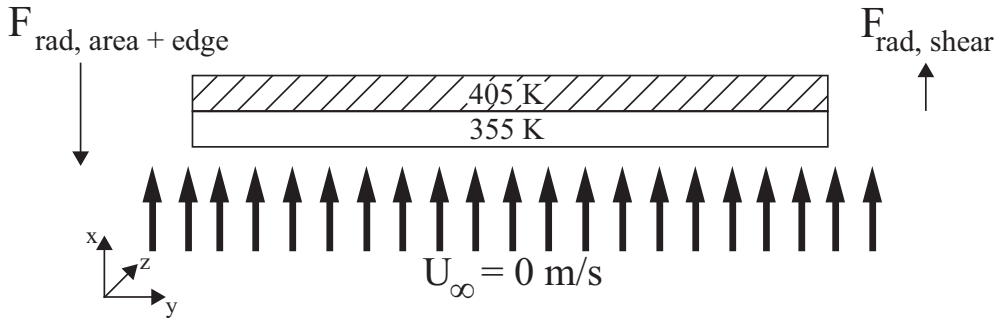

Figure 6.4: Schematic of the forces acting on an artificially stationary SpaceChip: $F_{\text{rad, area + edge}}$ are the edge and area forces described in §6.1 and $F_{\text{rad, shear}}$ is the shear force.

Table 6.3 shows the information used to determine the cell sizes and time steps required to obtain reliable DSMC results. In all of our simulations, the gas is simulated as a multi-component particle mixture. The mean free path λ, mean collision time t_{mc} and most probable thermal velocity c'_{mp} are taken from the US Standard Atmosphere 1976 [125]. The parameters have been chosen so that each simulation contains the same number of DSMC particles, and that each cell in the mesh initially contains a sufficient number of particles to meet good DSMC practice. The measured statistical error in each of the force results in the stationary SpaceChip cases with a 50 K temperature difference is approximately $\pm$ 2%, which is deemed acceptable for the current work. This statistical error was calculated as the standard error in the instantaneous force

measurements.

H (km)	λ (m)	t_{mc} (s)	F_N	c'_{mp} (m/s)
75	2.3×10^{-3}	6.0×10^{-6}	1.6×10^{9}	388.7
100	1.4×10^{-1}	3.7×10^{-4}	1.1×10^{7}	381.4
200	2.4×10^{2}	0.3	6460.0	921.6
400	1.6×10^{4}	13.9	96.0	1148.5
600	2.8×10^{5}	208.3	5.0	1356.3
800	1.4×10^{6}	714.3	1.1	1954.3
1000	3.1×10^{6}	1333.3	0.5	2318.1
1300	1.0×10^{7}	3333.3	0.16	2500.0

Table 6.3: SpaceChip DSMC simulation parameters.

Figure 6.5 shows the computed radiometric forces acting on the stationary SpaceChip at different altitudes. The solar radiation pressure for reflectivity coefficients c_R of 1.0 and 1.8 are also shown for reference, along with the analytical drag force using a drag coefficient of 2.1. The range of applicability of this drag coefficient will be tested in a later section.

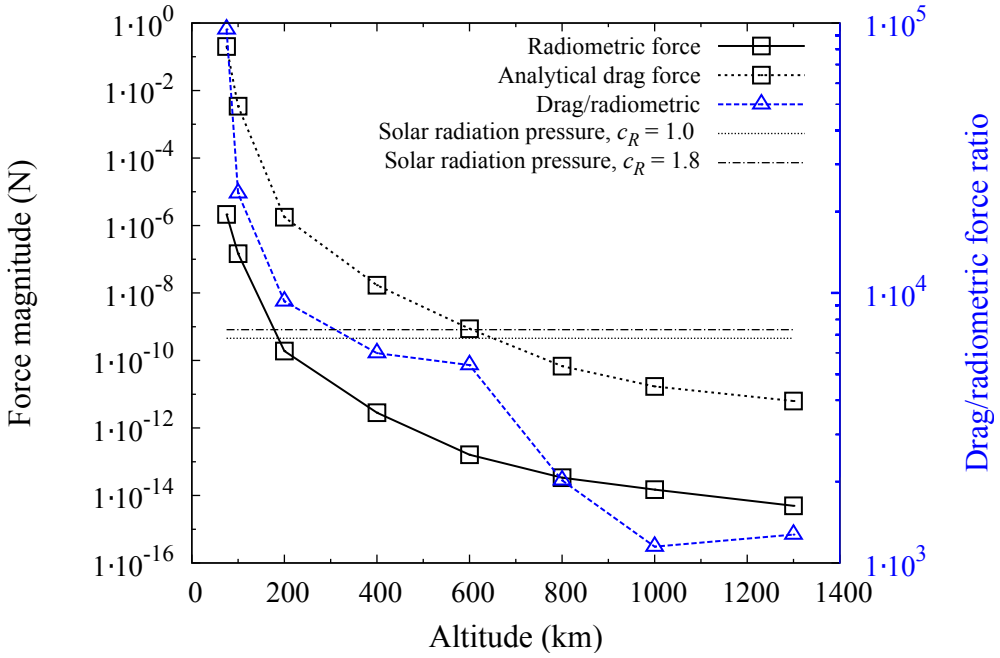

Figure 6.5: Variation of radiometric forces with altitude. The theoretical drag force is shown for reference, and the ratio of the two forces has also been plotted.

Figure 6.5 shows that the predicted radiometric forces are around three to four orders of magnitude smaller than the expected drag forces, with the radiometric force

becoming relatively more important as the altitude increases. The measured forces are all very small, but so is the mass of the SpaceChip (around 5.75 $\times 10^{-6}$ kg): the acceleration due to the radiometric force at 600 km is 3.5 $\times 10^{-9}$ m/s^2. It is interesting to note that at this altitude the accelerations due to drag and solar radiation pressure are expected to be of roughly the same magnitude (based on atmospheric conditions from the US Standard Atmosphere [125]). At altitudes below 600 km, atmospheric drag is the dominant force. At higher altitudes, forces due to solar radiation pressure dominate. Therefore, any rarefied gas effects that can be taken advantage of will be most effective at altitudes of up to 600 km.

An analytical solution for the radiometric force in the free-molecular regime is given in Reference [56] as:

$$F = \frac{P_\infty}{2} A \left(\sqrt{\frac{\sigma_M T_h + (1 - \sigma_M) T_\infty}{T_\infty}} - \sqrt{\frac{\sigma_M T_c + (1 - \sigma_M) T_\infty}{T_\infty}} \right), \qquad (6.3)$$

where P_∞ is the freestream pressure, σ_M is Maxwell's accommodation coefficient, and T_h and T_c are the temperature of the hot and cold side of the radiometer vane, respectively.

Table 6.4 compares the forces calculated using Equation (6.3) with those obtained from our DSMC simulations. At 75 km altitude, the flow is clearly not free-molecular and elements of collisional flow are dominating, which Equation (6.3) cannot account for. From 100 km and up, the flow can be considered close to free-molecular — demonstrated by the analytical and numerical results being in good agreement.

H (km)	F/P_{sim} (N/Pa)	F/P_{analy} (N/Pa)	Ratio
75	1.090×10^{-6}	4.444×10^{-6}	0.245
100	4.569×10^{-6}	4.594×10^{-6}	0.995
200	2.244×10^{-6}	2.195×10^{-6}	1.022
400	1.958×10^{-6}	2.033×10^{-6}	0.963
600	1.988×10^{-6}	2.029×10^{-6}	0.978
800	1.978×10^{-6}	2.029×10^{-6}	0.975
1000	1.981×10^{-6}	2.029×10^{-6}	0.977
1300	2.022×10^{-6}	2.029×10^{-6}	0.996

Table 6.4: Force per unit pressure values, calculated from our simulations and an independent analytical approach.

6.2.2 Orbiting SpaceChips

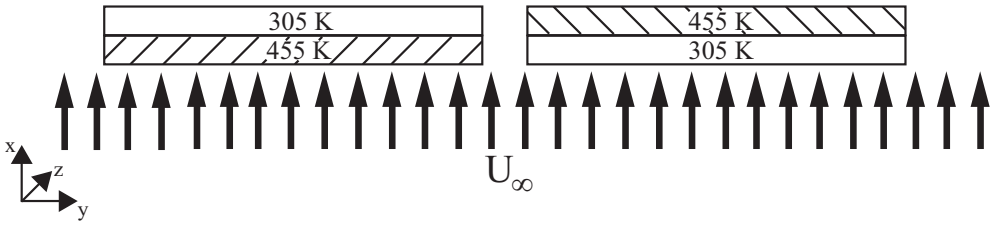

Figure 6.6: Schematic of orbiting non-isothermal SpaceChip simulations. Left: flow incident on the hot face; right: Flow incident on the cold face.

We now consider a SpaceChip travelling at the velocity at which it would orbit the Earth at each altitude considered, as set out in Table 6.2. We consider the maximum drag configuration, i.e. when the SpaceChip lies perpendicular to the flow. In this case, a near-vacuum wake will be produced immediately downstream of the SpaceChip. It is therefore possible that the gas flow will not experience the temperature gradient between the two faces. In order to test this, isothermal cases are also performed where the orbiting SpaceChips have a uniform temperature equal either to that of the hot face or the cold face of a non-isothermal SpaceChip.

H (km)	F_{cold} (N)	F_{hot} (N)
75	2.017×10^{-1}	2.017×10^{-1}
100	3.445×10^{-3}	3.458×10^{-3}
200	1.637×10^{-6}	1.643×10^{-6}
400	1.777×10^{-8}	1.785×10^{-8}
600	7.089×10^{-10}	7.128×10^{-10}
800	7.208×10^{-11}	7.258×10^{-11}
1000	2.278×10^{-11}	2.297×10^{-11}
1300	7.175×10^{-12}	7.241×10^{-12}

Table 6.5: Forces obtained from DSMC simulations on orbiting SpaceChips with the flow incident on either the hot or the cold face.

Table 6.5 shows the forces computed on non-isothermal SpaceChips traveling so the gas is incident on either the hot (see Figure 6.6, left side) or cold (see Figure 6.6, right side) face of the SpaceChip, F_{hot} and F_{cold} respectively. The measured statistical error for these forces is around $\pm$ 0.015%, and the difference between the two forces at each altitude is comfortably outside of this statistical error range (for all altitudes above 75 km).

Temperature (K)	355		405	
	Isothermal	Non-isothermal	Isothermal	Non-isothermal
Force (N)	7.2075×10^{-11}	7.2078×10^{-11}	7.2563×10^{-11}	7.2578×10^{-11}

Table 6.6: Comparison of forces in the isothermal and non-isothermal SpaceChip cases at 800 km.

Table 6.6 compares the drag forces on the isothermal SpaceChips at 800 km with those for the non-isothermal SpaceChips at the same altitude. The temperature for each non-isothermal case is the temperature of the side of the SpaceChip that the gas flow is incident on, while in the isothermal cases the whole SpaceChip is at the stated temperature. The forces are very similar and fall within the measured statistical error of $\pm$ 0.015%. Therefore, as expected, we can say that there is no radiometric contribution to the overall force acting on a SpaceChip in orbit, because the region immediately downstream of the SpaceChip is effectively a vacuum. The only force that needs to be accounted for is a standard aerodynamic pressure drag force for this maximum drag configuration.

Despite there not being any substantive radiometric force contribution, it is still evident that when the surface temperature of the SpaceChip changes, the drag force changes: an increase in temperature increases the drag. Although this is not a radiometric force, it can be understood through the same reasoning considered previously for the free-molecular pressure force contribution to the overall radiometric force. At altitudes of 100 km and above, the gaseous flow is in the free-molecular regime, so inter-molecular collisions are not significant. The pre-interaction momentum remains unchanged as the surface temperature changes. When molecules collide with the surface they are reflected, but do not deflect oncoming molecules as would happen in the transition and continuum regimes. This means that the molecule flux hitting the surface is unaffected by the surface temperature, and so the pressure at the surface which results in the drag force is simply related to the difference in momentum of molecules before and after they interact with the surface.

As it has also been demonstrated that it is the temperature of the side on which the gas is incident that is important, and not the temperature difference between the

two sides, we consider all SpaceChips to be isothermal in the remainder of this section. The results from Table 6.5 can still be used for this purpose, as the results in Table 6.6 demonstrate. The difference in the drag forces on a hot and on a cold SpaceChip F_Δ is defined as

$$F_\Delta = \left| \frac{|F_{hot}| - |F_{cold}|}{2} \right|. \tag{6.4}$$

Then the ratio of the force acting on an isothermal SpaceChip at the average temperature $F_{av.}$ to F_Δ can be used to calculate how much of an effect changing the spacecraft's temperature has on the drag force.

A set of DSMC simulations at the average temperature of 380 K were performed. Figure 6.7 shows a plot of this ratio $F_{av.}/F_\Delta$ varying with altitude, with F_{hot} and F_{cold} being found for temperatures of 405 K and 355 K respectively.

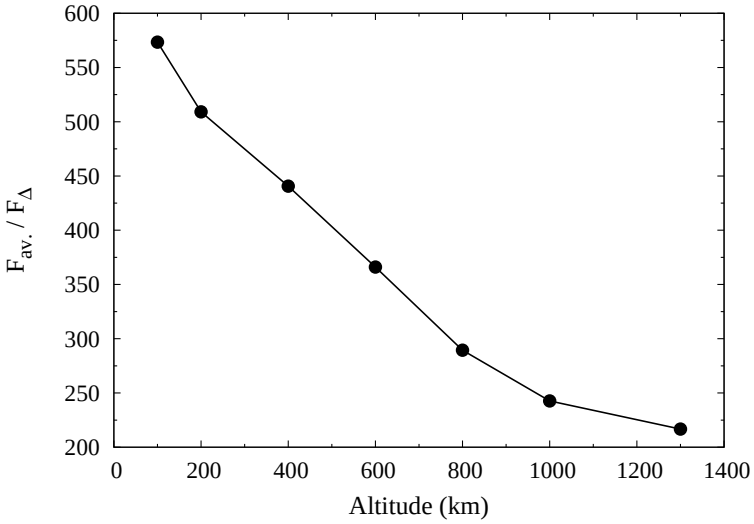

Figure 6.7: Variation of $F_{av.}/F_\Delta$ with altitude of SpaceChip.

Clearly F_Δ increases (relative to the drag force at the average temperature $F_{av.}$) with altitude. Since the drag force can be changed by changing the surface temperature (provided no other parameters are altered), it is concluded that the drag coefficient is changing with the spacecraft's temperature.

6.3 Drag Coefficient

There are several analytical solutions available for calculating the drag coefficient of a flat plate in a free-molecular flow. Two different expressions are given in Reference [128]: one for hyperthermal flow and one for non-hyperthermal flow, where a hyperthermal flow is defined as one in which the thermal component of the gas molecular velocities is negligible compared to the macroscopic velocity, i.e. $U_\infty \gg c'_{mp}$. It is not always certain that the flow in the current work can be considered hyperthermal (e.g. at 1000 km, $c'_{mp}/U_\infty = 0.315$) and so both forms of the analytical expression are considered here. The hyperthermal and non-hyperthermal equations are given as

$$c_{D_{\text{hyperthermal}}} = 2\left[\sigma_M + \sigma_M \frac{c'_w}{U_\infty}\sin(\alpha) + (2 - 2\sigma_M)\sin^2(\alpha)\right]\sin(\alpha), \tag{6.5}$$

and

$$\begin{aligned} c_{D_{\text{non-hyperthermal}}} = {} & 2\sigma_M \frac{c'_w}{U_\infty}\sin^2(\alpha) \\ & + \frac{2}{\sqrt{\pi}s}\left[(2 - \sigma_M)\sin^2(\alpha) + \sigma_M \cos^2(\alpha)\right]\exp(-s^2\sin^2(\alpha)) \\ & + 2\left[(2 - \sigma_M)\left(\sin^2(\alpha) + \frac{1}{2s^2}\right) + \sigma_M \cos^2(\alpha)\right]\sin(\alpha)\text{erf}(s\sin(\alpha)), \end{aligned} \tag{6.6}$$

respectively, where

$$c'_w = \sqrt{\frac{\pi k_B T_w}{2m}}, \tag{6.7}$$

s is the molecular speed ratio

$$s = U_\infty / c'_{mp}, \tag{6.8}$$

T_w is the SpaceChip temperature, α is the angle of attack, m is the molecular mass, and σ_M is Maxwell's accommodation coefficient fraction.

Note that as s tends to ∞, Equation (6.6) reduces to Equation (6.5). A further

analytical expression from Reference [21] is given as

$$\begin{aligned} c_{D_{\text{Bird}}} = \; & 2\frac{\{1-\kappa\cos(2\alpha)\}}{\sqrt{\pi}s}\exp\left(-s^2\sin^2(\alpha)\right) \\ & + \frac{\sin(\alpha)}{s^2}\left[1+2s^2+\kappa\left\{1-2s^2\cos(2\alpha)\right\}\right]\text{erf}(s\sin(\alpha)) \\ & + \frac{(1-\kappa)}{s}\sqrt{\pi}\sin^2(\alpha)\left(\frac{T_w}{T_\infty}\right)^{\frac{1}{2}}, \end{aligned} \tag{6.9}$$

where $\kappa = 1 - \sigma_M$.

In Figure 6.8, results from Equations (6.5) – (6.9) are compared to the drag coefficients obtained from our DSMC simulations for flow incident on a a fully accommodating isothermal SpaceChip with our maximum considered surface temperature of 405 K. This temperature has been chosen arbitrarily, but similar results with slightly smaller drag coefficients are found for lower temperatures. The angle of attack is constant at 90° for all of the current analysis.

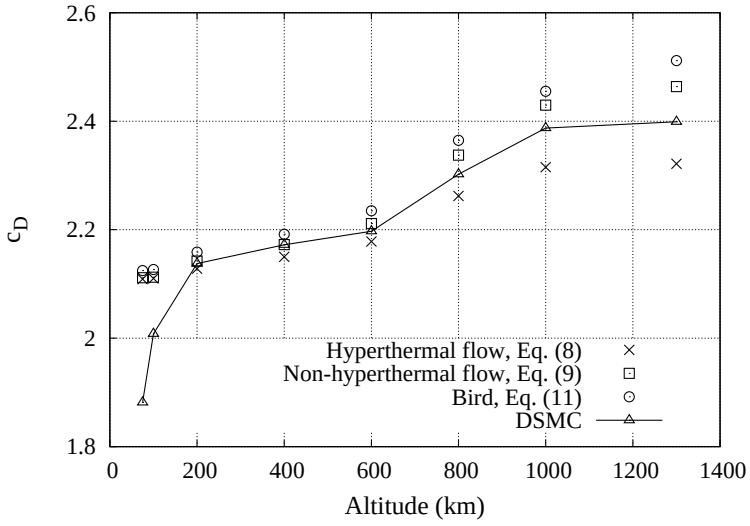

Figure 6.8: Variation of c_D with altitude, calculated using different analytical and DSMC solutions, and for a SpaceChip surface temperature of 405 K.

For this limiting case of maximum drag configuration, the three different analytical expressions and our DSMC solution follow the general trend of drag coefficient increasing with altitude, with the DSMC solutions within 5% of the analytical results. The numerical results fall between the hyperthermal and non-hyperthermal solutions, but are closer to the non-hyperthermal, indicating that typical orbital velocities tend to

lie between the hyperthermal and non-hyperthermal limits. The DSMC results do not match the analytical solutions at 75 km and 100 km: in §6.2.1 it was established that the flow is not free-molecular at 75 km, so this is expected. However, at 100 km the flow is free-molecular for the case of a stationary SpaceChip, but this does not appear to be the case for an orbiting SpaceChip. The large velocity leads to an increased density at the forward stagnation point and this increase in density is large enough to reduce the local mean free path, making inter-molecular collisions important in the stagnation region, despite them being negligible in the freestream.

All of our work has so far considered fully diffuse surfaces, but the drag coefficient is expected to be highly sensitive to different values of the accommodation coefficient. For example, Table 6.7 shows the drag coefficients obtained using Equation (6.9) for a surface temperature of 355 K and altitude of 1300 km with the freestream conditions set out in Table 6.2, but with different accommodation coefficients, and for the limiting case of angle of attack $alpha = 90°$. Higher temperatures give the same pattern, only with slightly larger drag coefficient values. A vacuum environment has a 'cleaning' effect on surfaces and results in a surface that is less than fully accommodating [21]. It is clear that a real surface, for which $\sigma < 1$, may have a significantly greater drag coefficient than a perfectly diffuse surface. On the other hand, atomic oxygen adsorption on the surface of a satellite may cause the accommodation coefficient to remain close to unity [129]. The pressure at a surface is related to the difference between the incident and reflected momentum of gas molecules through

$$P = \frac{1}{t_s A}\left(\sum_{i=1}^{N_s}\left(mc_{n,i}\right)^{inc} - \sum_{i=1}^{N_s}\left(mc_{n,i}\right)^{refl}\right), \tag{6.10}$$

where N_s is the total number of molecules incident on the surface of area A in a time period t_s, c_n is the component of the molecular velocity normal to the surface, and the superscripts *inc* and *refl* stand for "incident" and "reflected", respectively.

In the case of a specular reflection, the normal component of the incident velocity simply changes sign. For the SpaceChips considered here, the magnitude of the reflected normal component from a diffuse reflection will (on average) be smaller because the surface temperature T_w is lower than the freestream temperature T_∞. A

H (km)	c_D		
	$\sigma_M = 1$	$\sigma_M = 0.8$	$\sigma_M = 0.5$
75	2.117	2.494	3.061
100	2.119	2.496	3.062
200	2.149	2.525	3.089
400	2.181	2.554	3.113
600	2.222	2.591	3.143
800	2.346	2.704	3.242
1000	2.433	2.786	3.316
1300	2.487	2.838	3.364

Table 6.7: Drag coefficients from Equation (6.9) for different SpaceChip surface accommodation coefficients.

reduced accommodation coefficient means an increased number of specular reflections, and hence an increase in the drag coefficient. The SpaceChip will not equilibrate to the freestream gas temperature as the power flux from the incident gas molecules is negligible compared to that from the radiation from the sun, and so does not greatly affect the radiative energy balance when calculating the SpaceChip temperature.

Determination of accommodation coefficients are often made experimentally and must take into account the surface material, surface roughness and gas composition. For example, in Reference [130] the accommodation coefficients for silicon micro-channels conveying argon and nitrogen gas are determined by comparing experimental results for the mass flow rates with analytical solutions for Poiseuille flow. Molecular dynamics simulations can also be used to determine accommodation coefficients, but it is important to use accurate molecule-molecule and molecule-surface interaction potentials, and this data is not always readily available [131, 132].

The magnitude of the changes in the drag force that can be obtained by increasing or decreasing the surface temperature are relatively small, producing a difference $\mathcal{O}(10^{-14})$ N for a 25 K temperature increase or decrease. The difference in drag force will be much smaller for smaller temperature changes, but the statistical nature (and low signal-to-noise characteristics) of DSMC makes simulating such small temperature differences impractical. However, a small change in drag force could be used to advantage in missions involving swarms of SpaceChips. If a means of controlling the temperature of individual SpaceChips can be implemented, e.g. through an integral heater plate, it

will be possible to use this change of temperature as a control method for changing the relative positions of individual SpaceChips within a swarm. The magnitude of the force would be predictable and repeatable and the fact that it is extremely small would allow for precise position control of individual SpaceChips. This close control application would be most applicable at orbit altitudes between 200 km and 600 km, where modifying the drag coefficient can have a decisive effect on the overall force acting on a SpaceChip.

Figure 6.9 shows the predicted drag coefficients from our DSMC simulations alongside the analytical solutions at 600 km, as the temperature increases from around the minimum to the maximum predicted temperatures for a SpaceChip [110, 115]. The DSMC results match the analytical expressions well, particularly the non-hyperthermal flow solution of Equation (6.6). It is clear that it is possible to exert a small degree of control over the drag coefficient at this altitude through modifying the surface temperature.

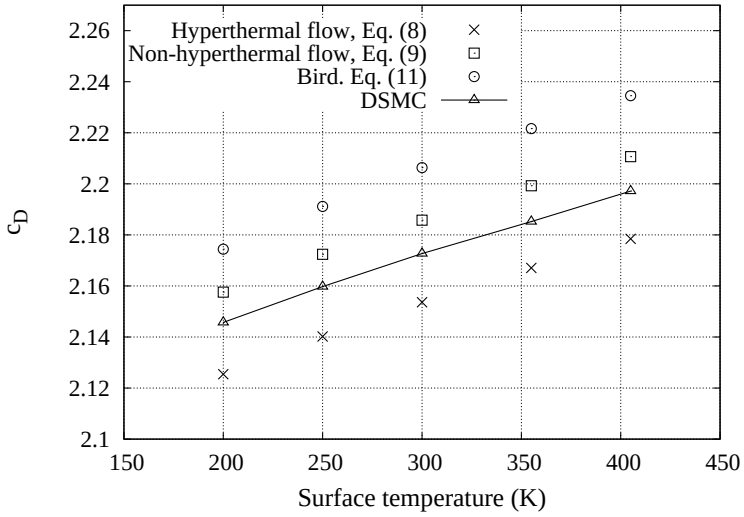

Figure 6.9: Variation of c_D with different SpaceChip temperatures, at an altitude of 600 km.

A drag coefficient of 2.1 is commonly used when performing preliminary SpaceChip mission analysis but, as we have shown, the drag coefficient (considering fully diffuse surfaces) can vary from around 1.9 to 2.5 as altitude and SpaceChip temperature increases. When accommodation coefficients of less than 1 are considered, the drag coefficient values are even greater.

6.3.1 Position Control

Assuming a SpaceChip of dimensions of 1 cm $\times$ 1 cm $\times$ 25 μm with a density equal to that of silicon (2300 kg m^{-3}), the total control acceleration available between temperatures of 200 K and 405 K is 2.9 $\times$ 10^{-6} m s^{-2}. For a circular orbit at 600 km, having a period of 5820 s, the inter-spacecraft change in velocity Δv per orbit is 0.017 m s^{-1} and the inter-spacecraft displacement Δs per orbit is therefore 50 m. This means that it is possible to alter the position of a single SpaceChip with respect to another one by up to 50 m in a single orbit by modifying the surface temperature to increase or decrease the drag coefficient. Smaller temperature differences will lead to smaller Δs, e.g. changing surface temperature from 300 K to 355 K gives a control acceleration of 7.05 $\times$ 10^{-7} m s $^{-2}$ and Δs per orbit is reduced to 12 m. This demonstrates that very small temperature differences could be used to produce useful values of Δv and Δs for performing position control.

Until now, it has been considered that the SpaceChips will remain perfectly perpendicular to the flow, and that they are at exactly the same altitude. In reality, this is not sustainable (e.g. due to the effect of variable wind direction on drag); therefore, a disturbance analysis is carried out. Note that, if we assume that the change in temperature does not affect the reflectivity coefficient, the characteristic acceleration due to solar radiation pressure can be considered constant in low Earth orbit. In addition, it has been demonstrated [133], at altitudes of around 600 km and a length scale of 1 cm, that accelerations due to drag are more significant than those due to solar radiation pressure. It has also been shown that the accelerations due to magnetism, in the form of Lorentz accelerations, are significantly less important than atmospheric drag accelerations at this altitude.

To study the effect of aerodynamic disturbances on inter-spacecraft displacement per orbit, it is first considered that one SpaceChip remains at the maximum drag configuration, while a second one can have angles of attack up to $\pm$ 20° from the maximum drag configuration. We then consider that two SpaceChips with the same attitude can be at different altitudes. The distance between two SpaceChips in a distributed sensor network is not likely to be greater than 1 km, as discussed previously, so an analysis of an altitude separation of up to 4 km is considered sufficient here. The

drag coefficients for the analysis have been calculated using Equation (6.9).

In order to study the effect of the angle of attack α on the inter-spacecraft displacement of two SpaceChips at different temperatures and an altitude of 600 km, the parameter Δc_D is introduced:

$$\Delta c_D = \left(c_{D_{200\text{ K},\alpha=90}} - c_{D_{405\text{ K},\alpha}}\right), \tag{6.11}$$

or

$$\Delta c_D = \left(c_{D_{405\text{ K},\alpha=90}} - c_{D_{200\text{ K},\alpha}}\right), \tag{6.12}$$

when the SpaceChip at 200 K is at constant angle of attack or the one at 405 K is at constant angle of attack, respectively; $c_{D_{200\text{ K},\alpha=90}}$ and $c_{D_{405\text{ K},\alpha=90}}$ are the drag coefficients when the temperature is 200 K or 405 K, and the angle of attack is constant at 90°; $c_{D_{200\text{ K},\alpha}}$ and $c_{D_{405\text{ K},\alpha}}$ are the drag coefficients for SpaceChips at temperatures of 200 K and 405 K respectively, at angle of attack α.

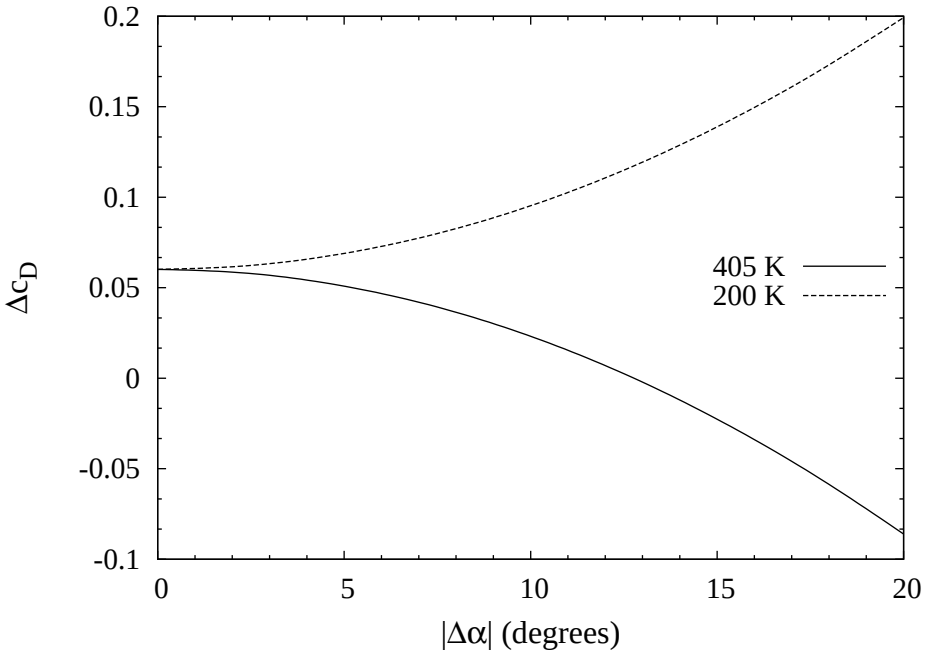

Figure 6.10: Variation of Δc_D with change in angle of attack $|\Delta\alpha|$ at 600 km for SpaceChips at 200 K and 405 K. The legend indicates which SpaceChip is having its angle of attack altered.

Figure 6.10 shows the variation of Δc_D for different angles of attack, where $|\Delta\alpha|$ is the difference in angle of attack between the two SpaceChips. When the SpaceChip

at 405 K has its angle of attack varied with respect to the one at 200 K, it is clear that the change in drag coefficient decreases, hence a smaller control acceleration is available in this situation. Until the situation where the 405 K SpaceChip has an angle of attack of 77° or 103° ($|\Delta\alpha| = 13°$) it is still possible to create a positive control acceleration. For example, using Equation (6.9), when both have $\alpha = 90°$ the inter-spacecraft displacement in one orbit is 59 m, but when the 405 K SpaceChip has an angle of attack of 11° this is reduced to 14 m. On the other hand, it is found that varying the angle of attack of the SpaceChip at 200 K always increases the control acceleration available. When the 200 K SpaceChip has an angle of attack of 11°, the inter-spacecraft displacement in a single orbit is increased to 100 m.

If two SpaceChips are not at the same altitude, they will experience slightly different forces due to the different atmospheric densities and orbital velocities. Here, we consider an altitude of 600 ± 2 km. If the 405 K SpaceChip is at 602 km and the 200 K one is at 598 km, the control acceleration available is 1.58×10^{-6} m s $^{-2}$, which is around half that available when both are at an altitude of 600 km. If the 200 K SpaceChip is at 602 km and the 405 K one is at 598 km, the control acceleration is around double that when both are at 600 km: 5.25×10^{-6} m s $^{-2}$.

For both attitude and altitude differences, it is clear that the aerodynamic disturbances can enhance or restrict the level of position control available to a SpaceChip operator. Position control is still achievable in all but one of our studied disturbances – it is not found when the 405 K SpaceChip has a relative angle of attack $\Delta\alpha$ of 13°with respect to the 200 K one which is at the maximum drag coefficient.

In addition to altitude and attitude differences between individual SpaceChips, the atmospheric conditions themselves are dependent on a number of factors that the US Standard Atmosphere [125] model considered in the current work does not account for. Solar activity is one such factor, and it has been found that periods of exceptional solar activity increase the local density and alter the atmospheric composition at orbital altitudes where the drag force is still dominant [134, 135].

6.3.2 Attitude Control

Previously it was considered that the SpaceChip temperature was uniform. But if its temperature could be modified non-uniformly it should be possible to create a moment around the centre of mass. This moment could be used to change the attitude of individual SpaceChips. A similar strategy for attitude control was proposed for the IKAROS solar sail mission, although based in that case on changing the reflectivity coefficient: a solar sail was designed with some variable reflectance elements loaded near the tips of the sail membrane. By changing the reflectivity coefficient, control of the spin direction was achieved [136]. In a similar way here, a change of drag coefficient can be exploited to control the attitude of a SpaceChip (or even a solar sail in the atmosphere) without the use of a propellant.

In order to test if it is indeed possible to create a moment that could be used to control the attitude of individual SpaceChips at an altitude of interest (identified as 600 km), a SpaceChip with a non-uniform temperature is considered: one half of the SpaceChip is maintained at 355 K, and the other half at 405 K, see Figure 6.11.

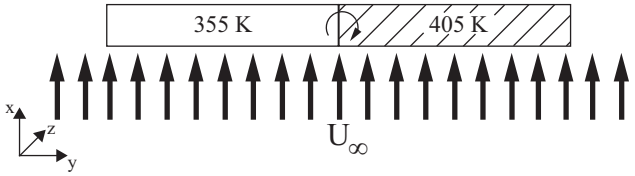

Figure 6.11: Schematic of SpaceChip non-uniform temperature geometry considered for attitude control.

We performed a two-dimensional DSMC simulation of this above geometry at 600 km, and measured the moments around the centre of mass of the SpaceChip at steady-state. With respect to Figure 6.11, the moments considered here will be around the z-axis. A moment of -1.78 $\times 10^{-12}$ Nm is produced by the hot half of the SpaceChip, while the cold side produces a moment of 1.77 $\times 10^{-12}$ Nm. The overall moment around the centre of mass is -1 $\times 10^{-14}$ Nm, so the SpaceChip will rotate slowly in an anti-clockwise direction. The moment of inertia of the SpaceChip geometry considered here is 4.79 $\times$ 10^{-11} kg m^2; therefore an angular acceleration of 1.2 $\times$ 10^{-2} deg s^{-2} (2.1 $\times$ 10^{-4} rad s^{-2}) is induced.

Similar to position control, disturbance torques can be important in any spacecraft

and here we perform an analysis of these disturbances. The most important disturbance torques are gravity gradient, solar radiation, magnetic field, and aerodynamic force [137]. The gravity gradient torque T_g is calculated as [137]:

$$T_g = \frac{3G_{Earth}}{2r_{orbit}} |I_x - I_z| \sin(2\theta), \tag{6.13}$$

where I_x and I_z are the mass moments of inertia around the x and z axes of Figure 6.11, respectively, and θ is the angular deviation from the local horizontal. The maximum gravity gradient disturbance for the 20° angle of attack disturbance at 600 km considered is considerably less than the control torque available; 2.88×10^{-17} Nm, and so is not important.

The magnetic field torque is given by $T_m = DB$, where D is the residual dipole of the SpaceChip, and B is the Earth's local magnetic field. We assume best and worst case residual magnetic dipoles of 2.5×10^{-10} Am^2 and 2.5×10^{-9} Am^2, respectively [133]. The worst case magnetic field at the poles for an altitude of 600 km is 4.69×10^{-5} T, reducing to half of this in the best case at the equator. This gives a worst case magnetic torque of 1.17×10^{-13} Nm and a best case of 5.86×10^{-15} Nm. The magnitude of the temperature-based control torque is slightly greater than the best case magnetic disturbance, indicating that a small amount of attitude control could be exercised around the equator for this example. Nearer the poles the magnetic disturbance torque is greater than the control torque we calculated would be available.

The aerodynamic torque is:

$$T_a = F_{drag}(c_{pa} - c_g), \tag{6.14}$$

where c_{pa} is the centre of pressure, and c_g is the centre of gravity. The centre of pressure position with changing angle of attack has been estimated using Avanzini's law [138]:

$$c_{pa} = L(0.2 + 0.3 \sin\alpha), \tag{6.15}$$

where L is the SpaceChip length. With this estimate for the position of c_{pa}, and assuming that the centre of gravity is at the geometrical centre of the SpaceChip,

the magnitude of the aerodynamic disturbance torque is found to be greater than the control torque of 1 $\times 10^{-14}$ Nm once the angle of attack is $\pm$ 5° from the maximum drag configuration. At our 20° maximum disturbance, the aerodynamic torque is much larger than the control torque; 1.2×10^{-13} Nm.

The solar radiation pressure disturbance torque is related to the difference in position between the centre of gravity and the centre of solar pressure. Since we are considering that the solar radiation pressure forces and accelerations remain constant as the temperature changes, our centre of solar pressure will not move, and we assume it is at the same position as the centre of gravity; hence, there is no disturbance torque due to solar radiation pressure in our current analysis.

For the large temperature difference considered in this example, the available angular slew is only 5°; smaller temperature differences would create smaller control torques and so it is found that non-uniform temperature control is not a practical control method for SpaceChips in low Earth orbit.

6.4 Summary

We have investigated rarefied gas effects on high area-to-mass ratio spacecraft in low Earth orbit, taking inspiration from the classical Crookes radiometer. It was found that the same forces that result in a radiometer vane turning were not present on non-isothermal SpaceChips due to the near vacuum wake on the downstream side of the spacecraft preventing any gas molecules from interacting with that side. However, advantage could still be taken of similar rarefaction effects that result in the drag coefficient slightly changing with the spacecraft's temperature and altitude.

Our numerical results were in good agreement with analytical solutions for the drag coefficient in free-molecular flow, and it was found that the drag coefficient of a SpaceChip varies from 1.9 to 2.4 with an increase in altitude from 100 km to 1300 km when the SpaceChip temperature is constant at 405 K. It is usual to assume a constant drag coefficient of around 2.1 for these small spacecraft when performing preliminary mission analysis, so this information could be used by mission designers to more accurately predict the atmospheric drag forces. When the accommodation coefficient was reduced in order to investigate more realistic surface behaviour, the

drag coefficient increased further; as high as 3.36 at a temperature of 355 K, altitude of 1300 km, and accommodation coefficient of 0.5. However, there is evidence to suggest that atomic oxygen adsorption on the surface of a satellite will keep the accommodation coefficient close to unity.

We proposed using these changes in drag coefficient, along with the high area-to-mass ratio of SpaceChips, to create accelerations that can be used as propellant-free control methods. In a swarm, individual SpaceChips could be moved relative to one another by controlling their temperatures, and we demonstrated that inter-spacecraft displacements can be generated in this way. A disturbance analysis for position control, taking into account angle of attack and altitude differences between two SpaceChips, showed that a level of control would still be available to the SpaceChip controller for most of our worst-case scenarios. Disturbances could even, in some cases, enhance the control accelerations available.

A natural extension to the opportunity for position control would be that of attitude control by modifying the temperature of a SpaceChip non-uniformly. It was demonstrated that torques could be produced in this way, but a disturbance analysis has indicated that aerodynamic disturbances will prevent attitude control slews of greater than 5° at 600 km. In addition, the magnetic field disturbance torque makes any attitude control unfeasible for the SpaceChip we considered, unless it is orbiting near the equator. Small, more practical, temperature differences would also greatly decrease the available control torques.

Chapter 7

Conclusions

The farther backward you can look,
the farther forward you can see.
- Winston Churchill

7.1 Summary

This thesis benchmarked the *dsmcFoam* solver for a wide variety of different rarefied gas flow situations. Our results were compared to independent DSMC results in the literature, analytical solutions, and experimental results where available. Simulated collision rates in adiabatic boxes for single species and gas mixtures were in excellent agreement with the analytical solution for an equilibrium VHS gas. Measurements of mixed Maxwellian diffuse and specular scattering angles compared well to an analytical solution for a fully diffuse surface, and numerical results from the MONACO code for lower accommodation coefficients. Hypersonic test cases showed good agreement with results from MONACO and Bird's solvers for both flow field and surface properties. Our numerical results for the force acting on a radiometer vane were in good agreement with experimental data and numerical results from the SMILE solver.

We have extended *dsmcFoam* to include features that enable it to be used to perform more realistic simulations of hypersonic applications, such as re-entry of spacecraft. Vibrational energy was added to the code, using the equally spaced quantum level harmonic oscillator model. This was validated against analytical solutions for

the probability distribution of vibrational quantum level, and the number of effective vibrational degrees of freedom. The relaxation of a gas in an initial state of vibrational non-equilibrium showed excellent agreement with previous numerical results for both the equilibrium temperature and the rate of relaxation to that temperature.

The quantum-kinetic chemistry model was then implemented, with our results for dissociation and exchange reaction rates in an adiabatic box filled with an equilibrium gas showing reasonable agreement with analytical QK rates, and total collision energy rates. Most of the reactions showed good agreement; however, the DSMC results for the exchange reactions are unable to match the analytical QK rates unless the adjustable parameters in these reactions have specific values.

A framework to measure both macroscopic and microscopic properties was introduced to *dsmcFoam*, based on the one implemented in OpenFOAM's molecular dynamics solver *mdFoam*. Several examples of this framework being used were presented, including measurement of mass flow rates to show the Knudsen minimum phenomenon. The Cercignani-Lampis-Lord model was implemented and benchmarked, increasing the choice of gas-surface interaction models available to *dsmcFoam* users.

Continuum-based boundary conditions for low-speed gas flows were implemented in *dsmcFoam*, and benchmarked against analytical solutions for micro-channel flows and previous numerical results. These boundary conditions were then extended to account for rotational non-equilibrium at the outlet, before being used to investigate gas flows in micro-channels with bends. We found that, in a small range of Knudsen number, the presence of a bend in a micro-channel can increase the mass flow rate compared to an equivalent straight channel. This had been found previously using the lattice Boltzmann method, but our results are the first time it has been found with DSMC. Shear stress and velocity slip profiles were calculated for the Knudsen number where the largest mass flux enhancement was found. Normalised values of average shear stress at the bent micro-channel walls are closer to unity in cases where a positive mass flux enhancement was found.

Rarefied cylindrical Couette flow between two concentric cylinders was simulated for a range of Knudsen numbers, accommodation coefficients, and inner-to-outer cylinder radii. We found that non-equilibrium effects in these geometries are dependent on both

Knudsen number and curvature; non-equilibrium effects were increased at the inner cylinder especially as the relative curvature was increased. Torque data at the inner cylinder was presented for the first time using DSMC, and radial velocity profiles for different radii ratios and accommodation coefficients have been presented.

High area-to-mass ratio spacecraft in low Earth orbit, where accelerations due to atmospheric drag are not negligible, were investigated using DSMC simulations and analytical free-molecular calculations. Analogies can be made to the classical Crookes radiometer, but it was found that the high orbital velocities and very low densities prevent any gas molecules from being able to interact with the wake-side face of the spacecraft, in turn preventing any substantive radiometric force from being produced. However, small changes in the drag coefficient with spacecraft temperature could make it possible to perform relative position control between two spacecraft in a swarm without the need for any propellant.

7.2 Future Work

The work developed in this thesis presents the opportunity to carry out the following future work:

1. Further analysis on the measurement of velocity slip and temperature jump in *dsmcFoam* should be carried out, along with benchmarking of the parallel performance of the solver. A dynamic load balancing module could be developed in order to maximise the parallel efficiency of the solver.

2. Perform the QK chemical reactions rather than just calculate the reaction rates. This will require developing models to add and remove particles while conserving mass, momentum, and energy. This work will be very important for hypersonic flows involving regions of high temperature, where the chemical reactions can make a significant contribution to the flow field and surface properties.

3. Extend the CLL model implementation to include the treatment of vibrational energy. This will be essential when using the CLL gas-surface interaction model in simulations where the vibrational mode is active.

4. Our new pressure outlet boundary conditions that can account for rotational equilibrium provide an improvement, but they still do not match the results from more computationally expensive simulations using high and low pressure reservoirs. There is possibly a degree of translational non-equilibrium in the test case, and so the boundary conditions should be extended to account for this also.

5. Micro-channels with more bends could be simulated to find out if the enhancement trend is maintained. Longer channels, with a larger range of rarefaction along their length, could also be studied to check if the enhancement is still found.

6. A more sophisticated atmospheric model could be implemented in the SpaceChip analysis to account for effects that the US Standard Atmosphere does not consider, e.g. variable wind direction, and periods of exceptional solar activity.

7. It is believed that high area-to-mass ratio spacecraft could survive re-entry without the need for any form of thermal protection. This could, for example, enable a swarm of them to be deposited on the surface of a planet to be used as a distributed sensor network. DSMC simulations could be used to predict the heating loads on these spacecraft during the portion of re-entry where the flow is in the transition regime, with analytical solutions being used in the free-molecular and continuum regimes to develop a full profile of the temperature obtained by these spacecraft during re-entry.

References

[1] J. M. Reese, M. A. Gallis, and D. A. Lockerby. New directions in fluid dynamics : Non-equilibrium aerodynamic and microsystem flows. *Philosophical Transactions of the Royal Society of London. Series A: Mathematical, Physical and Engineering Sciences*, 361(1813):2967–2988, 2003.

[2] M. Gad-el-Hak. The fluid mechanics of microdevices - the Freeman Scholar lecture. *Journal of Fluids Engineering*, 121(1):5–33, 1999.

[3] M. A. Gallis, R. B. Bond, and J. R. Torczynski. A kinetic-theory approach for computing chemical-reaction rates in upper-atmosphere hypersonic flows. *The Journal of Chemical Physics*, 131(12):124311, 2009.

[4] J. N. Moss, C. E. Glass, and F. A. Greene. DSMC simulations of Apollo capsule aerodynamics for hypersonic rarefied conditions. In *Proceedings of 9th AIAA/ASM Thermophysics and Heat Transfer Conference*, 2006.

[5] M. S. Ivanov, G. N. Markelov, A. V. Kashkovsky, and S. F. Gimelshein. Statistical simulation of high-altitude aerodynamic problems. In *Proceedings of the 3rd European Symposium on Aerothermodynamics for Space Vehicles*, 1999.

[6] M. A. Gallis, K. A. Boyles, and G. J. LeBeau. DSMC simulations in support of the STS-107 accident investigation. In *Proceedings of 24th International Symposium on Rarefied Gas Dynamics*, 2004.

[7] T. Ewart, P. Perrier, I. A. Graur, and J. G. Méolans. Mass flow rate measurements in a microchannel, from hydrodynamic to near free molecular regimes. *Journal of Fluid Mechanics*, 584:337–356, 2007.

[8] J. C. Maxwell. On stresses in rarefied gases arising from inequalities of temperature. *Philosophical Transactions of the Royal Society Part 1*, 170:231–256, 1879.

[9] M. Von Smoluchowski. Über wärmeleitung in verdünnten gasen. *Annalen der Physik und Chemie*, 64:101–130, 1898 (in German).

[10] H. Grad. On the kinetic theory of rarefied gases. *Communications on Pure and Applied Mathematics*, 2:331–407, 1949.

[11] H. M. Mott-Smith. The solution of the Boltzmann equation for a shock wave. *Physical Review*, 82:885–892, 1951.

[12] C. Y. Liu and L. Lees. Kinetic theory description of plane compressible Couette flow. In *Proceedings of 2nd International Symposium on Rarefied Gas Dynamics*, 1961.

[13] P. L. Bhatnagar, E. P. Gross, and M. Krook. A model for collision processes in gases. I. Small amplitude processes in charged and neutral one-component systems. *Physical Review*, 94:511–525, 1954.

[14] H. Struchtrup and M. Torrilhon. Regularization of grad's 13 moment equations: Derivation and linear analysis. *Physics of Fluids*, 15(9):2668–2680, 2003.

[15] X. J. Gu and D. R. Emerson. A high-order moment approach for capturing non-equilibrium phenomena in the transition regime. *Journal of Fluid Mechanics*, 636:177–216, 2009.

[16] X. J. Gu and D. R. Emerson. A computational strategy for the regularized 13 moment equations with enhanced wall-boundary conditions. *Journal of Computational Physics*, 225:263–283, 2007.

[17] P. Taheri, M. Torrilhon, and H. Struchtrup. Couette and Poiseuille microflows: Analytical solutions for regularized 13-moment equations. *Physics of Fluids*, 21(1):017102, 2009.

[18] X. J. Gu and D. R. Emerson. Modeling oscillatory flows in the transition regime using a high-order moment method. *Microfluidics and Nanofluidics*, 10(2):389–401, 2011.

[19] X. J. Gu, D. R. Emerson, and G. H. Tang. Kramers' problem and the Knudsen minimum: a theoretical analysis using a linearized 26-moment approach. *Continuum Mechanics and Thermodynamics*, 21(5):345–360, 2009.

[20] A. Rana, M. Torrilhon, and H. Struchtrup. A robust numerical method for the R13 equations of rarefied gas dynamics: Application to lid driven cavity. *Journal of Computational Physics*, 236:169–186, 2013.

[21] G. A. Bird. *Molecular Gas Dynamics and the Direct Simulation of Gas Flows*. Oxford Science Publications, Oxford University Press Inc, New York, 1994.

[22] A. Frangi, A. Frezzotti, and S. Lorenzani. On the application of the BGK kinetic model to the analysis of gas-structure interactions in MEMS. *Computers & Structures*, 85(11–14): 810–817, 2007.

[23] C. Cercignani. *Mathematical Methods in Kinetic Theory*. Plenum Publishing Inc., 223 Spring Street, New York, N.Y. 10013, 1990.

[24] B. J. Alder and T. E. Wainwright. Studies in molecular dynamics. I. General method. *Journal of Chemical Physics*, 31(2):459–466, 1959.

[25] A. L. Garcia. *Numerical Methods for Physics*. Prentice-Hall, Inc, Upper Saddle River, New Jersey, 2000.

[26] OpenFOAM Foundation. http://www.openfoam.org, 2011.

[27] G. B. Macpherson. *Molecular Dynamics Simulation in Arbitrary Geometries for Nanoscale Fluid Mechanics*. PhD thesis, University of Strathclyde, 2008.

[28] M. K. Borg. *Hybrid Molecular-Continuum Modelling of Nano-Scale Flows*. PhD thesis, University of Strathclyde, 2010.

[29] M. K. Borg, D. A. Lockerby, and J. M. Reese. A multiscale method for micro/nano flows of high aspect ratio. *Journal of Computational Physics*, 233:400–413, 2013.

[30] G. A. Bird. Sophisticated DSMC. In *Notes prepared for short-course at the DSMC07 meeting*, 2007.

[31] G. A. Bird. Approach to translational equilibrium in a rigid sphere gas. *Physics of Fluids*, 6(10):1518–1519, 1963.

[32] B. J. Alder and T. E. Wainwright. *Transport Processes in Statistical Mechanics*. Interscience Publishers, New York, 1958.

[33] G. A. Bird. Shock wave structure in a rigid sphere gas. In *Proceedings of the Fourth International Symposium on Rarefied Gas Dynamics*, 1965.

[34] G. A. Bird. The velocity distribution function within a shockwave. *Journal of Fluid Mechanics*, 30(4):479–487, 1967.

[35] G. A. Bird. The structure of normal shockwaves in a binary gas mixture. *Journal of Fluid Mechanics*, 31(4):657–668, 1968.

[36] G. A. Bird. Breakdown of translational and rotational equilibrium in gaseous expansions. *AIAA Journal*, 8(11):1998–2003, 1970.

[37] G. A. Bird. Direct simulation and the Boltzmann equation. *Physics of Fluids*, 13(11): 2676–2681, 1970.

[38] G. A. Bird. Recent advances and current challenges for DSMC. *Computers & Mathematics with Applications*, 35(1-2):1–14, 1998.

[39] W. Wagner. A convergence proof for Bird's direct simulation Monte Carlo method for the Boltzmann equation. *Journal of Statistical Physics*, 66:1011–1044, 1992.

[40] C. Borgnakke and P. S. Larsen. Statistical collision model for Monte Carlo simulation of polyatomic gas mixture. *Journal of Computational Physics*, 18(4):405–420, 1975.

[41] G. A. Bird. Definition of mean free path for real gases. *Physics of Fluids*, 26(11):3222–3223, 1983.

[42] G. A. Bird. Perception of numerical methods in rarefied gas dynamics. *Progress in Astronautics and Aeronautics*, 118:211–226, 1989.

[43] M. S. Ivanov and S. V. Rogasinsky. Analysis of numerical techniques of the direct simulation Monte Carlo method in the rarefied gas dynamics. *Russian Journal of Numerical Analysis and Mathematical Modelling*, 3(6):453–465, 1988.

[44] S. K. Stefanov. On DSMC calculations of rarefied gas flows with small number of particles in cells. *SIAM Journal on Scientific Computing*, 33(2):677–702, 2011.

[45] C. C. Su, K. C. Tseng, H. M. Cave, J. S. Wu, Y. Y. Lian, T. C. Kuo, and M. C. Jermy. Implementation of a transient adaptive sub-cell module for the parallel-DSMC code using unstructured grids. *Computers & Fluids*, 39(7):1136–1145, 2010.

[46] N. G. Hadjiconstantinou, A. L. Garcia, M. Z. Bazant, and G. He. Statistical error in particle simulations of hydrodynamic phenomena. *Journal of Computational Physics*, 187(1):274–297, 2003.

[47] DSMC Resources from Graeme Bird. http://gab.com.au, 2012.

[48] S. Dietrich and I. D. Boyd. Scalar and parallel optimized implementation of the direct simulation Monte Carlo method. *Journal of Computational Physics*, 126(2):328–342, 1996.

[49] MONACO. http://ngpdlab.engin.umich.edu/research/monaco, 2012.

[50] G. A. Bird. Simulation of multi-dimensional and chemically reacting flows (past Space Shuttle orbiter). In *Proceedings of the 11th International Symposium on Rarefied Gas Dynamics*, pages 365–388, 1979.

[51] M. S. Ivanov, A. V. Kashkovsky, S. F. Gimelshein, G. N. Markelov, A. A. Alexeenko, Y. A. Bondar, G. A. Zhukova, S. B. Nikiforov, and P. V. Vashenkov. SMILE system for 2D/3D DSMC computations. In *Proceedings of the 25th International Symposium on Rarefied Gas Dynamics*, pages 539–544, 2006.

[52] J. F. Padilla. *Assessment of Gas-Surface Interaction Models for Computaion of Rarefied Hypersonic Flows*. PhD thesis, University of Michigan, 2008.

[53] J. F. Padilla and I. D. Boyd. Assessment of gas-surface interaction models for computation of rarefied hypersonic flow. *Journal of Thermophysics and Heat Transfer*, 23(1):96–105, 2009.

[54] A. J. Lofthouse. *Nonequilibrium Hypersonic Aerothermodynaics Using the Direct Simulation Monte Carlo and Navier-Stokes Models*. PhD thesis, University of Michigan, 2008.

[55] A. J. Lofthouse, L. C. Scalabrin, and I. D. Boyd. Velocity slip and temperature jump in hypersonic aerothermodynamics. *45th AIAA Aerospace Sciences Meeting and Exhibit*, 2007.

[56] S. F. Gimelshein, N. E. Gimelshein, A. D. Ketsdever, and N. P. Selden. Analysis and applications of radiometeric forces in rarefied gas flows. *AIP Conference Proceedings*, 1333(1):693–700, 2011.

[57] W. Crookes. On attraction and repulsion resulting from radiation - part II. *Proceedings of the Royal Society of London*, 23:373, 1875.

[58] T. J. Scanlon, E. Roohi, C. White, M. Darbandi, and J. M. Reese. An open source, parallel DSMC code for rarefied gas flows in arbitrary geometries. *Computers & Fluids*, 39(10):2078 – 2089, 2010.

[59] E. Arlemark, G. Markelov, and S. Nedea. Rebuilding of Rothe's nozzle measurements with OpenFOAM software. *Journal of Physics: Conference Series*, 362:012040, 2012.

[60] B. L. Haas, J. D. McDonald, and L. Dagum. Models of thermal relaxation mechanics for particle simulation methods. *Journal of Computational Physics*, 107(2):348–358, 1993.

[61] F. Bergemann and I. D. Boyd. New discrete vibrational energy model for the direct simulation Monte Carlo method. *Progress in Astronautics and Aeronautics*, 158:174–183, 1994.

[62] G. A. Bird. A comparison of collision energy-based and temperature-based procedures in DSMC. *AIP Conference Proceedings*, 1084(1):245–250, 2008.

[63] G. Zuppardi, L. Morsa, and F. Romano. Influence of chemical models on the computation of thermo-fluid-dynamic parameters in hypersonic, rarefied flows. *Proceedings of the Institution of Mechanical Engineers, Part G: Journal of Aerospace Engineering*, 224: 637–646, 2010.

[64] I. D. Boyd. Modeling backward chemical rate processes in the direct simulation Monte Carlo method. *Physics of Fluids*, 19(12):126103, 2007.

[65] G. A. Bird. Chemical reactions in DSMC. In *Rarefied Gas Dynamics*, pages 1195–1202, 2011.

[66] G. A. Bird. The Q-K model for gas-phase chemical reaction rates. *Physics of Fluids*, 23 (10):106101, 2011.

[67] National Institute for Standards and Technology. http://kinetics.nist.gov/kinetics/kineticssearchform.jsp, 2012.

[68] N. G. Hadjiconstantinou. Private communication, 2012.

[69] G. B. Macpherson, N. Nordin, and H. G. Weller. Particle tracking in unstructured, arbitrary polyhedral meshes for use in CFD and molecular dynamics. *Communications in Numerical Methods in Engineering*, 25(3):263–273, 2009.

[70] G. Karniadakis, A. Beskok, and N. Aluru. *Microflows and Nanoflows: Fundamentals and Simulation*. Springer Science+Business Media, Inc., 233 Spring St, New York, 2005.

[71] N. Dongari, F. Durst, and S. Chakraborty. Predicting microscale gas flows and rarefaction effects through extended Navier-Stokes-Fourier equations from phoretic transport considerations. *Microfluidics and Nanofluidics*, 9:831–846, 2010.

[72] W. Steckelmacher. Knudsen flow 75 years on: the current state of the art for flow of rarefied gases in tubes and systems. *Reports on Progress in Physics*, 49(10):1083–1107, 1999.

[73] C. Cercignani and M. Lampis. Kinetic models for gas-surface interactions. *Transport Theory and Statistical Physics*, 1(2):101–114, 1971.

[74] R. G. Lord. Application of the Cercignani-Lampis scattering kernel to direct simulation Monte Carlo calculations. In *Proceedings of the 17th International Symposium on Rarefied Gas Dynamics*, pages 1427–1433, 1990.

[75] R. G. Lord. Some extensions to the Cercignani–Lampis gas–surface scattering kernel. *Physics of Fluids A: Fluid Dynamics*, 3(4):706–710, 1991.

[76] R. G. Lord. Some further extensions of the Cercignani–Lampis gas–surface interaction model. *Physics of Fluids*, 7(5):1159–1161, 1995.

[77] T. A. Gombosi. *Gaskinetic Theory*. Cambridge University Press, Cambridge, 1994.

[78] G. A. Radtke, N. G. Hadjiconstantinou, and W. Wagner. Low-noise Monte Carlo simulation of the variable hard sphere gas. *Physics of Fluids*, 23(3):030606, 2011.

[79] H. A. Al-Mohssen and N. G. Hadjiconstantinou. Low variance direct Monte Carlo simulations using importance weights. *ESAIM: Mathematical Modelling and Numerical Analysis*, 44:1069–1083, 2010.

[80] E. S. Piekos and K. S. Breuer. Numerical modeling of micromechanical devices using the direct simulation Monte Carlo method. *Journal of Fluids Engineering*, 118(3):464–469, 1996.

[81] R. P. Nance, D. B. Hash, and H. A. Hassan. Role of boundary conditions in Monte Carlo simulation of MEMS devices. *Journal of Thermophysics and Heat Transfer*, 12(3): 119–128, 1997.

[82] J.-S. Wu, F. Lee, and S.-C. Wong. Pressure boundary treatment in micromechanical devices using the direct simulation Monte Carlo method. *JSME International Journal Series B Fluids and Thermal Engineering*, 44(3):439–450, 2001.

[83] J.-S. Wu and K.-C. Tseng. Analysis of micro-scale gas flows with pressure boundaries using direct simulation Monte Carlo method. *Computers & Fluids*, 30(6):711–735, 2001.

[84] W. W. Liou and Y. Fang. Heat transfer in microchannel devices using DSMC. *Journal of Microelectromechanical Systems*, 10(2):274–279, 2001.

[85] Y. Fang and W. W. Liou. Computations of the flow and heat transfer in microdevices using DSMC with implicit boundary conditions. *Journal of Heat Transfer*, 124(2):338–345, 2002.

[86] W. W. Liou and Y. Fang. *Microfluid Mechanics*. McGraw-Hill, Two Penn Plaza, New York, 2006.

[87] M. Wang and Z. Li. Simulations for gas flows in microgeometries using the direct simulation Monte Carlo method. *International Journal of Heat and Fluid Flow*, 25(6):975–985, 2004.

[88] J. J. Ye, J. Yang, J. Y. Zheng, W. Z. Li, S. Z. He, and Y. B. Ma. New treatment of pressure boundary conditions for DSMC method in micro-channel flow simulations. *ASME Conference Proceedings*, pages 121–126, 2007.

[89] J. J. Ye, J. Yang, J. Y. Zheng, P. Xu, C. Lam, L. Wong, and Y. Ma. Effects of wall temperature on the heat and mass transfer in microchannels using the DSMC method. In *Nano/Micro Engineered and Molecular Systems, 2009. NEMS 2009. 4th IEEE International Conference on*, pages 666–671, 2009.

[90] J. Yang, J. J. Ye, J. Y. Zheng, I. Wong, C. K. Lam, P. Xu, R. X. Chen, and Z. H. Zhu. Using direct simulation Monte Carlo with improved boundary conditions for heat and mass transfer in microchannels. *Journal of Heat Transfer*, 132(4):041008, 2010.

[91] E. Roohi, M. Darbandi, and V. Mirjalili. Direct simulation Monte Carlo solution of subsonic flow through micro/nanoscale channels. *Journal of Heat Transfer*, 131(9):092402, 2009.

[92] E. Kennard. *Kinetic Theory of Gases*. McGraw-Hill Book Company, Inc., New York and London, 1938.

[93] G. N. Patterson. *Molecular Flow of Gases*. John Wiley & Sons, Inc., New York, 1956.

[94] W. G. Vincenti and C. H. Kruger. *Introduction to Physical Gas Dynamics*. Krieger Publishing Company, Malabar, Florida, 1965.

[95] S. Y. K. Lee, M. Wong, and Y. Zohar. Gas flow in microchannels with bends. *Journal of Micromechanics and Microengineering*, 11(6):635–644, 2001.

[96] A. A. Alexeenko, S. F. Gimelshein, and D. A. Levin. Reconsideration of low reynolds number flow-through constriction microchannels using the DSMC method. *Journal of Microelectromechanical Systems*, 14(4):847–856, 2005.

[97] A. Beskok, G. E. Karniadakis, and W. Trimmer. Rarefaction and compressibility effects in gas microflows. *Journal of Fluids Engineering*, 118(3):448–456, 1996.

[98] A. Agrawal, L. Djenidi, and A. Agrawal. Simulation of gas flow in microchannels with a single ninety-degree bend. *Computers & Fluids*, 38(8):1629–1637, 2009.

[99] O. Rovenskaya and G. Croce. Numerical analysis of rarefaction and compressibility effects in bent microchannels. *ASME Conference Proceedings*, pages 451–458, 2010.

[100] D. A. Lockerby, J. M. Reese, David R. Emerson, and Robert W. Barber. Velocity boundary condition at solid walls in rarefied gas calculations. *Physical Review E*, 70:017303, 2004.

[101] D. Einzel, P. Panzer, and M. Liu. Boundary condition for fluid flow: Curved or rough surfaces. *Physical Review Letters*, 64:2269–2272, 1990.

[102] K. W. Tibbs, F. Baras, and A. L. Garcia. Anomalous flow profile due to the curvature effect on slip length. *Physical Review E*, 56:2282–2283, 1997.

[103] K. Aoki, H. Yoshida, T. Nakanishi, and A. L. Garcia. Inverted velocity profile in the cylindrical Couette flow of a rarefied gas. *Physical Review E*, 68:016302, 2003.

[104] S. Yuhong, R. W. Barber, and D. R. Emerson. Inverted velocity profiles in rarefied cylindrical Couette gas flow and the impact of the accommodation coefficient. *Physics of Fluids*, 17(4):047102, 2005.

[105] Z. Guo, B. Shi, and C. Zheng. Velocity inversion of micro cylindrical Couette flow: A lattice Boltzmann study. *Computers and Mathematics with Applications*, 61(12):3519 – 3527, 2011.

[106] S. Kim. Slip velocity and velocity inversion in a cylindrical couette flow. *Physical Review E*, 79:036312, 2009.

[107] Y. Jung. Velocity inversion in nanochannel flow. *Physical Review E*, 75:051203, 2007.

[108] A. R. Kuhlthau. Air friction on rapidly moving surfaces. *Journal of Applied Physics*, 20 (2):217 –223, 1949.

[109] A. Agrawal and S. V. Prabhu. Deduction of slip coefficient in slip and transition regimes from existing cylindrical Couette flow data. *Experimental Thermal and Fluid Science*, 32 (4):991–996, 2008.

[110] D. J. Barnhart, T. Vladimirova, and M. N. Sweeting. Very-small-satellite design for distributed space missions. *Journal of Spacecraft and Rockets*, 44(6):1294–1306, 2007.

[111] C. Colombo and C. R. McInnes. Orbit design for future SpaceChip swarm missions in a planetary atmosphere. *Acta Astronautica*, 75:25 – 41, 2012.

[112] C. Colombo, C. Lücking, and C. R. McInnes. Orbit evolution, maintenance and disposal of SpaceChip swarms. *6th International Workshop on Satellite Constellation and Formation Flying*, 2010.

[113] I. I. Shapiro and H. M. Jones. Perturbations of the orbit of the ECHO balloon. *Science*, 132:1484–1486, 1960.

[114] C. Colombo and C. R. McInnes. Orbital dynamics of 'smart dust' devices with solar radiation pressure and drag. *Journal of Guidance, Control, and Dynamics*, 34(6):1613–1631, 2010.

[115] J. A. Atchison and M. A. Peck. A passive, sun-pointing, millimeter-scale solar sail. *Acta Astronautica*, 67(1-2):108–121, 2010.

[116] C. W. Johnson, C. A. Lundquist., and J. L. Zurasky. The LAGEOS satellite. In *Anaheim International Astronautical Federation Congress*, 1976.

[117] H. Heidt, J. Puig-Suari, A. S. Moore, S. Nakasuka, and R. J. Twiggs. CubeSat: A new generation of picosatellite for education and industry low-cost space experimentation. In *Proceedings of the 14th Annual AIAA/USU Conference on Small Satellites*, 2000.

[118] N. P. Selden, C. Ngalande, N. E. Gimelshein, S. F. Gimelshein, and A. D. Ketsdever. Origins of radiometric forces on a circular vane with a temperature gradient. *Journal of Fluid Mechanics*, 634:419–431, 2009.

[119] N. E. Gimelshein, S. F. Gimelshein, A. D. Ketsdever, and N. P. Selden. Shear force in radiometric flows. *AIP Conference Proceedings*, 1333(1):661–666, 2011.

[120] O. Reynolds. On certain dimensional properties of matter in the gaseous state. *Philosophical Transactions of the Royal Society Part 1*, 170:727–845, 1879.

[121] A. Einstein. Zur theorie der radiometrerkrafte. *Zeitschrift fur Physik*, 27:1–5, 1924 (in German).

[122] M. Scandurra, F. Iacopetti, and P. Colona. Gas kinetic forces on thin plates in the presence of thermal gradients. *Physical Review E*, 75:026308, 2007.

[123] M. Ota, Y. He, and S. K. Stefanov. Monte Carlo simulation of rotation of a laser opto-microactuator. In *Rarefied Gas Dynamics: 25th International Symposium*, 2007.

[124] Y. He, S. K. Stefanov, and M. Ota. The Monte Carlo simulation of a model microactuator driven by rarefied gas thermal effects. In *Rarefied Gas Dynamics: 26th International Symposium*, 2009.

[125] NASA. NASA-TM-X-74335, U.S. Standard Atmosphere. Technical report, 1976.

[126] B. Cornella, A. D. Ketsdever, N. E. Gimelshein, and S. F. Gimelshein. Analysis of multi-vane radiometers in high-altitude propulsion. *10th AIAA/ASME Joint Thermophysics and Heat Transfer Conference*, 2010.

[127] D. A. Vallado. *Fundamentals of Astrodynamics and Applications.* Space Technology Library, New York, 2007.

[128] J. A. Storch. Aerodynamic disturbances on spacecraft in free-molecular flow. Technical report, DTIC Document, 2002.

[129] K. Moe and M. M. Moe. Gas surface interactions and satellite drag coefficients. *Planetary and Space Science*, 53:793–801, 2005.

[130] I. A. Graur, P. Perrier, W. Ghozlani, and J. G. Méolans. Measurements of tangential momentum accommodation coefficient for various gases in plane microchannel. *Physics of Fluids*, 21(10):102004, 2009.

[131] K. J. Daun, M. Karttunen, and J. T. Titantah. Molecular Dynamics simulation of thermal accommodation coefficients for laser-induced incandescence sizing of nickel nanoparticles. *Proceedings of the ASME 2011 International Mechanical Engineering Congress & Exposition*, 2011.

[132] V. L. Kovalev and A. N. Yakunchikov. Accommodation coefficients for molecular hydrogen on a graphite surface. *Fluid Dynamics*, 45(6):975–981, 2010.

[133] J. A. Atchison and M. A. Peck. Length scaling in spacecraft dynamics. *Journal of Guidance, Control and Dynamics*, 34(1):231–245, 2011.

[134] P. Willis, F. Deleflie, F. Barlier, Y. E. Bar-Sever, and L. J. Romans. Effects of thermosphere total density perturbations on LEO orbits during severe geomagnetic conditions (Oct–Nov 2003) using DORIS and SLR data. *Advances in Space Research*, 36(3):522–533, 2005.

[135] C. Berger, R. Biancale, M. Ill, and F. Barlier. Improvement of the empirical thermospheric model DTM: DTM94 – a comparative review of various temporal variations and prospects in space geodesy applications. *Journal of Geodesy*, 72:161–178, 1998.

[136] J. Kawaguchi, Y. Mimasu, O. Mori, R. Funase, T. Yamamoto, and Y. Tsuda. IKAROS - Ready for lift-off as the world's first solar sail demonstration in interplanetary space. *60th International Astronautical Congress*, 2009.

[137] W. J. Larson and J. R. Wertz, editors. *Space Mission Analysis and Design*. Microcosm Press and Kluwer Academic Publishers, 1999.

[138] R. De Villamil and G. Avanzini. *The Laws of Avanzini: Laws of Planes Moving at an Angle in Air and Water*. Forgotten Books, 1912.